CHEMICAL POTENTIAL SHIFT OF K-DOPED TITANIUM CARBONITRIDES AND TITANIUM CARBIDES (MXENES)

Warakorn Jindata

A Thesis Submitted in Partial Fulfillment of the Requirement for the

Degree of Doctor of Philosophy in Physics

Suranaree University of Technology

Academic Year 2020

การเลื่อนของศักย์เคมีของไทเทเนียมคาร์ไบด์และไทเทเนียมคาร์บอนไนไตรด์ (แมกซีน) ที่เจือด้วยโพแทสเซียม

นายวรากร จินดาทา

วิทยานิพนธ์นี้เป็นส่วนหนึ่งของการศึกษาตามหลักสูตรปริญญาวิทยาศาสตรดุษฎีบัณฑิต
สาขาวิชาฟิสิกส์
มหาวิทยาลัยเทคโนโลยีสุรนารี
ปีการศึกษา 2563

CHEMICAL POTENTIAL SHIFT OF K-DOPED TITANIUM CARBONITRIDES AND TITANIUM CARBIDES (MXENES)

Suranaree University of Technology has approved this thesis submitted in partial fulfillment of the requirements for the Degree of Doctor of Philosophy.

Thesis Examining Committee

(Assoc. Prof. Dr. Panomsak Meemon)
Chairperson

(Assoc. Prof. Dr. Worawat Meevasana)
Member (Thesis Advisor)

(Assoc. Prof. Dr. Prayoon Songsiriritthigul)
Member

(Dr. Ittipon Fongkaew)
Member

(Dr. Hideki Nakajima)
Member

Chatchai Jothi
(Assoc. Prof. Dr. Chatchai Jothityangkoon)
Vice Rector for Academic Affairs
and Quality Assurance

(Assoc. Prof. Dr. Worawat Meevasana)
Dean of Institute of Science

วรากร จินดาทา : การเลื่อนของศักย์เคมีของไทเทเนียมคาร์ไบด์และไทเทเนียมคาร์บอนไนไตรด์ (แมกซีน) ที่เจือด้วยโพแทสเซียม (CHEMICAL POTENTIAL SHIFT OF K-DOPED TITANIUM CARBONITRIDES AND TITANIUM CARBIDES (MXENES)). อาจารย์ที่ปรึกษา : รองศาสตราจารย์ ดร.วรวัฒน์ มีวาสนา, 94 หน้า.

สารประกอบโครงสร้างสองมิติโลหะทรานซิชันคาร์ไบด์ คาร์บอนไนไตรด์ และไนไตรด์ (แมกซีน) แสดงคุณสมบัติเฉพาะตัวได้แก่ มีค่าการนำไฟฟ้าสูง มีประสิทธิภาพในการให้ไอออนแทรกเข้าไปในระหว่างชั้นของโครงสร้างได้ และมีปฏิกิริยารีดอกซ์แบบผันกลับได้ ส่งผลให้แมกซีนถูกนำไปประยุกต์ใช้ในหลากหลายแอปพลิเคชันได้แก่ การกักเก็บพลังงาน และ การแปลงพลังงาน การป้องกันการรบกวนจากคลื่นแม่เหล็กไฟฟ้า และอิเล็กทรอนิกส์ จากการศึกษาการแทนที่อะตอมคาร์บอนด้วยอะตอมไนโตรเจนในโครงสร้างของสารประกอบไทเทเนียมคาร์ไบด์ ($Ti_3C_2T_x$) เกิดเป็นสารประกอบไทเทเนียมคาร์บอนไนไตรด์ (Ti_3CNT_x) ถูกพบว่าเป็นการนำไปสู่การเปลี่ยนแปลงของคุณสมบัติทางอิเล็กทรอนิกส์ที่แตกต่างกันระหว่าง $Ti_3C_2T_x$ และ Ti_3CNT_x เช่น Ti_3CNT_x มีประจุลบที่บริเวณพื้นผิวสูงมากกว่า $Ti_3C_2T_x$ เมื่ออยู่ในสารละลาย และ Ti_3CNT_x มีประสิทธิภาพในการป้องกันการรบกวนจากคลื่นแม่เหล็กไฟฟ้าสูงมากกว่า $Ti_3C_2T_x$ วิทยานิพนธ์นี้นำเสนอผลการศึกษาทางการทดลองด้วยการใช้เทคนิคอัลตราไวโอเลตโฟโตอิมิชชันสเปกโทรสโกปีเพื่อศึกษาโครงสร้างอิเล็กทรอนิกส์ของสารประกอบ Ti_3CNT_x และ $Ti_3C_2T_x$ ด้วยการเปรียบเทียบกันในฟังก์ชันของความหนาแน่นอิเล็กตรอน ผลการทดลองแสดงให้เห็นว่าโครงสร้างอิเล็กทรอนิกส์ในระดับชั้นแกนกลาง 3p ของอะตอมไทเทเนียมของ Ti_3CNT_x แสดงการเลื่อนของศักย์เคมีที่ผิดปกติประมาณ 250 มิลลิอิเล็กตรอนโวลต์ ไปทางด้านพลังงานยึดเหนี่ยวลดลงเมื่อเพิ่มความหนาแน่นของอิเล็กตรอน ซึ่งโครงสร้างอิเล็กทรอนิกส์ที่แสดงการเลื่อนของศักย์เคมีไปทางด้านพลังงานยึดเหนี่ยวลดลงเมื่อเพิ่มของความหนาแน่นอิเล็กตรอนนี้ เป็นสัญลักษณ์ของคุณสมบัติการบีบอัดอิเล็กตรอนที่มีค่าติดลบ แต่อย่างไรก็ตาม ผลการทดลองโครงสร้างอิเล็กทรอนิกส์ที่แสดงการเลื่อนของศักย์เคมีไปทางด้านพลังงานยึดเหนี่ยวลดลงในฟังก์ชันของการเพิ่มความหนาแน่นของอิเล็กตรอนไม่ถูกพบในผลการทดลองของ $Ti_3C_2T_x$ ผลการทดลองโครงสร้างอิเล็กทรอนิกส์การเลื่อนของศักย์เคมีใน Ti_3CNT_x และ $Ti_3C_2T_x$ ถูกอธิบายด้วยการคำนวณโครงสร้างอิเล็กทรอนิกส์การเลื่อนของศักย์เคมีทางทฤษฎีด้วยทฤษฎีฟังก์ชันความหนาแน่น ผลการคำนวณด้วยทฤษฎีฟังก์ชันความหนาแน่นแสดงให้เห็นว่าพันธะเคมีระหว่างอะตอมไทเทเนียมและอะตอมไนโตรเจนช่วยส่งเสริมให้อะตอมไทเทเนียมของ Ti_3CNT_x มีชั้นสถานะว่างสำหรับรองรับการเติมอิเล็กตรอนได้มากกว่าปกติที่บริเวณเหนือระดับชั้นพลังงานเฟอร์มิขึ้นไป ซึ่งเป็นการนำไปสู่การค้นพบคุณสมบัติการบีบอัดอิเล็กตรอนที่มีค่าติดลบใน Ti_3CNT_x ดังนั้นการศึกษาโครงสร้างอิเล็กทรอนิกส์การเลื่อนของศักย์เคมีในฟังก์ชันของ

การเพิ่มความหนาแน่นอิเล็กตรอนในสารประกอบ Ti_3CNT_x และ $Ti_3C_2T_x$ ทางด้านการทดลองด้วยเทคนิคอัลตราไวโอเลตโฟโตอิมิชชันสเปกโทรสโกปี และการคำนวณทางทฤษฎีด้วยทฤษฎีฟังก์ชันความหนาแน่น สามารถอธิบายได้ถึงความแตกต่างกันในคุณสมบัติทางอิเล็กทรอนิกส์ของ Ti_3CNT_x และ $Ti_3C_2T_x$ และยังนำเสนอวิธีการใหม่ที่จะประยุกต์ใช้คุณสมบัติการบีบอัดอิเล็กตรอนที่มีค่าติดลบใน Ti_3CNT_x สำหรับแอปพลิเคชันทางด้านการกักเก็บพลังงาน และการกักเก็บประจุ

สาขาวิชาฟิสิกส์ ลายมือชื่อนักศึกษา กรทร จินดาม

ปีการศึกษา 2563 ลายมือชื่ออาจารย์ที่ปรึกษา

WARAKORN JINDATA : CHEMICAL POTENTIAL SHIFT OF K-DOPED
TITANIUM CARBONITRIDE AND TITANIUM CARBIDE (MXENES)
THESIS ADVISOR : ASSOC. PROF. WORAWAT MEEVASANA, Ph.D.
94 PP.

MXENE/TI$_3$CNT$_X$/TI$_3$C$_2$T$_X$/2D MATERIALS/ELECTRONIC STRUCUTURE/ PHOTOEMISSION SPECTROSCOPY/DENSITY FUNCTIONAL THEORY

Two-dimensional transition metal carbides, carbonitrides, and nitrides called MXenes exhibit high metallic conductivity, ion intercalation capability and reversible redox activity, prompting their applications in energy storage and conversion, electromagnetic interference (EMI) shielding, and electronics, among many other fields. It has been shown that replacement of about 50% of carbon atoms in the most popular MXene family member, titanium carbide ($Ti_3C_2T_x$), by nitrogen atoms, forming titanium carbonitride (Ti_3CNT_x), leads to drastically different properties. Such properties include very high negative charge in solution and extreme EMI shielding effectiveness, exceeding all known materials, even metals at comparable thicknesses. This thesis presents ultraviolet photoemission spectroscopy (UPS) experiments on the electronic structures of Ti_3CNT_x and $Ti_3C_2T_x$ MXenes. The electronic structures of two MXenes are systematically investigated and compared as a function of electron density. We observe that, in contrast to $Ti_3C_2T_x$, the Ti 3p core-level of Ti_3CNT_x exhibits a counterintuitive shift to a lower binding energy of up to approximately 250 meV upon increasing the electron density, which is a spectroscopic signature of negative electronic compressibility (NEC). These experimentally measured chemical potential shifts are well captured by the density functional theory (DFT) calculation. The DFT results also further suggest that the hybridization of titanium-nitrogen bonding in Ti_3CNT_x helps promoting the available states of Ti atoms for receiving more electron above the Fermi level and leads to the observed NEC. Our UPS experiments and DFT calculations explain the differences in electronic properties between Ti_3CNT_x and $Ti_3C_2T_x$ MXenes and suggest a new strategy to apply the NEC effect of Ti_3CNT_x in energy and charge storage applications.

School of Physics	Student's Signature Warakorn Jindata
Academic Year 2020	Advisor's Signature

ACKNOWLEDGMENTS

First and foremost, I would like to sincerely thank Prof. Worawat Meevasana who has been my thesis supervisor. About 5 years ago, I promptly got a communication from WM by telephone after I sent the email to him for enrolling to be a PhD student under his supervision. I felt that WM is very kind and gentle. At that time, I had not hesitated in applying to be his student, that was a beginning of a new challenge at Suranaree University of Technology (SUT). WM is very kind of advisor. He has taught many great scientific ideas on photoemission spectroscopy together with concepts of physics. I would always feel good when I got any comments and suggestions from him. For me, WM is an excellence role model to conduct the frontier research in physics. WM gave me a chance to do the research in abroad; for example, doing the ARPES experiment at Soleil Synchrotron in France and at Stanford Synchrotron Radiation Light Source in USA. Moreover, WM led me done the manuscript for submitting to high-impact journal, which is a one of great experience. With his best wishes and best supervision, I have to say that I am profoundly grateful, and I will respect WM forever.

I also would like to thank my two awesome coaches; Dr. Tanachat Eknapakul and Dr. Ittipon Fongkaew, who are professional physicists that have an excellence scientific mindset. Dr. Tanachat helps and supports me in everything. I have learned many experimental skills from him; for example, Igor Pro program, photoemission experiments, and manuscript preparation concept. I would get complained from him if I got slothful but I knew in my heart that he did it to change me for the better good. For Dr. Ittipon, I would like to really thank him from my heart. Dr. Ittipon is very nice.

He is an important person that performs all computational calculations as we have discussed in this thesis. He also gives an advice in theoretical aspects and computational methods. Without great helps from him my thesis would not be completed.

I truly appreciate Prof. Yury Gogotsi and Dr. Kanit Hantanasirisakul. Prof. Yury always quick reply an email despite of his busy times. Dr. Kanit is a smart scientist with many skills. He is a very good colleague who is another person that I have to say thank you from my heart. We have communicated in online all the time, but he never said no to my any helps request. Prof. Yury and Dr. Kanit did not only provide a good Ti_3CNT_x and $Ti_3C_2T_x$ MXenes samples to our lab, but also shared insights knowledge of MXenes on scientific ideas and useful discussions. Moreover, Prof. Yury kindly gave the opportunity to me and WM to submitting our manuscript to Applied Physics Reviews under his invitation. Prof. Yury and Dr. Kanit have a systematical and potential approaches in writing the manuscript. They kindly helped me in preparing the manuscript in many steps including; discussions, comments, suggestions, and revisions the manuscript, in order to be suitable for submitting to Applied Physics Reviews. Owing to a lot of help from them, my manuscript has been accepted for publication in Applied Physics Reviews. Without both of them, my thesis would not be accomplished too.

I would like to acknowledge Prof. Prayoon Songsiriritthigul. Prof. Prayoon is very kind. He always supports and encourages me in everything. In 2017, he encouraged me to travel to Paris and led me to do the experiments on the photoemission spectroscopy of liquid with his team at the GALAXIES beamline of Soleil Synchrotron in France. It was a good experience that I have learned in using the synchrotron light for scientific experiments in abroad for the first time.

I would like to thank Dr. Jonathan D. Denlinger, the beamline manager of the beamline 4.0.3 (MERLIN) of the Advanced Light Source in USA, for the allocation of synchrotron photoemission beamtime to measure our MXene samples.

I am thankful to beamline manager; Dr. Hideki Nakajima, and all beamline scientists of the beamline 3.2Ua of the Synchrotron Light Research Institute. I have to say a special thanks to Dr. Hideki Nakajima and Dr. Arunothai Rattanachata, who are very good with many insights in synchrotron radiation and photoemission spectroscopy. Dr. Hideki and Dr. Arunothai kindly taught me in using the Simulation of Electron Spectra for Surface Analysis (SESSA) program for analyzing some UPS data in this thesis. Thanks Dr. Ratchadaporn Supruangnet, Dr. Thanit Saisopa, Mr. Surachet Rattanasuporn, and Mr. Watcharapon Jenpiyapong. All of them always support and maintain the photoemission system and kindly share some experimental experience to me.

In the Meevasana group, I believe it was a destiny that I was a membership of this research group. We are a big family. I would like to thank Dr. Siwat Polin and Dr. Supansa Musikajaroen for helping and supporting me in many things. We often have the useful discussion in many aspects. Ms. Areeya Mooltang is acknowledged for her miscellaneous helps. Without Areeya, my life in SUT would have been much harder. Thanks Dr. Sumet Siriroj, Mr. Sujinda Chaiyachad, Mr. Suppanat Sangphet, Mr. Worasarit Saengsui, Mr. Seksan Laopa, Mr. Chutchawan Jaisuk, Mr. Peerawat Laohana, Mr. Suwat Thila, Ms. Aissara Rasritat, Mr. Ukrit Jitropas, Mr. Anan Sutcha, Ms. Manlika Sriondee, Ms. Pakwan Chaprakhon, and all members in Meevasana group. I am sure that I will never forget all of them absolutely, because they are the important persons who make me having wonderful memories at SUT.

Thanks all staffs, students, and friends at the School of Physics, Institute of Science, SUT, for their kindly supports.

Importantly, the Synchrotron Light Research Institute is acknowledged for financial support providing covering the study throughout PhD program and the opportunities in doing research in abroad.

Dear Ms. Punchanok Chompu, where ever you are. I hope you can hear my thanks to you, and hopefully you will read all these appreciation sentences in someday. Punchanok is the special one who is the sunshine of my life. It is you. It is always been you. I think I will never find a better girlfriend than you. Even though our relationship was already ended, but everything about you is never gone from my breath. Our nice moments along with your smile still impress in my heart, and I never regretted for once I found you. Everything you did it for me will forever be in my memory, and for that I am really thankful.

Last but not least, I dedicate this thesis to my beloved parents; father, Pol. Sen. Sgt. Maj. Samran Jindata; mother, Mrs. Kasinee Jindata; aunt, Ms. Saisamorn Duangta; elder sister, Ms. Somrawee Jindata; elder brother, Mr. Wachirapas Jindata; spiritual preceptor, Venerable Luang-Por Watcharin Kittinantho, who give me an endless love and be by my side all the time when I have had sufferings. My beloved Swangarom family; Mr. Pawin Swangarom, Mrs. Sureeporn Swangarom, Mr. Natthanin Swangarom, Mrs. Pitchanan Swangarom, and Ms. Panchita Swangarom. I would like to thank all of you for the love, encouragements, and supports you always give me.

Warakorn Jindata

CONTENTS

Page

ABSTRACT IN THAI I

ABSTRACT IN ENGLISH III

ACKNOWLEDGMENTS V

CONTENTS IX

LIST OF FIGURES XII

LIST OF TABLES XXII

CHAPTER

I INTRODUCTION 1

1.1 Motivation 1

1.1.1 2D transition metal carbides, carbonitrides, and nitrides (MXenes) 1

1.1.2 The unique intrinsic properties of MXenes 2

1.2 Thesis outline 3

II TITANIUM CARBONITRIDE AND TITANIUM CARBIDE ……….……5

2.1 Synthesis and characterization of titanium carbonitride (Ti_3CNT_x) ….……..5

2.2 Synthesis and characterization of titanium carbide ($Ti_3C_2T_x$) 9

2.3 Materials processing 13

2.4 Electronic structures of Ti_3CNT_x and $Ti_3C_2T_x$ 14

2.5 The experimental study of Ti_3CNT_x and $Ti_3C_2T_x$ 19

2.5.1 Energy storage application of Ti_3CNT_x 19

CONTENTS (Continued)

Page

2.5.2 Electromagnetic interference shielding application of Ti_3CNT_x 20

2.5.3 Energy storage application of $Ti_3C_2T_x$ 24

2.5.4 Electromagnetic interference shielding application of $Ti_3C_2T_x$ 26

III NEGATIVE ELECTRONIC COMPRESSIBILITY 27

3.1 The theoretical and experimental studies on the negative electronic compressibility (NEC) 27

IV PHOTOEMISSION SPECTROSCOPY 32

4.1 Photoelectric effect 32

4.2 The photoemission process 33

4.2.1 The three-step model 33

4.2.2 The one-step model 34

4.3 Ultraviolet photoemission spectroscopy (UPS) 35

4.4 UPS measurements system 36

4.5 Core-level photoemission spectroscopy 41

4.6 Related techniques 42

4.6.1 Potassium evaporation in ultrahigh vacuum 42

4.6.2 Preparation of Ti_3CNT_x and $Ti_3C_2T_x$ for UPS measurement 43

V SPECTROSCOPIC SIGNATURE OF NEGATIVE ELECTRONIC COMPRESSIBILITY FROM THE TI CORE-LEVEL OF TITANIUM CARBONITRIDE MXENE 44

CONTENTS (Continued)

Page

5.1 Introduction 45

5.2 Experimental and calculation approaches.. 47

5.3 The experimental results 48

5.3.1 Characterization of Ti_3CNT_x and $Ti_3C_2T_x$ by XPS 48

5.3.2 Analysis of the photoemission data 52

5.3.2.1 Determining the potassium concentrations by Ti 3p and K 3p core-level spectra.. 52

5.3.2.2 The extraction of the Ti 3p core-level and valence band shifts upon potassium doping 59

5.3.3 Results of the chemical potential shifts of potassium doped Ti_3CNT_x and $Ti_3C_2T_x$ by UPS measurement 61

5.4 Density functional theory (DFT) calculations 65

5.4.1 Ti 3p core-level and valence band shifts calculation.......................... 65

5.4.2 Density of states (DOS) calculation.. 71

5.4.3 Charge density difference and Bader charge calculation ……..…….74

5.4.4 The effect of carbon and nitrogen distribution on the structural and electronic structure of titanium carbonitride 77

VI CONCLUSION 80

REFERENCES 82

CURRICULUM VATAE 94

LIST OF FIGURES

Figure **Page**

1.1 MAX and MXene families: With a combination of 12 transition metals (red), 12 group A elements (blue), and 2 X elements (grey), about of 100 MAX phases of M_2AX, M_3AX_2, or M_4AX_3 structures have been reported to date. By selective etching of A element from MAX phases, about 30 MXenes have been synthesized (green) and many more theoretically predicted (Hantanasirisakul et al., 2018) …………..…………..….2

1.2 Schematic illustration of MXene structure. MXenes possess excellence electrical conductivity from a conductive carbide core along with transition metal oxide-like surfaces. Intercalated water molecule enables high accessibility of protons to the redox-active sites (Lukatskaya et al., 2017) ……3

2.1 (a)-(c) SEM images of d-Ti_3CNT_x flakes for the LiF + HCl with and without sonication. (d), (e) SEM images of delaminated Ti_3CNT_x flakes for HF + TMAOH and HF + TBAOH with sonication. (f) Cross-section SEM image of d-Ti_3CNT_x free-standing film (Hantanasirisakul et al., 2019) ……….……....6

2.2 (a) TEM image of the Ti_3CNT_x single flake. (b) the selected area electron diffraction (SAED) pattern determining typical hexagonal symmetry of the Ti_3CNT_x flake (Hantanasirisakul et al., 2019) …………………………………7

2.3 Survey scan and XPS spectra of Ti_3CNT_x including Ti 2p, C 1s, N 1s, O 1s, F 1s, and Al 2p (Hantanasirisakul et al., 2019) ………………………….…..…8

LIST OF FIGURES (Continued)

Figure **Page**

2.4 Schematic guidance for $Ti_3C_2T_x$ synthesis from Ti_3AlC_2 (Alhabeb et al., 2017) ……10

2.5 (a) – (c) XPS peak fitting of as-prepared $Ti_3C_2T_x$, (a) Ti 2p, (b) C 1s, (c) O 1s, and 1s before sputtering and (e) Ti 2p, (f) C 1s, (g) O 1s, and (h) F 1s after sputtering (Halim et al., 2016) ……11

2.6 Synthesis and processing of 2D MXene flakes: (a) Selective etching of MAX powder results in a multilayer MXene powder as shown in (b) which can be subsequently delaminated by intercalation and/or sonication (c). The resulting delaminated MXene solution can be processed in many ways including filtration, spray or spin coating, writing, stamping, electrophoresis, and composite as shown in (d) (Hantanasirisakul et al., 2019) ……14

2.7 Total and partial DOS of Ti 3d, C 2p, N 2p, and O 2p for (a) Ti_3CN, (b) $Ti_3CN(OH)_2$, and comparison the total and PDOS for $Ti_3C_{2-x}N_x(OH)_2$ with various C/N ratio of (c) $Ti_3C_{1.5}N_{0.5}(OH)_2$, (d) $Ti_3CN(OH)_2$, and (e) $Ti_3C_{0.5}N_{1.5}(OH)_2$. The total DOS, PDOS of Ti 3d, PDOS of C 2p, PDOS of N 2p, and PDOS of O 2p are shown in black line, grey color, green color, blue color, and red color, respectively (Enyashin et al., 2013) ……16

LIST OF FIGURES (Continued)

Figure **Page**

2.8 Total and partial DOS of Ti 3d, C 2p, N 2p, and O 2p for (a) Ti_3C_2, (b) Ti_3N_2, (c) $Ti_3C_2(OH)_2$, and (d) $Ti_3N_2(OH)_2$. The total DOS, PDOS of Ti 3d, PDOS of C 2p, PDOS of N 2p, and PDOS of O 2p are shown in black line, grey color, green color, blue color, and red color, respectively (Enyashin et al., 2013) ..…………………………………………18

2.9 CV profiles of Ti_3C_2, HND, PDN, and Ti_3CN electrode recorded at scan rate 100 mV s^{-1} (Lu et al., 2020) ………………………………………19

2.10 Comparison of the electrical conductivity between Ti_3CNT_x and $Ti_3C_2T_x$ as a function of annealing temperature (Iqbal et al., 2020) ………………...…20

2.11 Composition of the total EMI SE (SE_T) of 40-μm Ti_3CNT_x and $Ti_3C_2T_x$ films annealed at different temperatures (Iqbal et al., 2020) ……………....…21

2.12 Comparison of ΔSE_T, ΔSE_R, and ΔSE_A of 40-μm Ti_3CNT_x film shown as a function of annealed at different temperatures (Iqbal et al., 2020) …….……..22

2.13 The data plot of the EMI SE_T versus thickness of a comparison the EMI SE_T of annealed films and materials reported in published works. At comparable thickness, the annealed Ti_3CNT_x MXene shows the highest EMI SE_T than these materials (Iqbal et al., 2020) ……………………...………………..23

LIST OF FIGURES (Continued)

Figure **Page**

2.14 (a) CV profiles shown at different scan rates of $Ti_3C_2T_x$ electrode in 1M H_2SO_4. (b) Comparison of electrochemical performances of $Ti_3C_2T_x$ electrode between Ghidiu et al., 2014 and other published works (Ghidiu et al., 2014) ………………………………………………………..….24

2.15 (a) CV profiles collected in *in situ* XAS electrochemical cell at 1 mV s^{-1} in 1 M H_2SO_4 electrolyte. Ti K-edge XANES spectra were collected, (b) between 0.3 and -0.35 V and (c) between -0.2 and 0.35 V (vs Ag/AgCl), (d) variation of Ti edge energy vs potential during full potential sweep between -0.35 and 0.35 V (Lukatskaya et al., 2015) ……………..……25

2.16 (a) Comparison the EMI SE between $Ti_3C_2T_x$ MXene, Copper, Aluminum, and other MXenes showing that $Ti_3C_2T_x$ lies above these materials. (b) Schematic of mechanism for the EMI shielding of $Ti_3C_2T_x$ MXene (Zhahzad et al., 2016) …………………………………………………….……...26

3.1 (a) ARPES measurements of the dispersion of 2DEG states formed along of **Γ** – K direction. (b) Corresponding the evolution of valence band splitting at K point. (c) Binding energy shift of the valence states indicate a decrease in binding energy with increasing electron density (Riley et al., 2015) ………...29

LIST OF FIGURES (Continued)

Figure **Page**

3.2 Electronic band dispersion of $(Sr_{1-x}La_x)_3Ir_2O_7$ indicating to the evolution of a decrease in binding energy of valence band states upon increasing the doping level x (He et al., 2015) ……………………………………………..….30

3.3 (a) Valence band spectra of $Bi_{0.95}La_{0.05}FeO_3$ indicating the shift in binding energy position to lower binding energy at 5mins UV and 5mins zeroth order light irradiation. (b) Summarize the binding energy shift of the O 2p state as a function of light dose (Nathabumroong et al., 2020) ……...……..…31

4.1 Schematic illustration of the three-step and one-step model for interpretation the possibility of photoemission process (Hüfner, 1995) …………………..….35

4.2 The universal curve of inelastic mean free path of electron in solids as a function of kinetic energy. This figure is adapted from the published work of Seah and Dench, 1979 (Seah and Dench, 1979) ………………..…….36

4.3 (a) Schematic illustration of UPS system, consisting of incident photon light, sample, and electron analyzer. (b) Real equipment of high energy resolution UPS beamline at the Advanced Light Source (ALS), USA ………….........37

4.4 Relationship between the electronic structure of a solid system (bottom-left) and its photoemission spectrum (top-right). Electrons with binding energy (BE) can be excited to above the vacuum level (E_{vac}) by photons with energy hv > BE + **Φ** (Lv et al., 2019) ………………………………………...40

LIST OF FIGURES (Continued)

Figure **Page**

4.5 UPS spectrum of a poly-crystalline Au sample shown as a function of binding energy for 0 (Fermi level) to 100 eV. The valence band, Au 5d, and Au 5p core- level are clearly observed. This figure is adapted from the published work of Reinert and Hüfner, 2005 (Reinert and Hüfner, 2005) ……………………………………………..……..41

5.1 Atomic structure of Ti_3CNT_x, composed of stacking three Ti layers interleaved with two alternately mixed C and N layers, as well as terminated by surface terminations (T_x) layers ……..……..…………………..50

5.2 X-ray photoelectron spectra of Ti_3CNT_x MXene. (a) Survey scan assigned to the peak Ti 3p, Cl 2p, C 1s, N 1s, Ti 2p, O 1s, and F 1s core- level spectra. (b) The Ti 2*p* core-level fitted by the four pairs of doublets correspond to spin-orbit splitting of the Ti $2p_{1/2}$ and Ti $2p_{3/2}$. (c)-(d) The C 1s and N 1s core-level XPS spectra of Ti_3CNT_x, respectively. For the C 1*s* core-level, the four fitting peaks are assigned to $C{-}Ti{-}T_x$, C−C, C−O and O−C=O bonds and for the N 1*s* core-level, the three fitting peaks are assigned to $N{-}Ti{-}T_x$, N−O−Ti, and $N{-}TiO_x$ bonds ……………………...………………..50

LIST OF FIGURES (Continued)

Figure **Page**

5.3 (a) Atomic structure, (b) survey scan and high-resolution (c) Ti 2p and (d) C 1s core- level spectra of $Ti_3C_2T_x$. The peaks in the survey scan are assigned to Ti 3p, Cl 2p, C 1s, Ti 2p, O 1s, and F 1s core-level spectra. For the Ti 2p, four pairs doublets correspond to spin-orbit splitting of the Ti $2p_{1/2}$ and Ti $2p_{3/2}$ were fitted ……………………….…………..……52

5.4 K 3p core-level spectra of (a) Ti_3CNT_x and (b) $Ti_3C_2T_x$ samples, shown in a function of potassium deposition time ……………………..………..……55

5.5 (a), (c) The integrated intensities under the areas of Ti 3p (green color) and K 3p (blue color) core-level spectra for Ti_3CNT_x and $Ti_3C_2T_x$ respectively. (b), (d) Corresponding the relative ratio of Ti to K (red color) as a function of potassium deposition time of the Ti_3CNT_x and $Ti_3C_2T_x$ respectively ……...56

5.6 The estimated electron density of Ti_3CNT_x ……………………………….……..57

5.7 The estimated electron density of $Ti_3C_2T_x$ ………………………………..……58

5.8 (a), (d) UPS spectra of the Ti 3p core-level and valence band of the Ti_3CNT_x as a function of potassium deposition time. (b), (c) and (e), (f) The example of Gaussian fitting at Ti 3p core-level and valence band, respectively ……………..…...60

5.9 (a), (d) UPS spectra of the Ti 3p core-level and valence band of the $Ti_3C_2T_x$ as a function of potassium deposition time. (b), (c) and (e), (f) The example of Gaussian fitting at Ti 3p core-level and valence band, respectively …………………60

LIST OF FIGURES (Continued)

Figure **Page**

5.10 (a) Angle-integrated photoemission spectra and evolution of the chemical potential shift ($\Delta\mu$) of (b) Ti 3p core-level and (c) VB, shown in a function of electron density for Ti_3CNT_x 62

5.11 (a) Angle-integrated photoemission spectra and evolution of the chemical potential shift ($\Delta\mu$) of (b) Ti 3p core-level and (c) VB, shown in a function of electron density for $Ti_3C_2T_x$ 63

5.12 Reproducibility of the UPS data of the *in situ* K deposition in Ti_3CNT_x surface measured at Beamline 3.2Ua of the Synchrotron Light Research Institute, Thailand. Black and green diamond symbols indicate spectral peaks of (a) Ti 3p core-level and (c) VB, respectively 64

5.13 Reproducibility of the UPS data of the *in situ* K deposition on $Ti_3C_2T_x$ surface measured at MERLIN beamline 4.0.3 of the Advanced Light Source, USA. Black and green triangle symbols indicate spectral peaks of (a) Ti 3p core-level and (c) VB, respectively 64

LIST OF FIGURES (Continued)

Figure **Page**

5.14 Summary of the chemical potential shift ($\Delta\mu$) of Ti 3*p* core-level and VB for UPS measurement of Ti_3CNT_x versus DFT calculation of Ti_3CNO_2. Green and yellow markers represent the $\Delta\mu$ of experimental data for Ti 3p core-level and VB, respectively. Error bars of the experimental data reflect the uncertainty in determining the peak energy position. Green and yellow solid lines represent the $\Delta\mu$ of calculation data for Ti 3p core-level and VB, respectively ………………………………………………………………..…….67

5.15 DFT calculations of the Ti 3p core-level and valence band shifts considering the effect of the nitrogen content in the Ti_3CNO_2 structure ….….68

5.16 Summary of the chemical potential shift ($\Delta\mu$) of Ti 3p core-level and VB for UPS measurement of $Ti_3C_2T_x$ versus DFT calculation of $Ti_3C_2O_2$. Green and yellow markers represent the $\Delta\mu$ of experimental data for Ti 3p core-level and VB, respectively. Error bars of the experimental data reflect the uncertainty in determining the peak energy position. Green and yellow solid lines represent the $\Delta\mu$ of calculation data for Ti 3p core-level and VB, respectively ……………………………………………………………………69

5.17 Comparison of the calculated changes of the Fermi level upon increasing the electron density between Ti_3CNO_2 (red line) and $Ti_3C_2O_2$ (blue line) …....70

LIST OF FIGURES (Continued)

Figure **Page**

5.18 Comparison of the calculated density of states (DOS) near the E_F between Ti_3CNO_2 and $Ti_3C_2O_2$. The total DOS and that of Ti, C, N and O are presented by grey, green, black, blue, and red colors, respectively. The E_F is set to 0 eV ……………………………………………………….………..72

5.19 The full DOS covering the near E_F and valence band states of energy -7 to 0.5 eV of Ti_3CNO_2 and $Ti_3C_2O_2$ ………………………………….…..……73

5.20 The calculated charge density difference of (a) Ti_3CNO_2 and (b) $Ti_3C_2O_2$ upon electron doping of 0.5*e* per supercell. Both (a) and (b) are shown with the same isosurface level of 0.0005. The charge accumulation region is displayed in yellow color while the charge loss region is in light blue color ……………………………………………………………………………......…75

5.21 The relaxed structure of Ti_3CNO_2 shown in (a) separately C/N, (b) alternately mixed C/N, and (c) randomly mixed C/N, respectively ……......78

5.22 DFT calculations of the Ti 3p core-level and valence band shifts of (a)separately C/N atoms and (b) randomly mixed C/N atoms for Ti_3CNO_2 structures ………………………………………………………………………79

LIST OF TABLES

Table **Page**

2.1 XPS peak fitting and peaks assignment of the Ti_3CNT_x (Hantanasirisakul et al., 2019) ………..………..………………………...9

2.2 XPS peak fitting for as-prepared $Ti_3C_2T_x$ before sputtering (Halim et al., 2016) …………………………………………………..…..12

2.3 XPS peak fitting for as-prepared $Ti_3C_2T_x$ after sputtering (Halim et al., 2016) ………………………………………..……..……..12

5.1 Results of the K concentrations for *in situ* K deposition on Ti_3CNT_x surface (adapted from (Jindata et al., 2021))……….…………………………………….57

5.2 Results of the K concentrations for *in situ* K deposition on $Ti_3C_2T_x$ surface (adapted from (Jindata et al., 2021))……………………………………..…..…58

5.3 The calculated DOS at the E_F ($N(E_F)$) and above the E_F from 0 to 0.5 eV (available states) of Ti, C, N and O atoms in states/eV. The DOS of Ti, C, N and O available states are given as normalized by the total number of each atoms in unit cell (adapted from (Jindata et al., 2021)) ……………………..…74

5.4 The Bader charge and summary of the percentage of charge density distribution on surface Ti, middle Ti, C, N and O atoms in Ti_3CNO_2 (and $Ti_3C_2O_2$) supercell for 16 (16) atoms, 8 (8) atoms, 8 (16) atoms, 8 (-) atoms and 16 (16) atoms of surface Ti, middle Ti, C, N, O, respectively (adapted from (Jindata et al., 2021)) …………………………………….…77

LIST OF TABLES (Continued)

Table **Page**

5.5 The calculated total ground state energy for the different types of C/N atoms in the X layers of Ti_3CNO_2 structures (Jindata et al., 2021) …..……….78

CHAPTER I

INTRODUCTION

1.1 Motivation

1.1.1 2D transition metal carbides, carbonitrides, and nitrides (MXenes)

Since the discovery of the first two-dimensional (2D) titanium carbide ($Ti_3C_2T_x$) and other carbonitrides and nitrides in 2011, the research study on MXenes is started in 2012 which leads to a breakthrough in many applications spanning through energy storage and harvesting, electromagnetic interference (EMI) shielding, electronics and optoelectronics, optics, environmental, biomedicines, sensors, and catalysis (VahidMohammadi et al., 2021). Since then, MXenes have become a large and quickly growing family of 2D materials. MXenes have a general formula of $M_{n+1}X_nT_x$, where M is the early transition metal (Ti, Y, Sc, Zr, Hf, V, Nb, Ta, Cr, Mo, or W), X can be either carbon and/or nitrogen, and n = 1–4. The T_x represents the surface termination that are mostly of −O, −F, and −OH. To date, most of MXenes have been experimentally synthesized with a versatile transition metals and surface chemistry by selective etching of the A layers from their precursor as typically called MAX phases, for example Ti_2CT_x, Nb_2CT_x, $Ti_3C_2T_x$, Ti_3CNT_x, $Cr_2TiC_2T_x$, $V_4C_3T_x$, and $Mo_2Ti_2C_3T_x$ (figure 1.1).

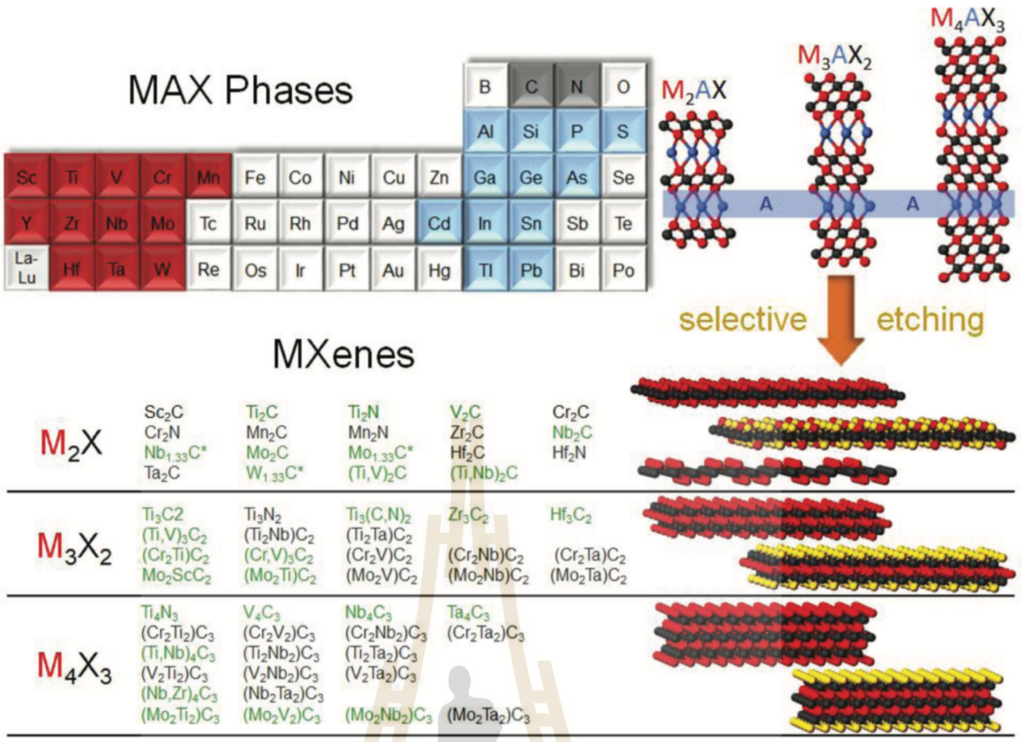
MAX Phases
B C N O
Al Si P S
Sc Ti V Cr Mn Fe Co Ni Cu Zn Ga Ge As Se
Y Zr Nb Mo Tc Ru Rh Pd Ag Cd In Sn Sb Te
La-Lu Hf Ta W Re Os Ir Pt Au Hg Tl Pb Bi Po
M_2AX
M_3AX_2
M_4AX_3
A
A
selective etching
MXenes
M_2X
Sc_2C Cr_2N $Nb_{1.33}C^*$ Ta_2C
Ti_2C Mn_2C Mo_2C $W_{1.33}C^*$
Ti_2N Mn_2N $Mo_{1.33}C^*$ $(Ti,V)_2C$
V_2C Zr_2C Hf_2C $(Ti,Nb)_2C$
Cr_2C Nb_2C Hf_2N
M_3X_2
Ti_3C2 $(Ti,V)_3C_2$ $(Cr_2Ti)C_2$ Mo_2ScC_2
Ti_3N_2 $(Ti_2Nb)C_2$ $(Cr,V)_3C_2$ $(Mo_2Ti)C_2$
$Ti_3(C,N)_2$ $(Ti_2Ta)C_2$ $(Cr_2V)C_2$ $(Mo_2V)C_2$
Zr_3C_2 $(Cr_2Nb)C_2$ $(Mo_2Nb)C_2$
Hf_3C_2 $(Cr_2Ta)C_2$ $(Mo_2Ta)C_2$
M_4X_3
Ti_4N_3 $(Cr_2Ti_2)C_3$ $(Ti,Nb)_4C_3$ $(V_2Ti_2)C_3$ $(Nb,Zr)_4C_3$ $(Mo_2Ti_2)C_3$
V_4C_3 $(Cr_2V_2)C_3$ $(Ti_2Nb_2)C_3$ $(V_2Nb_2)C_3$ $(Nb_2Ta_2)C_3$ $(Mo_2V_2)C_3$
Nb_4C_3 $(Cr_2Nb_2)C_3$ $(Ti_2Ta_2)C_3$ $(V_2Ta_2)C_3$ $(Mo_2Nb_2)C_3$
Ta_4C_3 $(Cr_2Ta_2)C_3$ $(Mo_2Ta_2)C_3$

Figure 1.1 MAX and MXene families: With a combination of 12 transition metals (red), 12 group A elements (blue), and 2 X elements (grey), about of 100 MAX phases of M_2AX, M_3AX_2, or M_4AX_3 structures have been reported to date. By selective etching of the A elements from MAX phases, about 30 MXenes have been synthesized (green) and many more theoretically predicted (Hantanasirisakul et al., 2018).

1.1.2 The unique intrinsic properties of MXenes

As shown in figure 1.2, the structure of MXenes possess the unique intrinsic properties which renders it to have great attention in the research field of energy storage and electronics. Such properties include: (i) a conductive transition metal carbide, carbonitride, and nitride layers enable fast electron to supply to electrochemically active sites; (ii) a transition metal oxide-like surface can generate the redox activity; and (iii) a two-dimensional morphology and pre-intercalated water enable fast ion transport (Lukatskaya et al., 2017).

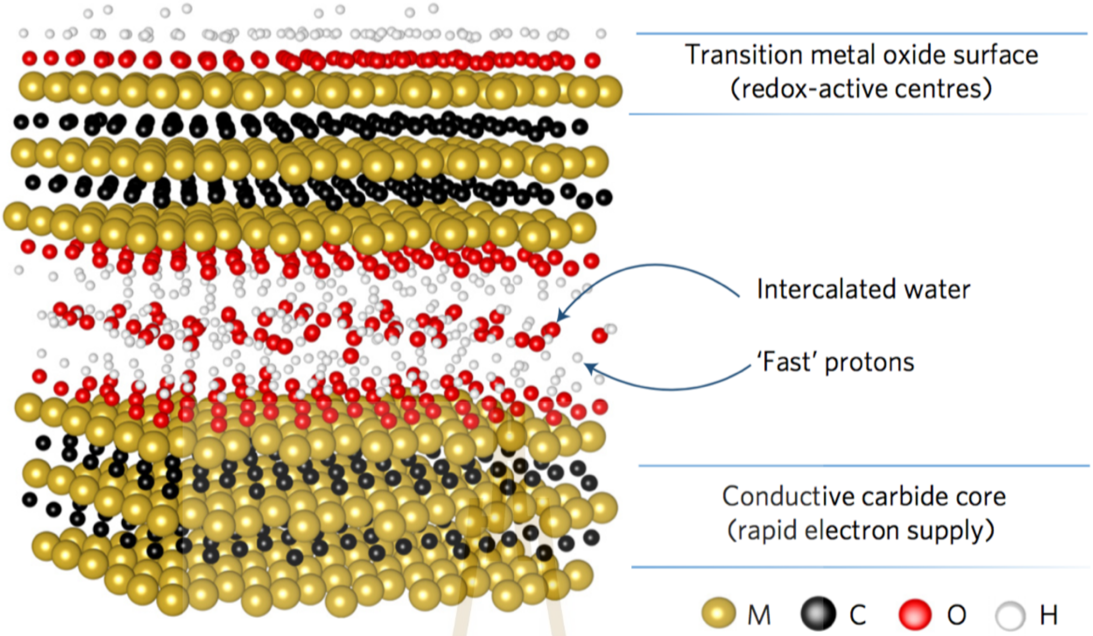
Transition metal oxide surface
(redox-active centres)
Intercalated water
'Fast' protons
Conductive carbide core
(rapid electron supply)
M
C
O
H

Figure 1.2 Schematic illustration of MXene structure. MXenes possess excellence electrical conductivity from a conductive carbide core along with transition metal oxide-like surfaces. Intercalated water molecule enables high accessibility of protons to the redox-active sites (Lukatskaya et al., 2017).

1.2 Thesis outline

This thesis is focused to study on the electronic structures of Ti_3CNT_x and $Ti_3C_2T_x$ MXenes. I have divided the contents in thesis as the following. Chapter II is the literature reviews on the synthesis, characterization, and processing of Ti_3CNT_x and $Ti_3C_2T_x$ MXenes. The experimental studies on the energy storage and EMI shielding applications, as well as the computational studies on the electronic structures of Ti_3CNT_x and $Ti_3C_2T_x$ will also be reviewed in chapter II. In chapter III, the theoretical and experimental studies on negative electronic compressibility (NEC) will be reviewed. In chapter IV, the theoretical and technical backgrounds of photoemission spectroscopy consist of photoelectric effect, photoemission process, ultraviolet photoemission spectroscopy (UPS), and core-level photoemission spectroscopy will be explained. The sample preparation before measuring with UPS and the technical requirements performed during UPS experiments, i.e., potassium evaporation in ultra-high vacuum will also be explained in this chapter.

Chapter V presents my main work on Ti_3CNT_x and $Ti_3C_2T_x$ MXenes. In this chapter, the effect of potassium deposition on the electronic structures difference between Ti_3CNT_x and $Ti_3C_2T_x$ studied by UPS measurement will be presented. The experimental observation on the differences of the chemical potential shift in Ti 3p core-level and the valence band as a function of electron density between Ti_3CNT_x and $Ti_3C_2T_x$ samples will be discussed in this chapter. The part of the density functional theory (DFT) calculation performed in this work will also be discussed in this chapter. Finally, the conclusion will be given in chapter VI.

CHAPTER II

TITANIUM CARBONITRIDE AND TITANIUM CARBIDE

Titanium carbonitride (Ti_3CNT_x) and titanium carbide ($Ti_3C_2T_x$) have shown attractive properties; for example, high electrical conductivity, and versatile surface chemistry. In this chapter, the introduction of Ti_3CNT_x and $Ti_3C_2T_x$ with several methods of synthesis, characterization, and materials processing will be reviewed. The experimental studies on the energy storage and EMI shielding applications of Ti_3CNT_x and $Ti_3C_2T_x$ will be described. In addition, the computational studies on the electronic structures of Ti_3CNT_x and $Ti_3C_2T_x$ will be depicted.

2.1 Synthesis and characterization of titanium carbonitride (Ti_3CNT_x)

Hantanasirisakul et al. (Hantanasirisakul et al., 2019) demonstrated the synthesis of Ti_3CNT_x MXene by selective etching of aluminum (Al) element from their Ti_3AlCN MAX phase powder. The Ti_3AlCN MAX powder was synthesized by heating the mixture elements of Ti, AlN, and graphite with a molar ratio of 3:1:1, respectively, held under the argon (Ar) gas condition (10 ºC min^{-1} to 1500 ºC min^{-1}) for 2 h. A 0.5 g of Ti_3AlCN MAX powder was slowly added to a mixture of LiF and HCl solution, and the solution was stirred at 500 rpm and at 35 °C for 24 h to remove the Al element.

Then, the solution was washed by adding 150 mL of deionized (DI) water and centrifuged at 3500 rpm for 5 min followed by decantation of the clear supernatant. The washing process was repeated four to five times until the pH of the supernatant became close to neutral and the supernatant became dark, as a result of partial delamination of Ti_3CNT_x flakes (d-Ti_3CNT_x). The supernatant consisting of few-layer flakes of Ti_3CNT_x can be characterized by using scanning electron microscopy (SEM) and transmission electron microscopy (TEM) as shown in figures 2.1 and 2.2, respectively.

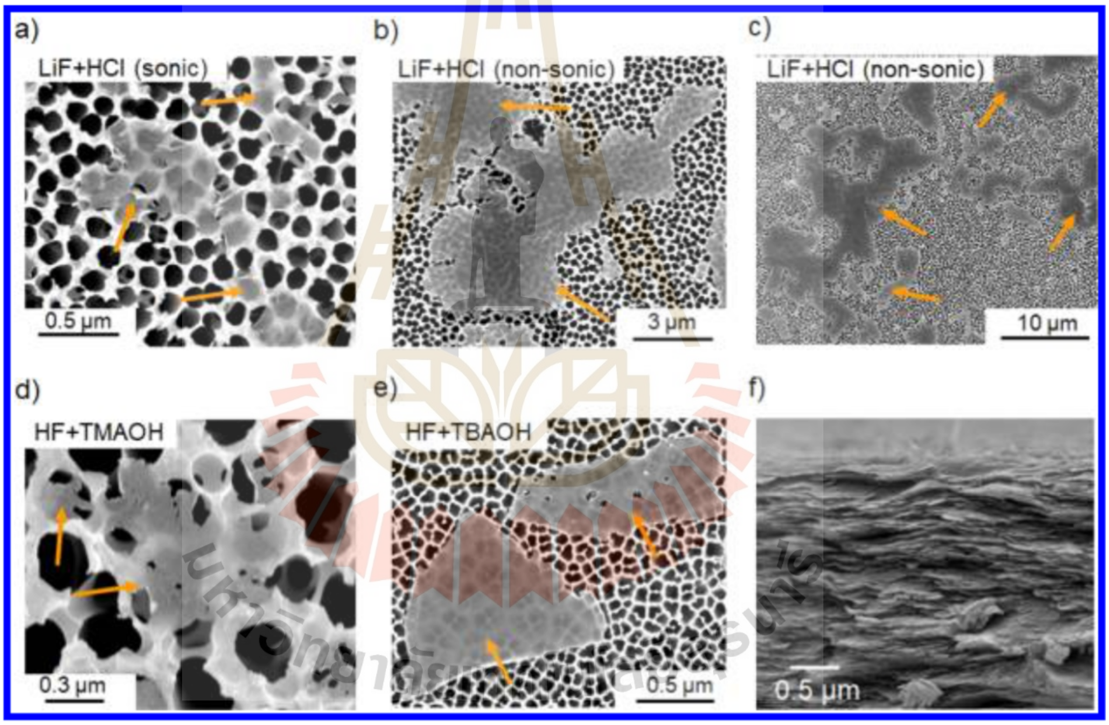
a)
LiF+HCl (sonic)
0.5 µm
b)
LiF+HCl (non-sonic)
3 µm
c)
LiF+HCl (non-sonic)
10 µm
d)
HF+TMAOH
0.3 µm
e)
HF+TBAOH
0.5 µm
f)
0.5 µm

Figure 2.1 (a)-(c) SEM images of d-Ti_3CNT_x flakes for the LiF and HCl with and without sonication. (d), (e) SEM images of delaminated Ti_3CNT_x flakes for HF and TMAOH and HF and TBAOH with sonication. (f) Cross-section SEM image of d-Ti_3CNT_x free-standing film (Hantanasirisakul et al., 2019).

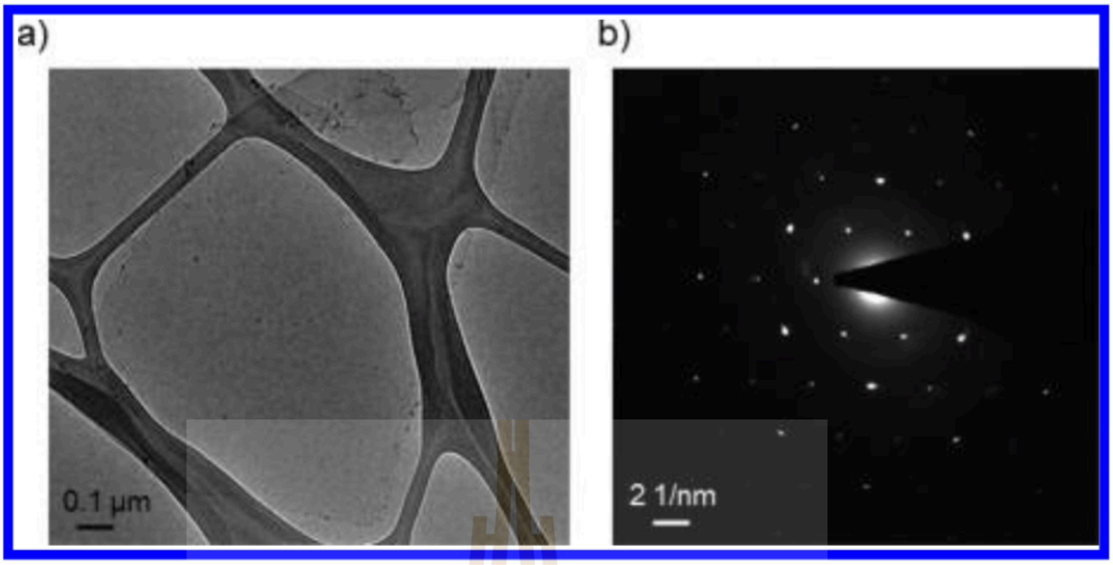

Figure 2.2 (a) TEM image of the Ti_3CNT_x single flake. (b) the selected area electron diffraction (SAED) pattern determining typical hexagonal symmetry of the Ti_3CNT_x flake (Hantanasirisakul et al., 2019).

The chemical composition at the surface and C/N ratio of the Ti_3CNT_x has been characterized by using x-ray photoelectron spectroscopy (XPS). Figure 2.3 shows the XPS spectra of Ti_3CNT_x including; survey scan, Ti 2p, C 1s, N 1s, O 1s, and F 1s core-levels, respectively. The detailed XPS peak fits of all regions are presented in table 2.1. The absence of Al 2p core-level signal confirms a successful etching, washing, and delamination steps for synthesis methods.

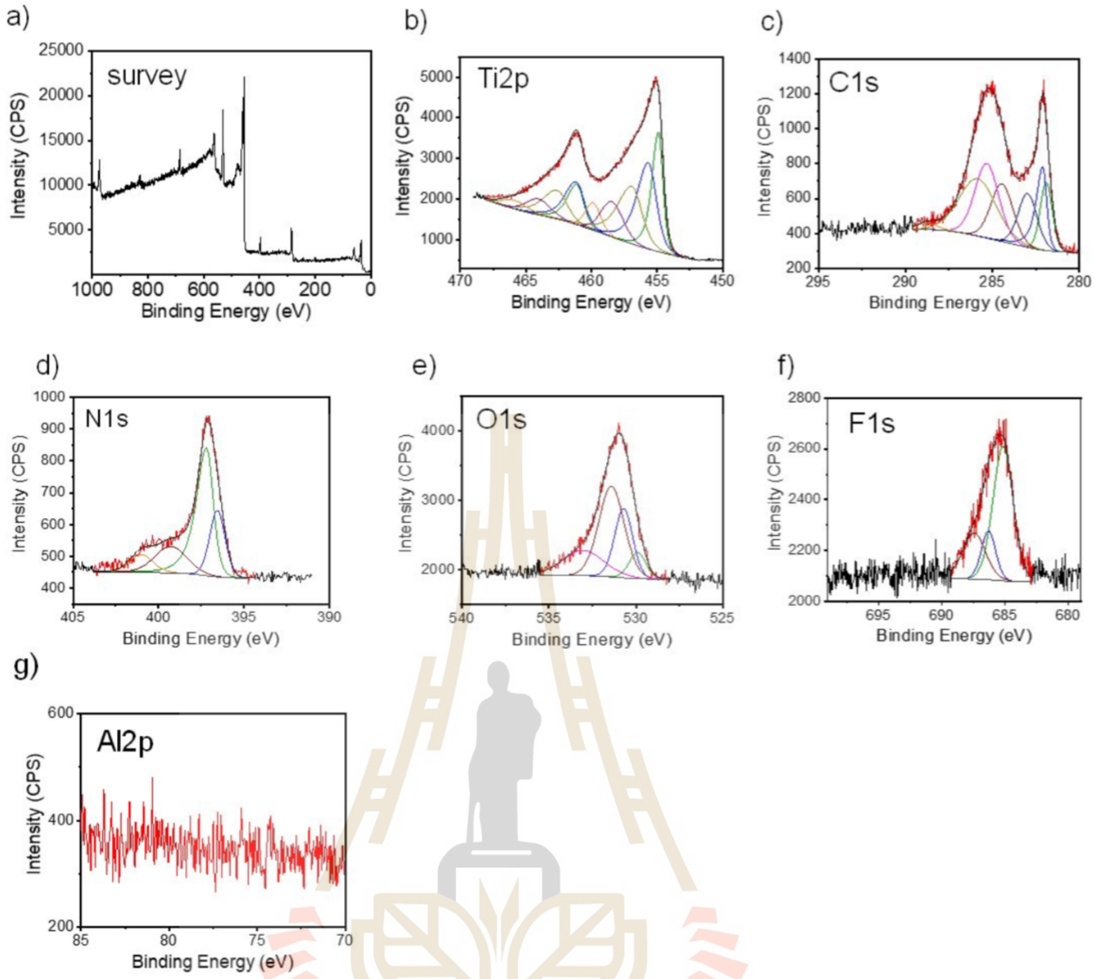

Figure 2.3 Survey scan and XPS spectra of Ti_3CNT_x including Ti 2p, C 1s, N 1s, O 1s, F 1s, and Al 2p core-levels (Hantanasirisakul et al., 2019).

Table 2.1 XPS peak fitting and peaks assignment of the Ti_3CNT_x (Hantanasirisakul et al., 2019).

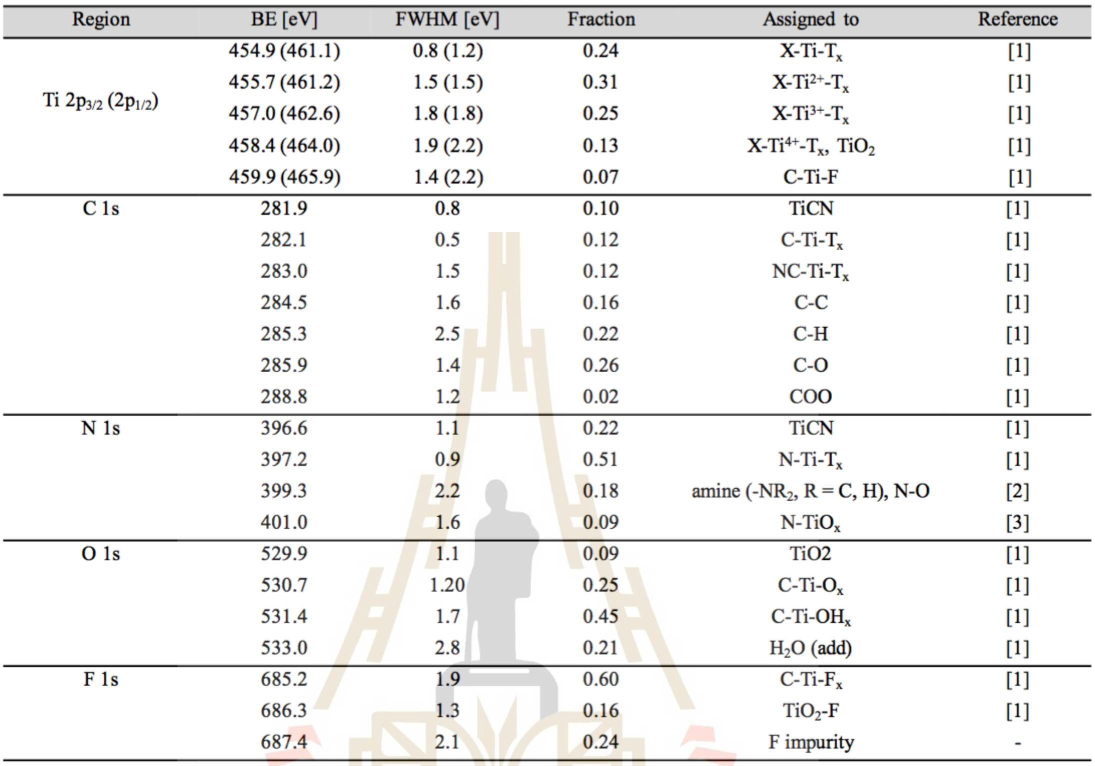

Region	BE [eV]	FWHM [eV]	Fraction	Assigned to	Reference
Ti $2p_{3/2}$ ($2p_{1/2}$)	454.9 (461.1)	0.8 (1.2)	0.24	X-Ti-T_x	[1]
	455.7 (461.2)	1.5 (1.5)	0.31	X-Ti^{2+}-T_x	[1]
	457.0 (462.6)	1.8 (1.8)	0.25	X-Ti^{3+}-T_x	[1]
	458.4 (464.0)	1.9 (2.2)	0.13	X-Ti^{4+}-T_x, TiO_2	[1]
	459.9 (465.9)	1.4 (2.2)	0.07	C-Ti-F	[1]
C 1s	281.9	0.8	0.10	TiCN	[1]
	282.1	0.5	0.12	C-Ti-T_x	[1]
	283.0	1.5	0.12	NC-Ti-T_x	[1]
	284.5	1.6	0.16	C-C	[1]
	285.3	2.5	0.22	C-H	[1]
	285.9	1.4	0.26	C-O	[1]
	288.8	1.2	0.02	COO	[1]
N 1s	396.6	1.1	0.22	TiCN	[1]
	397.2	0.9	0.51	N-Ti-T_x	[1]
	399.3	2.2	0.18	amine (-NR_2, R = C, H), N-O	[2]
	401.0	1.6	0.09	N-TiO_x	[3]
O 1s	529.9	1.1	0.09	TiO2	[1]
	530.7	1.20	0.25	C-Ti-O_x	[1]
	531.4	1.7	0.45	C-Ti-OH_x	[1]
	533.0	2.8	0.21	H_2O (add)	[1]
F 1s	685.2	1.9	0.60	C-Ti-F_x	[1]
	686.3	1.3	0.16	TiO_2-F	[1]
	687.4	2.1	0.24	F impurity	-

2.2 Synthesis and characterization of titanium carbide ($Ti_3C_2T_x$)

Alhabeb et al. (Alhabeb et al., 2017) demonstrated the synthesis of $Ti_3C_2T_x$ MXene by selective etching the Al element from their Ti_3AlC_2 MAX phase powder which shown in a several methods for etching and delaminating processes (figure 2.4). After the complete of synthesis processes, the multilayered flakes of $Ti_3C_2T_x$ can be collected by using minimally intensive layer delamination (MILD) as called MILD-$Ti_3C_2T_x$ via vacuum-assisted filtration method.

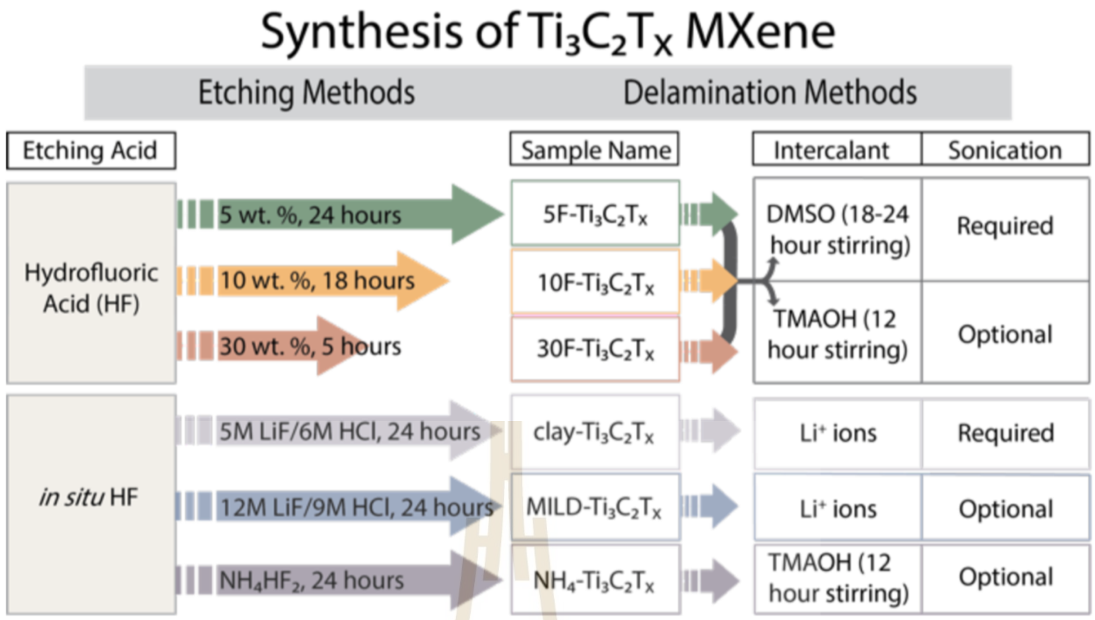
Synthesis of $Ti_3C_2T_X$ MXene
Etching Methods
Delamination Methods
Etching Acid
Sample Name
Intercalant
Sonication
Hydrofluoric Acid (HF)
5 wt. %, 24 hours
10 wt. %, 18 hours
30 wt. %, 5 hours
5F-$Ti_3C_2T_X$
10F-$Ti_3C_2T_X$
30F-$Ti_3C_2T_X$
DMSO (18-24 hour stirring)
Required
TMAOH (12 hour stirring)
Optional
in situ HF
5M LiF/6M HCl, 24 hours
12M LiF/9M HCl, 24 hours
NH_4HF_2, 24 hours
clay-$Ti_3C_2T_X$
MILD-$Ti_3C_2T_X$
NH_4-$Ti_3C_2T_X$
Li⁺ ions
Required
Li⁺ ions
Optional
TMAOH (12 hour stirring)
Optional

Figure 2.4 Schematic guidance for $Ti_3C_2T_x$ synthesis from Ti_3AlC_2 MAX phase (Alhabeb et al., 2017).

Recently, Halim et al. (Halim et al., 2016) reported the differences of the chemical composition and chemical bonding between before and after sputtering of $Ti_3C_2T_x$ surface by using XPS. Figure 2.5 shows the differences of the XPS spectra including; Ti 2p, C 1s, O 1s and F 1s core-levels before and after sputtering. The detailed XPS peak fits of all regions for before and after sputtering are presented in tables 2.2 and 2.3, respectively.

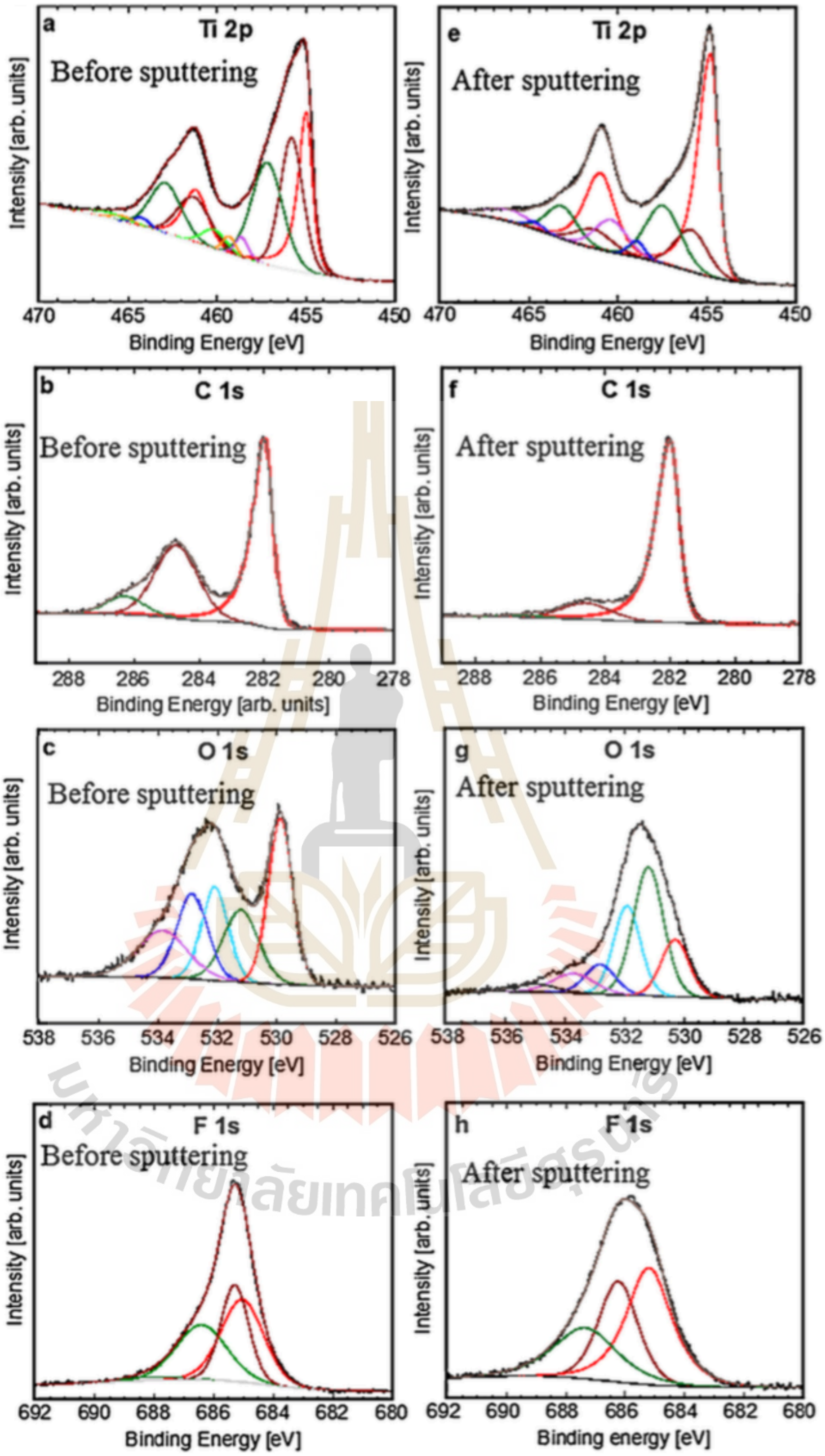

Figure 2.5 (a) – (c) XPS spectra of as-prepared $Ti_3C_2T_x$ before sputtering, (a) Ti 2p, (b) C 1s, (c) O 1s, and F 1s core-levels. (e) – (h) XPS spectra of as-prepared $Ti_3C_2T_x$ after sputtering, (e) Ti 2p, (f) C 1s, (g) O 1s, and (h) F 1s core-levels (Halim et al., 2016).

Table 2.2 XPS peak fitting for as-prepared $Ti_3C_2T_x$ before sputtering (Halim et al., 2016).

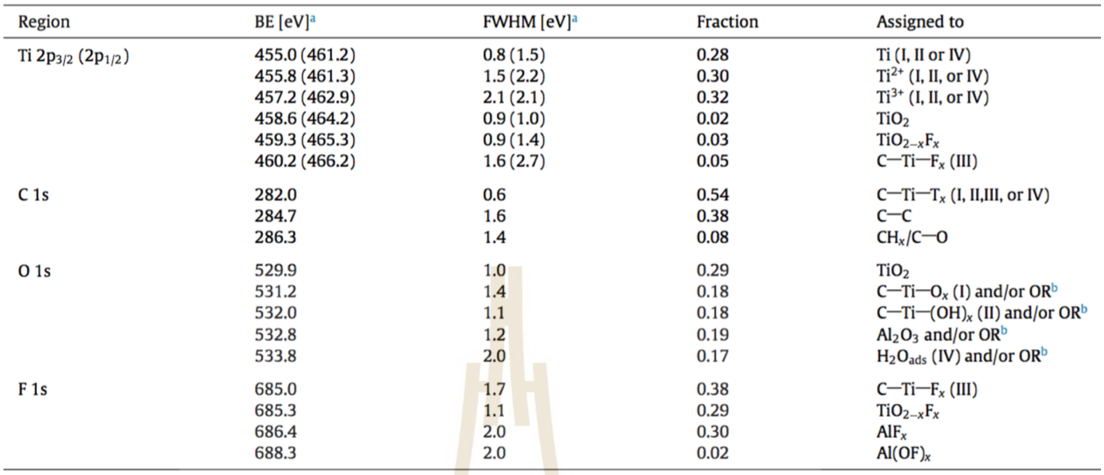

Region	BE [eV][a]	FWHM [eV][a]	Fraction	Assigned to
Ti $2p_{3/2}$ ($2p_{1/2}$)	455.0 (461.2)	0.8 (1.5)	0.28	Ti (I, II or IV)
	455.8 (461.3)	1.5 (2.2)	0.30	Ti^{2+} (I, II, or IV)
	457.2 (462.9)	2.1 (2.1)	0.32	Ti^{3+} (I, II, or IV)
	458.6 (464.2)	0.9 (1.0)	0.02	TiO_2
	459.3 (465.3)	0.9 (1.4)	0.03	$TiO_{2-x}F_x$
	460.2 (466.2)	1.6 (2.7)	0.05	$C—Ti—F_x$ (III)
C 1s	282.0	0.6	0.54	$C—Ti—T_x$ (I, II,III, or IV)
	284.7	1.6	0.38	C—C
	286.3	1.4	0.08	CH_x/C—O
O 1s	529.9	1.0	0.29	TiO_2
	531.2	1.4	0.18	$C—Ti—O_x$ (I) and/or OR[b]
	532.0	1.1	0.18	$C—Ti—(OH)_x$ (II) and/or OR[b]
	532.8	1.2	0.19	Al_2O_3 and/or OR[b]
	533.8	2.0	0.17	H_2O_{ads} (IV) and/or OR[b]
F 1s	685.0	1.7	0.38	$C—Ti—F_x$ (III)
	685.3	1.1	0.29	$TiO_{2-x}F_x$
	686.4	2.0	0.30	AlF_x
	688.3	2.0	0.02	$Al(OF)_x$

Table 2.3 XPS peak fitting for as-prepared $Ti_3C_2T_x$ after sputtering (Halim et al., 2016).

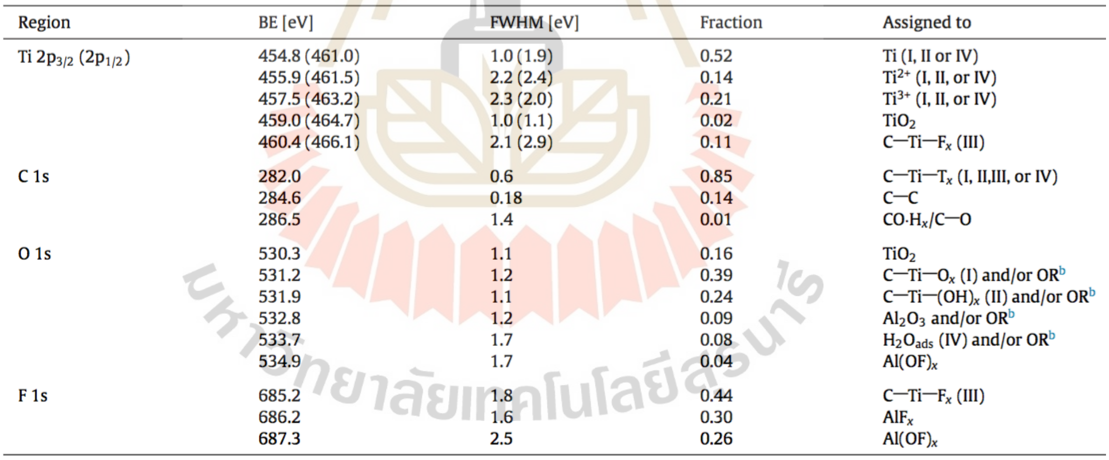

Region	BE [eV]	FWHM [eV]	Fraction	Assigned to
Ti $2p_{3/2}$ ($2p_{1/2}$)	454.8 (461.0)	1.0 (1.9)	0.52	Ti (I, II or IV)
	455.9 (461.5)	2.2 (2.4)	0.14	Ti^{2+} (I, II, or IV)
	457.5 (463.2)	2.3 (2.0)	0.21	Ti^{3+} (I, II, or IV)
	459.0 (464.7)	1.0 (1.1)	0.02	TiO_2
	460.4 (466.1)	2.1 (2.9)	0.11	$C—Ti—F_x$ (III)
C 1s	282.0	0.6	0.85	$C—Ti—T_x$ (I, II,III, or IV)
	284.6	0.18	0.14	C—C
	286.5	1.4	0.01	$CO·H_x$/C—O
O 1s	530.3	1.1	0.16	TiO_2
	531.2	1.2	0.39	$C—Ti—O_x$ (I) and/or OR[b]
	531.9	1.1	0.24	$C—Ti—(OH)_x$ (II) and/or OR[b]
	532.8	1.2	0.09	Al_2O_3 and/or OR[b]
	533.7	1.7	0.08	H_2O_{ads} (IV) and/or OR[b]
	534.9	1.7	0.04	$Al(OF)_x$
F 1s	685.2	1.8	0.44	$C—Ti—F_x$ (III)
	686.2	1.6	0.30	AlF_x
	687.3	2.5	0.26	$Al(OF)_x$

2.3 Materials processing

During the etching process (step 1 in figure 2.6), the strong M-A bonds of MAX phase are replaced by a weak van der Waals bond of MXenes. The delamination process including; intercalation, sonication, and shaking are essential to obtain a mono- or few-layer MXene flakes (step 2 in figure 2.6). However, the intercalation and sonication processes are mostly used for delamination of MXenes. This is achieved by intercalating with cations and followed by sonication method that causing in the expanding in the MXenes interlayers. For the shaking process, it is used to separate the MXenes layers of intercalated MXenes when we desired the high quality of flake size and concentration of MXene solution. This solution can be processed in different methods, for example; vacuum filtration to form free-standing MXene paper, spin or spray coating, writing, stamping, electrophoresis, and composites (step 3 in figure 2.6).

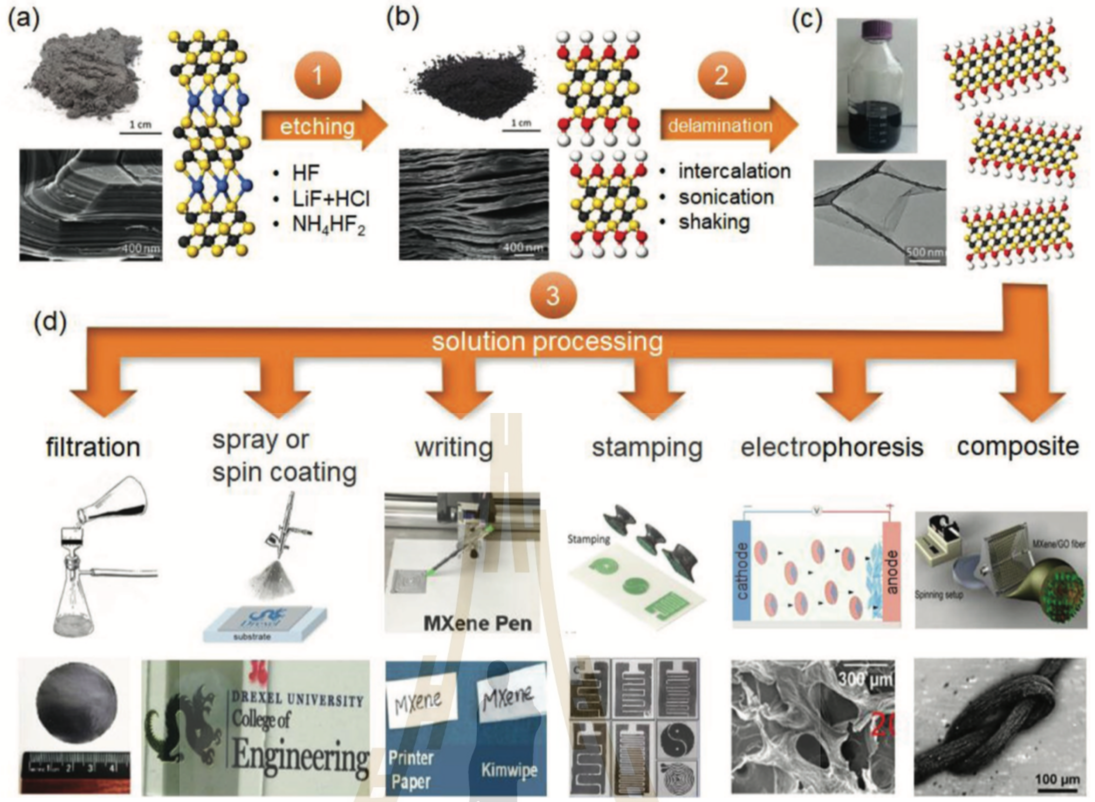
(a)
1 cm
400 nm
1
etching
• HF
• LiF+HCl
• NH₄HF₂
(b)
1 cm
400 nm
2
delamination
• intercalation
• sonication
• shaking
(c)
500 nm
3
(d)
solution processing
filtration
spray or
spin coating
writing
stamping
electrophoresis
composite
substrate
MXene Pen
Stamping
cathode
anode
MXene/GO fiber
Spinning setup
DREXEL UNIVERSITY
College of
Engineering
MXene
MXene
Printer
Paper
Kimwipe
300 μm
100 μm

Figure 2.6 Synthesis and processing of 2D MXene flakes. (a) Selective etching of MAX powder results in a multilayer MXene powder as shown in (b) which can be subsequently delaminated by intercalation and/or sonication (c). The resulting delaminated MXene solution can be processed in many ways including filtration, spray or spin coating, writing, stamping, electrophoresis, and composite as shown in (d) (Hantanasirisakul et al., 2018).

2.4 Electronic structures of Ti_3CNT_x and $Ti_3C_2T_x$

Basically, the electronic structure of MXenes has been predicted by using density functional theory (DFT) calculations. Enyashin et al. (Enyashin et al., 2013) performed the density of state (DOS) calculations in a difference type of titanium carbonitride MXene including Ti_3CN, $Ti_3CN(OH)_2$, $Ti_3C_{1.5}N_{0.5}(OH)_2$, and

$Ti_3C_{0.15}N_{1.5}(OH)_2$ as shown in figures 2.7(a)-2.7(e), respectively. The DOS of Ti_3CN shows the three electronic states including Ti 3d state near the Fermi level (E_F), hybridization of C 2p – Ti 3d states, and hybridization of N 2p – Ti 3d states (figure 2.7(a)). The DOS of $Ti_3CN(OH)_2$ are composed of Ti 3d state near the E_F, the hybridization of C 2p – Ti 3d states, as well as the hybridized and merged between O 2p – Ti 3d and N 2p – Ti 3d states (figures 2.7(b) and 2.7(d)). Note that the Ti_3CN and $Ti_3CN(OH)_2$ exhibit the metallic behavior as it shows the high DOS of Ti 3d state near the E_F. The authors also calculated the DOS of the C/N atomic variation in $Ti_3CN(OH)_2$ structure including $Ti_3C_{1.5}N_{0.5}(OH)_2$ and $Ti_3C_{0.5}N_{1.5}(OH)_2$ as shown in figures 2.7(c) and 2.7(e), respectively. The DOS of $Ti_3C_{1.5}N_{0.5}(OH)_2$ and $Ti_3C_{0.5}N_{1.5}(OH)_2$ are similar to those of $Ti_3CN(OH)_2$ phase (figures 2.7(b) and 2.7(d)), which include four main DOS of the Ti 3d state near the E_F and the hybridization of C 2p –Ti 3d, N 2p – Ti 3d, and O 2p – Ti 3d states. However, it is worthwhile to note that the variation of the DOS of C 2p and N 2p are depended on the ratio of the C/N atom in $Ti_3CN(OH)_2$ structure.

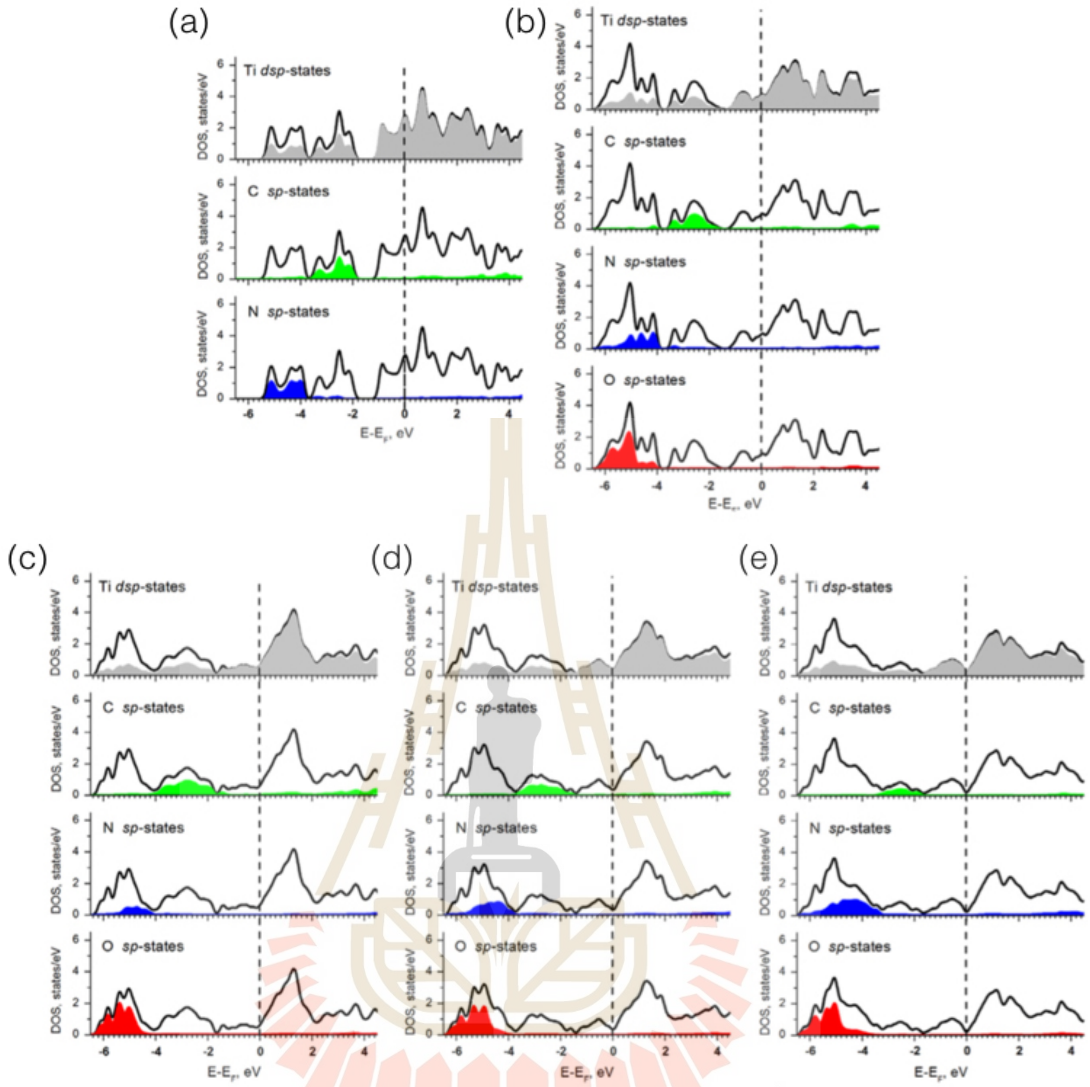

Figure 2.7 Total and partial DOS (PDOS) of Ti 3d, C 2p, N 2p, and O 2p for (a) Ti_3CN, (b) $Ti_3CN(OH)_2$, and comparison the total and PDOS for $Ti_3C_{2-x}N_x(OH)_2$ with various C/N ratio of (c) $Ti_3C_{1.5}N_{0.5}(OH)_2$, (d) $Ti_3CN(OH)_2$, and (e) $Ti_3C_{0.5}N_{1.5}(OH)_2$. The total DOS, PDOS of Ti 3d, PDOS of C 2p, PDOS of N 2p, and PDOS of O 2p are shown in black line, grey color, green color, blue color, and red color, respectively (Enyashin et al., 2013).

Enyashin et al. (Enyashin et al., 2013) also calculated the DOS of titanium carbide and titanium nitride MXenes including Ti_3C_2, Ti_3N_2, $Ti_3C_2(OH)_2$, and $Ti_3N_2(OH)_2$ as shown in figures 2.8(a)-2.8(d), respectively. The Ti_3C_2 shows the DOS of Ti 3d states near the E_F and hybridized states of C 2p – Ti 3d below the E_F (figure 2.8(a)). The high DOS near the E_F is the Ti 3d states, which are responsible for metallic behavior of Ti_3C_2 MXene. The DOS of Ti_3N_2 contains the Ti 3d states near the E_F and hybridized states N 2p – Ti 3d (figure 2.8(b)). Also, the high DOS of Ti 3d states near the E_F indicates the metallic behavior of Ti_3N_2 MXene. The changes in DOS of Ti_3C_2, and Ti_3N_2 after their hydroxylation ($Ti_3C_2(OH)_2$ and $Ti_3N_2(OH)_2$) is the presence of additional O 2p states. As shown in figure 2.8(c), the O 2p states of $Ti_3C_2(OH)_2$ is located below the hybridized of C 2p – Ti 3d states, whereas the O 2p states of $Ti_3N_2(OH)_2$ is partially merged with the hybridized N 2p – Ti 3d states (figure 2.8(d)).

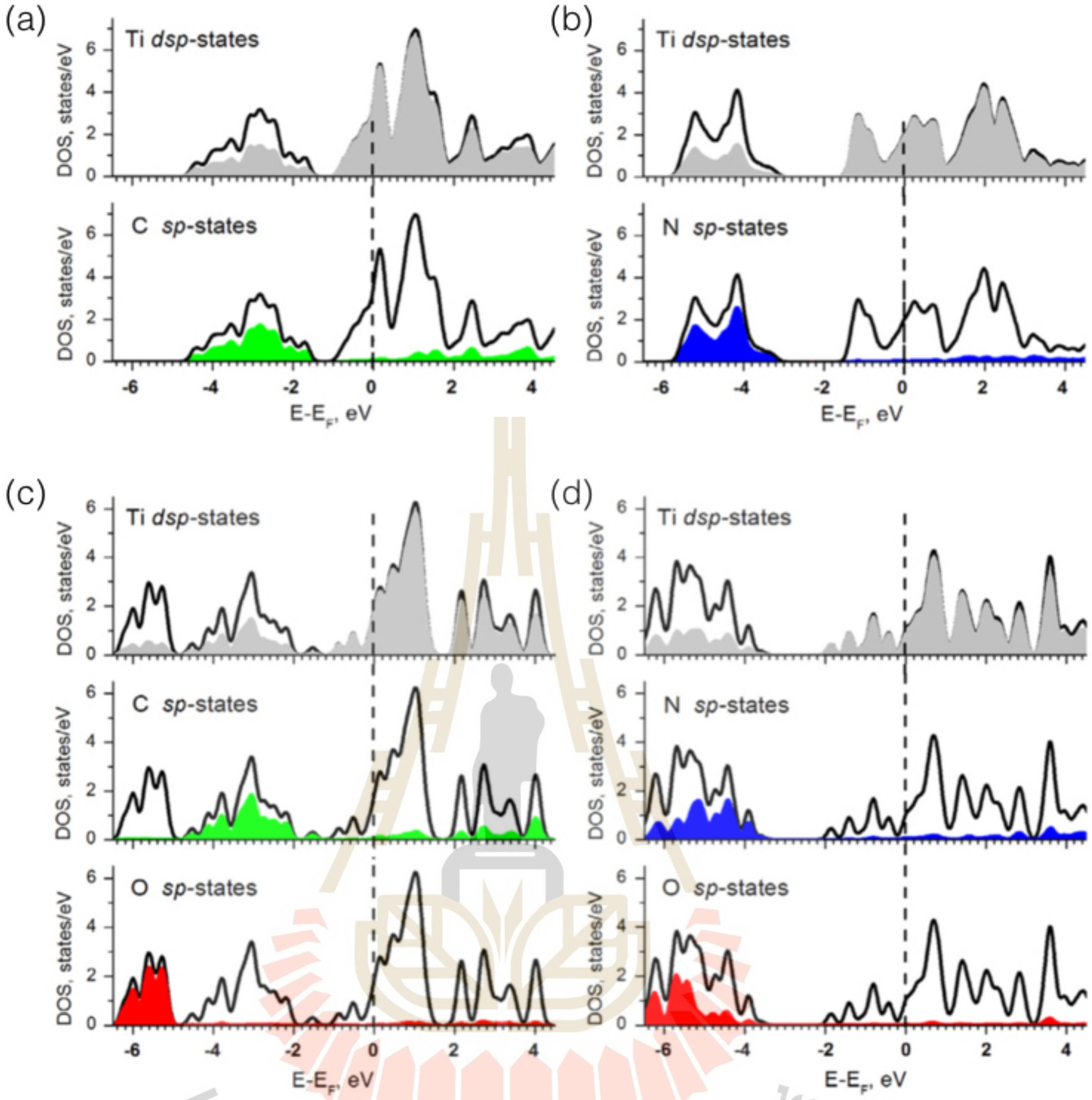

Figure 2.8 Total and PDOS of Ti 3d, C 2p, N 2p, and O 2p for (a) Ti_3C_2, (b) Ti_3N_2, (c) $Ti_3C_2(OH)_2$, and (d) $Ti_3N_2(OH)_2$. The total DOS, PDOS of Ti 3d, PDOS of C 2p, PDOS of N 2p, and PDOS of O 2p are shown in black line, grey color, green color, blue color, and red color, respectively (Enyashin et al., 2013).

2.5 The experimental study of Ti_3CNT_x and $Ti_3C_2T_x$

2.5.1 Energy storage application of Ti_3CNT_x

Lu et al. (Lu et al., 2020) demonstrated the electrochemical test for Ti_3CN, Ti_3C_2, hydrothermal treated pristine Ti_3C_2 (called HND), as well as low vacuum and low temperature treated pristine Ti_3C_2 (called PND) electrodes. The cyclic voltammetry (CV) behaviors of the four MXene electrodes measured at the scan rate of 100 mV s^{-1} are presented in figure 2.9. The features of CV curves suggest that four electrodes do not show the rectangular profile, indicating a strong combination between electrical double-layer capacitance (EDLC) and pseudocapacitive (PC) mechanisms. The key result of this work is, the Ti_3CN electrode is found to have a higher specific capacitance than the pristine Ti_3C_2 electrode, with the capacitance values increased from 76.1 F g^{-1} for Ti_3C_2 to 98.6 F g^{-1} for Ti_3CN electrode at the scan rate of 5 mV s^{-1}.

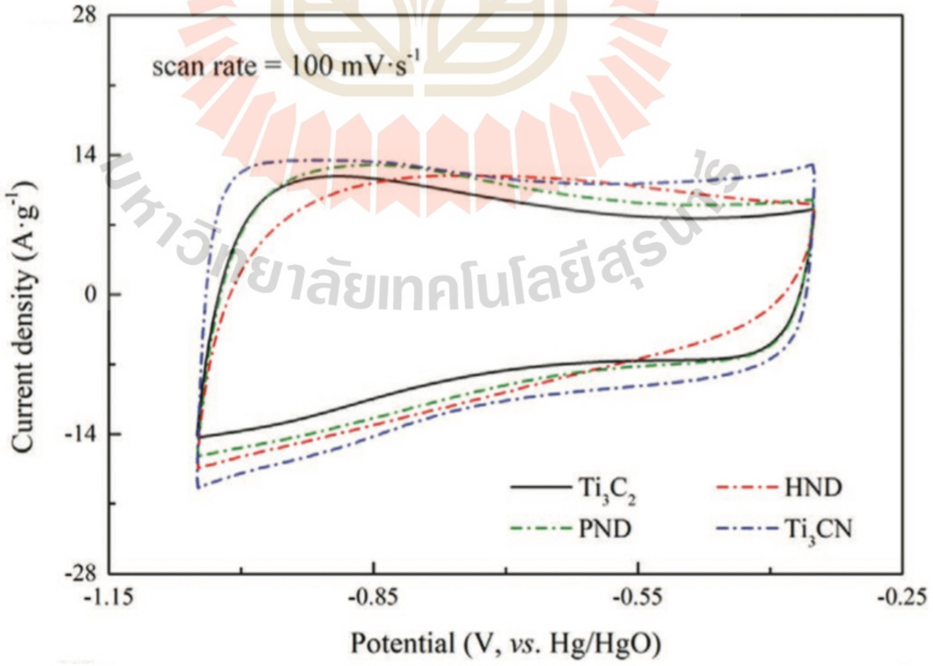

Figure 2.9 CV profiles of Ti_3C_2, HND, PDN, and Ti_3CN recorded at scan rate of 100 mV s^{-1} (Lu et al., 2020).

2.5.2 Electromagnetic interference shielding application of Ti_3CNT_x

Recently, Iqbal et al. (Iqbal et al., 2020) revealed the outstanding performance in electromagnetic interference (EMI) shielding of Ti_3CNT_x achieved by thermal annealing, which can contribute the Ti_3CNT_x having the EMI shielding effectiveness (EMI SE) to be higher than $Ti_3C_2T_x$. Figure 2.10 shows the difference of the electrical conductivity between Ti_3CNT_x (black rectangle) and $Ti_3C_2T_x$ (red triangle) as a function of annealing temperature. The result shows that Ti_3CNT_x has a lower electrical conductivity than $Ti_3C_2T_x$. The as-synthesized Ti_3CNT_x has an average electrical conductivity of 1125 S cm^{-1}, which gradually increases with annealing temperature and reaches a maximum value of 2475 S cm^{-1} at 250°C. However, $Ti_3C_2T_x$ shows the monotonic increase in electrical conductivity from 4500 to 5225 S cm^{-1} with increasing annealing temperature.

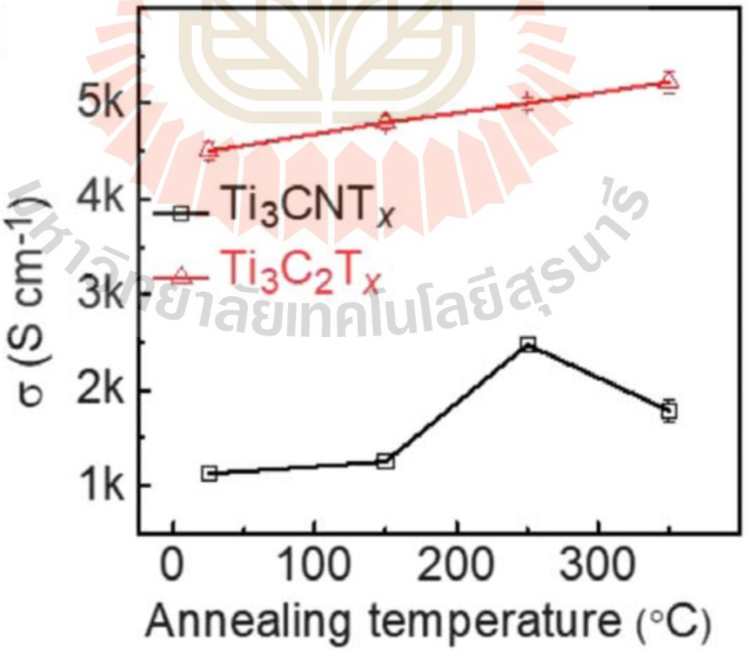

Figure 2.10 Comparison of the electrical conductivity between Ti_3CNT_x and $Ti_3C_2T_x$ as a function of annealing temperature (Iqbal et al., 2020).

Figure 2.11 shows the difference of the total EMI SE (SE_T) of 40-μm-thick between Ti_3CNT_x and $Ti_3C_2T_x$ films after annealing at various temperatures. The as-synthesized Ti_3CNT_x film (room temperature; RT) shows the SE_T of 61 dB, which increases to 77, 99, and 116 dB at annealing temperatures of 150, 250, and 350°C, respectively. The as-synthesized $Ti_3C_2T_x$ (room temperature; RT) shows the SE_T of 84 dB, which gradually increases to 87, 92, and 93 dB after annealing temperatures at 150, 250, and 350°C, respectively.

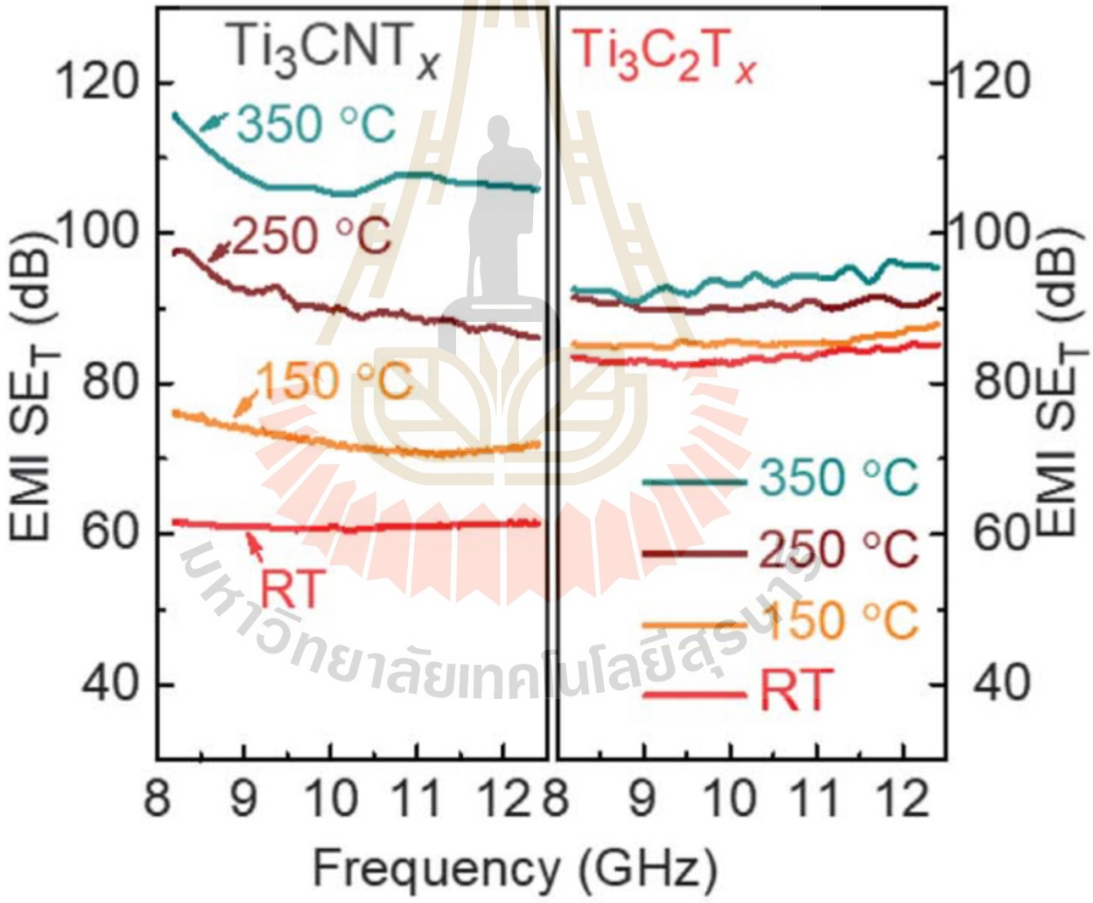

Figure 2.11 Composition of the total EMI SE (SE_T) of 40-μm Ti_3CNT_x and $Ti_3C_2T_x$ films annealed at different temperatures (Iqbal et al., 2020).

We note that the EMI SE values of both MXenes caused by the reflection (SE_R) and the absorption (SE_A). Figure 2.12 shows the changes in SE_T, SE_R, and SE_A values as a function of annealing temperature, which is represented by the increase of ΔSE_T, ΔSE_R, and ΔSE_A, respectively. The SE_T and SE_A of Ti_3CNT_x films rapidly increase with increasing annealing temperature, whereas the SE_R values are almost independent of annealing temperature. In contrast to Ti_3CNT_x, the increase rate in $Ti_3C_2T_x$ is much smaller than that in Ti_3CNT_x at the same annealing conditions.

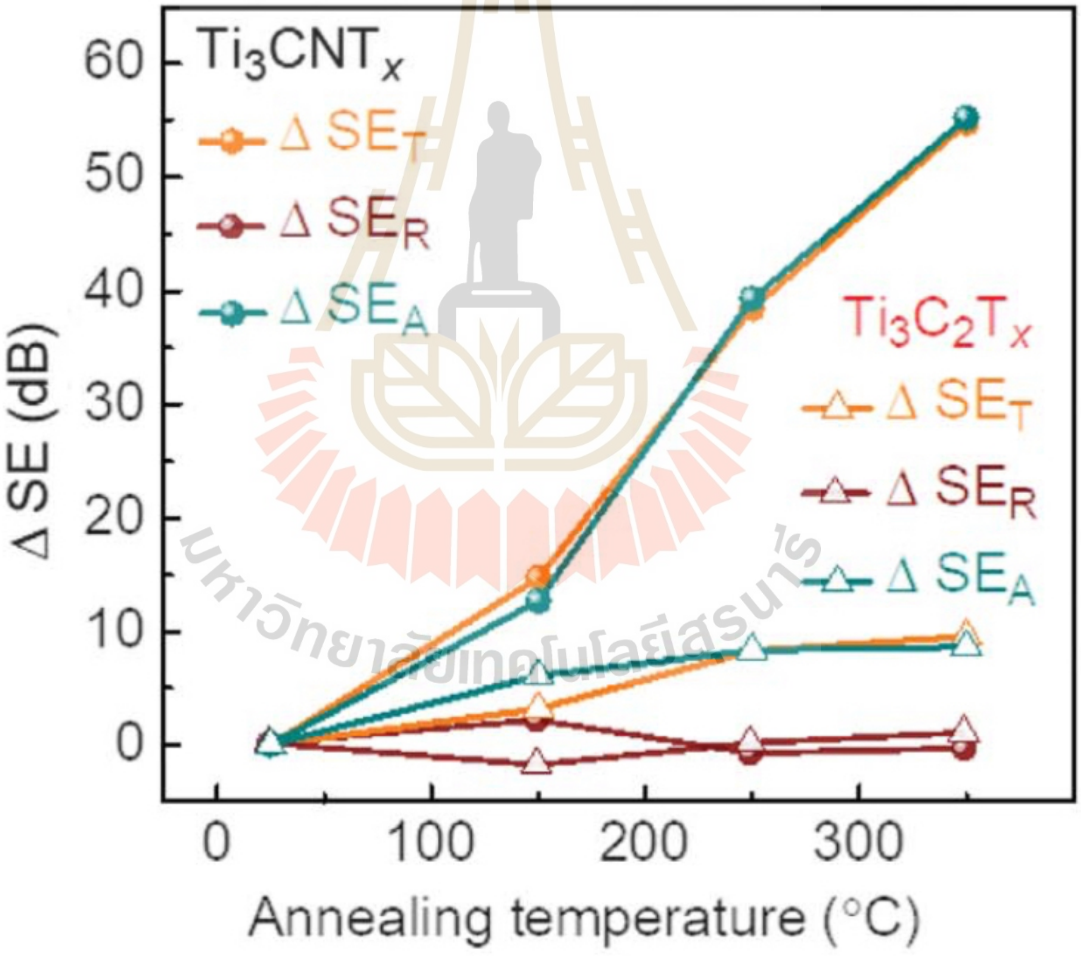

Figure 2.12 Comparison of ΔSE_T, ΔSE_R, and ΔSE_A of 40-μm Ti_3CNT_x film shown as a function of annealed at different temperatures (Iqbal et al., 2020).

The EMI SE_T value of Ti_3CNT_x films is compared with the EMI SE values reported in previous studies as shown in figure 2.13. Metal-based and carbon-based materials have been on the forefront in the last decade, where SE values in excess of 50 dB for a thickness between 50 and 100 mm has been considered sufficient for practical applications. The key finding of this work is, the thermally treated of 40-mm-thick Ti_3CNT_x MXene film exhibits an absorption-dominant EMI SE of 116 dB, exceeding all known materials, which shows its strong potential for EMI shielding and related electronic applications.

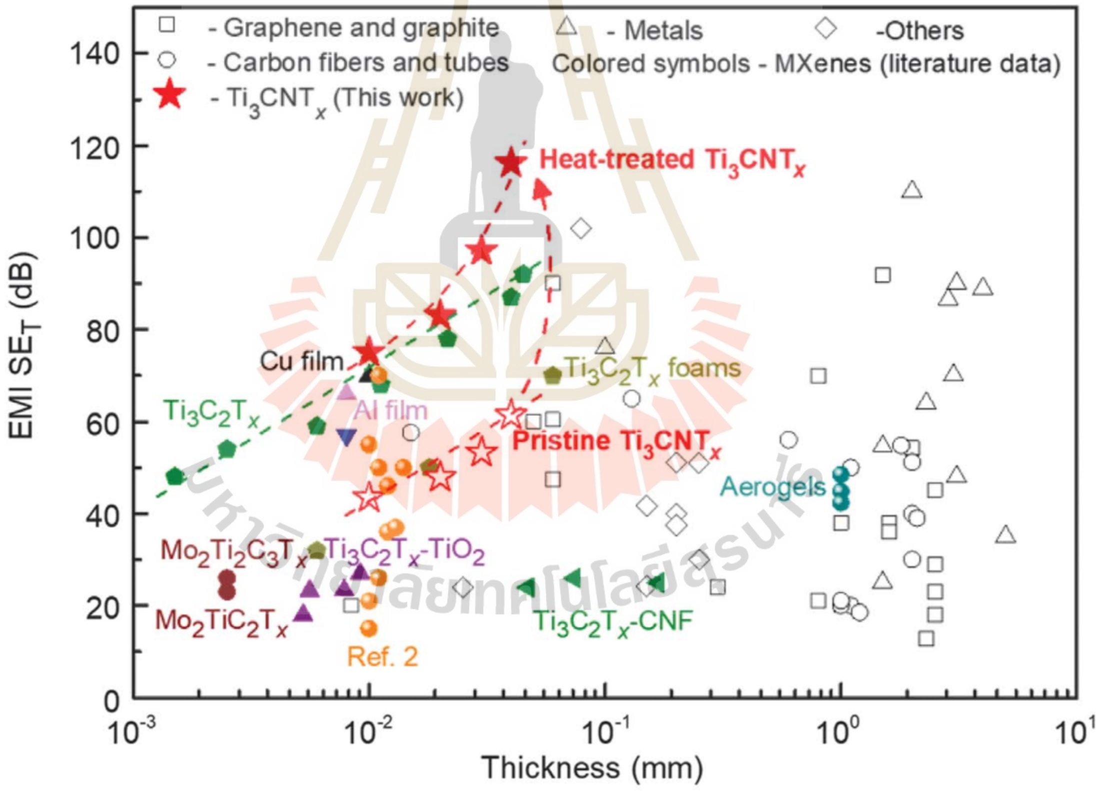

Figure 2.13 The data plot of the EMI SE_T versus thickness of a comparison the EMI SET of annealed films and materials reported in other published works. At comparable thickness, the annealed Ti_3CNT_x MXene shows the highest EMI SE_T than other materials (Iqbal et al., 2020).

2.5.3 Energy storage application of $Ti_3C_2T_x$

$Ti_3C_2T_x$ is the most studied MXene for electrochemical capacitors (supercapacitors). The volumetric capacitance of free-standing $Ti_3C_2T_x$ electrode has been reported to be 300-400 F cm^{-3} which is a higher than the volumetric capacitance of carbon-based electrical double-layer capacitors (EDLC). As shown in figures 2.14(a) and 2.14(b), the $Ti_3C_2T_x$ electrode exhibits the volumetric capacitance exceeding 900 F cm^{-3} in 1 M H_2SO_4 which shows a perfect capacitive behavior for a high charge and discharge rates (Ghidiu et al., 2014).

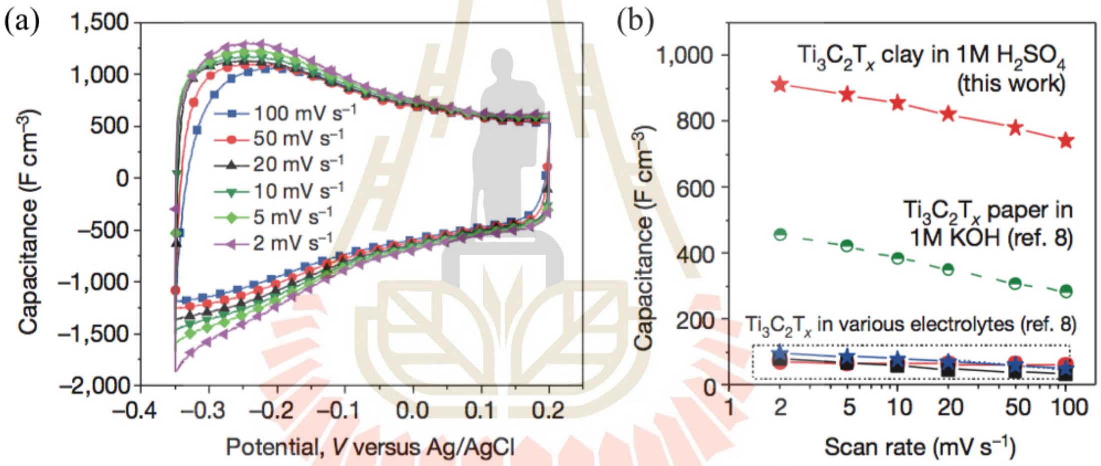

Figure 2.14 (a) CV profiles shown at different scan rates of $Ti_3C_2T_x$ electrode in 1M H_2SO_4. (b) Comparison of electrochemical performances of $Ti_3C_2T_x$ electrode between Ghidiu et al., 2014 and other published works (Ghidiu et al., 2014).

The mechanism of high volumetric capacitance of $Ti_3C_2T_x$ MXene has been studied by using electrochemical *in situ* x-ray absorption spectroscopy (XAS). This study is about the charge storage on pseudocapacitive behavior that associates with the changes in the oxidation state of transition metal. Figure 2.15(a) shows the electrochemical *in situ* XAS measurement of $Ti_3C_2T_x$ electrode in 1M H_2SO_4. The main result of this work is, the titanium oxidation state changes as the oxidation and reduction corresponding with the charging-discharging cycles, respectively (figures 2.15(b)-2.15(d)). The authors concluded that the charge storage mechanism of electrochemical storage in $Ti_3C_2T_x$ MXene in sulfuric acid is predominantly by pseudo-capacitive behavior (Lukatskaya et al., 2015).

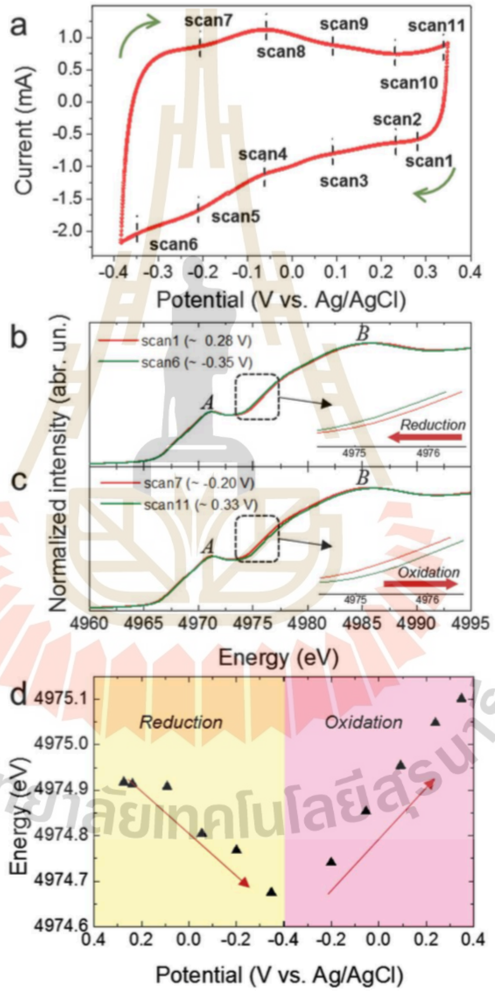

Figure 2.15 (a) CV profiles collected in *in situ* XAS electrochemical cell in 1 M H_2SO_4. Ti K-edge XANES spectra were collected, (b) between 0.28 and -0.35 V and (c) between -0.2 and 0.35 V (vs Ag/AgCl), (d) variation of Ti edge energy vs potential during full potential sweep between -0.35 and 0.35 V (Lukatskaya et al., 2015).

2.5.4 Electromagnetic interference shielding application of $Ti_3C_2T_x$

Zhahzad et al. (Zhahzad et al., 2016) reported a comprehensive study of the EMI shielding performance of $Ti_3C_2T_x$ MXene film which is outperform all of the known synthetic materials; such as graphene, carbon nanotube, and metals (figure 2.16(a)). The main discussion of this work is, the authors proposed the physical mechanism on the EMI shielding of $Ti_3C_2T_x$ MXene that can be explained by several mechanisms. Such mechanisms include: (i) the incident EM wave can be reflected by a highly conducting of MXene surface, (ii) the variety of surface termination groups can help to absorb the EM wave, and (iii) the layered architecture of MXene structure can repeat the mechanisms (i) and (ii), giving rise to multiple internal reflections and more absorption the EM wave in the interlayers MXene, as shown in figure 2.16(b).

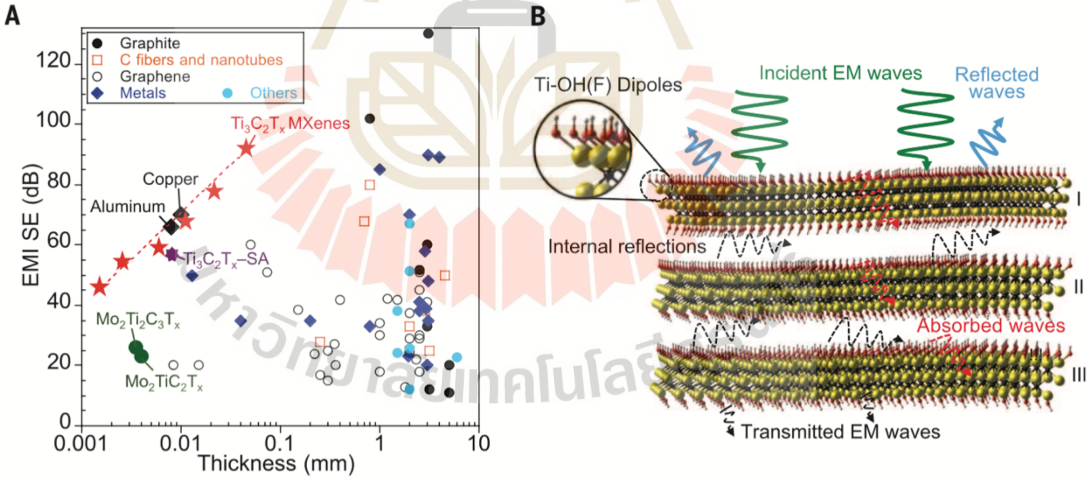

Figure 2.16 (a) Comparison the EMI SE between $Ti_3C_2T_x$ MXene, copper, aluminum, and other MXenes showing that $Ti_3C_2T_x$ lies above these materials. (b) Schematic of the EMI shielding mechanism of $Ti_3C_2T_x$ MXene (Zhahzad et al., 2016).

CHAPTER III

NEGATIVE ELECTRONIC COMPRESSIBILITY

In this chapter, I would like to explain the negative electronic compressibility (NEC) which is related to the discussion on the experimental results of the electronic structures differences between Ti_3CNT_x and $Ti_3C_2T_x$ in this thesis. The theoretical and experimental studies on the NEC will be reviewed in this chapter. The experimental observation of the electronic structure characteristic of NEC by using photoemission spectroscopy (PES) will also be reviewed.

3.1 The theoretical and experimental studies on the negative electronic compressibility (NEC)

The NEC is a measure of the relative change in the electron density and the chemical potential, which is described as $K = (1/n^2)\,(\partial n/\partial \mu)$, where n is the electron density and μ is the chemical potential. NEC is described as the chemical potential counterintuitively become lower upon increasing the electron density. In principle, the NEC is rarely occurred as a counterintuitive effect compared to the positive electronic compressibility (PEC). The PEC is defined as the chemical potential is the higher upon increasing the electron density. Recently, the signature of NEC has been observed in 2D materials and interfaces (Riley et al., 2015; Li et al., 2011), as well as bulk materials (He et al., 2015; Nathabumroong et al., 2020).

The experimental observation on the spectroscopic signature of NEC has been reported by using the advanced spectroscopy, e.g., photoemission spectroscopy (PES). The comprehensive study of the NEC by PES composes of the following steps: (i) varying the electron density in the material with a controllable by the doping; (ii) measuring the change of the chemical potential as a function of electron density; (iii) uncovering and understanding the key mechanism causing to the observed NEC. For the step (i), the general approaches of the electron doping based on PES experiments include surface doping, bulk doping, and photo-doping as a way of varying the electron density in the materials. For the step (ii), measurements the binding energy shifts of the valence band and core-level as the methods for deducing the change of the chemical potential as a function of electron density. In principle, the chemical potential (μ) is defined as the electronic state laid between the valence band maximum (VBM) and the conduction band minimum (CBM) as known as the Fermi level (E_F). For the photoemission experiment, we can determine the chemical potential shift ($\Delta\mu$) by measuring the binding energy shift of energy reference, i.e., deep valance band and core-level relative to the E_F.

Recently, the signature of NEC has been reported in 2D tungsten diselenide (WSe_2) by using angle-resolved photoemission spectroscopy (ARPES) (Riley et al., 2015). This work is focused to study the NEC and tunable spin splitting by using surface doping with *in situ* evaporating alkali metal (rubidium) on the surface. The increased of rubidium deposition results to the increased electron density in the system ($\partial n > 0$). The key finding of this work is, the sub-monolayer deposition of rubidium atoms can donate an extra electron to the WSe_2 surface, resulting to the charge accumulation induced the two-dimensional electron gas (2DEG) (figure 3.1(a)). This surface electron doping affects to the layer degeneracy (ΔL1 and ΔL2), driving the splitting of the valence band minimum (figure 3.1(b)). An observation of the shrinkage of band gap ($\partial\mu < 0$) is the demonstration to the signature of NEC which results from the stronger downward band bending of the conduction band compared to the valance band.

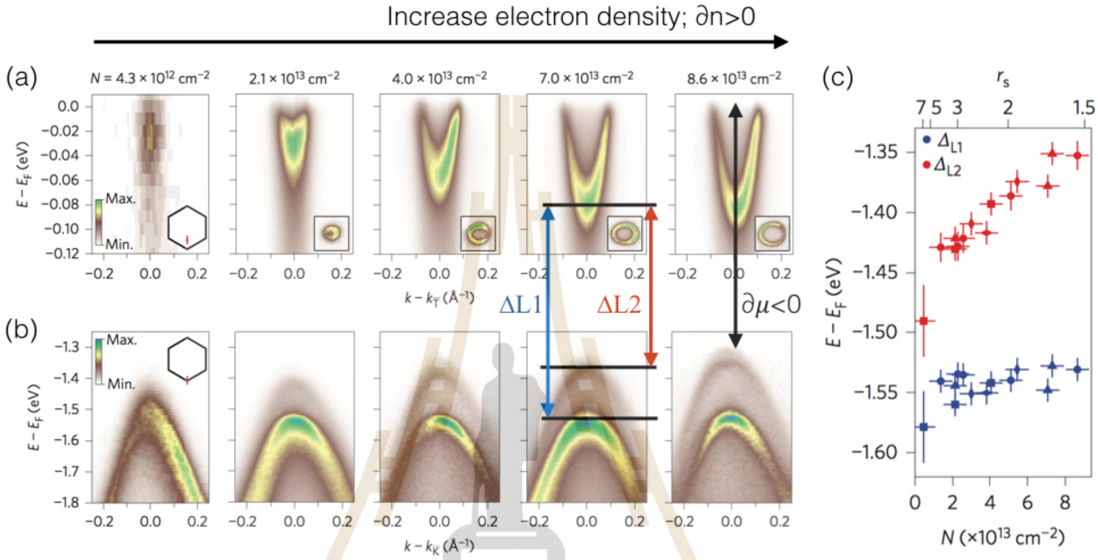

Figure 3.1 (a) ARPES measurements of the dispersion of 2DEG states formed along of **Γ** – K direction. (b) Corresponding the evolution of valence band splitting at K point. (c) Binding energy shift of the valence states indicate a decrease in binding energy with increasing surface-electron density. This figure is adapted from the published work of Riley et al., 2015 (Riley et al., 2015).

The signature of NEC has also been reported in 3D spin-orbit correlated metal ($Sr_3Ir_2O_7$) by using bulk doping based on ARPES measurement (He et al., 2015). This work used the lanthanum (La) substitution in the Sr sites in $Sr_3Ir_2O_7$ structure, leading to a bulk electron doping which is became to $(Sr_{1-x}La_x)_3Ir_2O_7$. As shown in figure 3.2, the increased of doping level x represents to the increased electron density in the system ($\partial n > 0$). The key finding of this work is, by increasing the electron density, the observation of the smaller of band gap ($\partial\mu < 0$) is the demonstration to the signature of NEC which results from the strong spin-orbit interaction in a quasi 3D spin-orbit metal material.

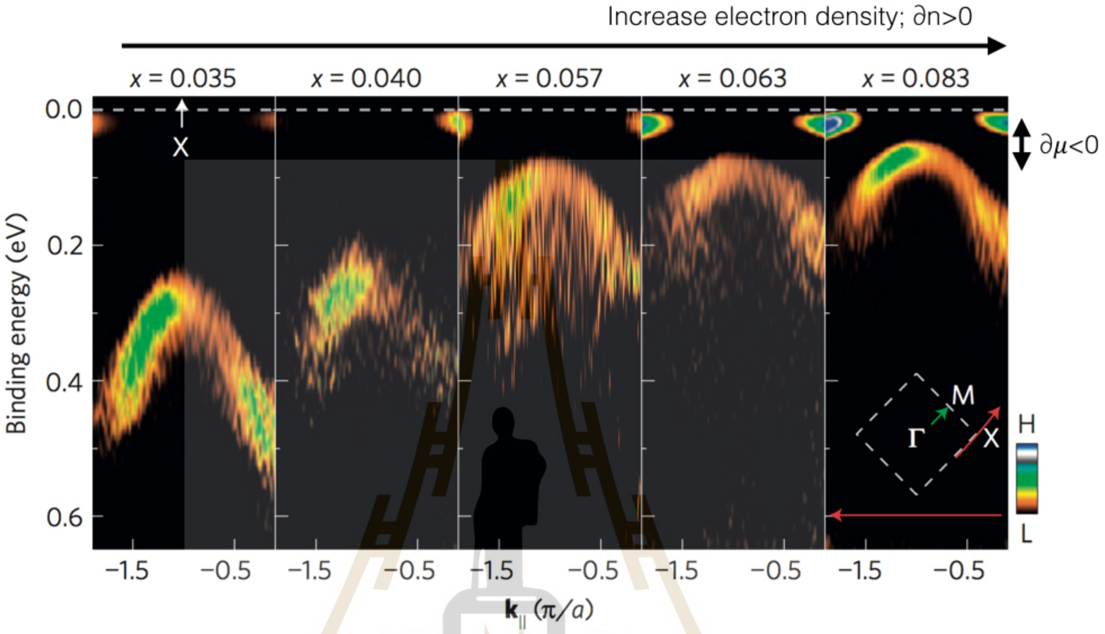

Figure 3.2 Electronic band dispersion of $(Sr_{1-x}La_x)_3Ir_2O_7$ indicating to the evolution of a decrease in binding energy of valence band states upon increasing the doping level x. This figure is adapted from the published work of He et al., 2015 (He et al., 2015).

The signature of NEC has also been studied by using photo-doping based on ultraviolet photoemission spectroscopy (UPS) measurement which is reported in the Bismuth Ferrite ($BiFeO_3$) (Nathabumroong et al., 2020). Figure 3.3(a) shows the oxygen 2p (O 2p) spectra of $Bi_{0.95}La_{0.05}FeO_3$ sample measured under the photo-doping conditions of 0min light irradiation, 5mins ultraviolet (UV) light irradiation, and 5mins zeroth order light irradiation. The signature of NEC is shown by a counterintuitive shift of the O 2p state to a lower binding energies that is initially observed by the first photo-doping condition (5min of UV light exposure), and is clearly observed of approximately 1 eV at the 5mins zeroth order light irradiation (light with all frequencies). In addition, the oxygen vacancy state (V_0) is observed at around 4 eV binding energy after zeroth order light irradiation. The counterintuitive shift to lower binding energy of O 2p state as function of UV light irradiation is found of up to 243 meV at the maximum UV doping of 180 J cm^{-2} (figure 3.3(b)).

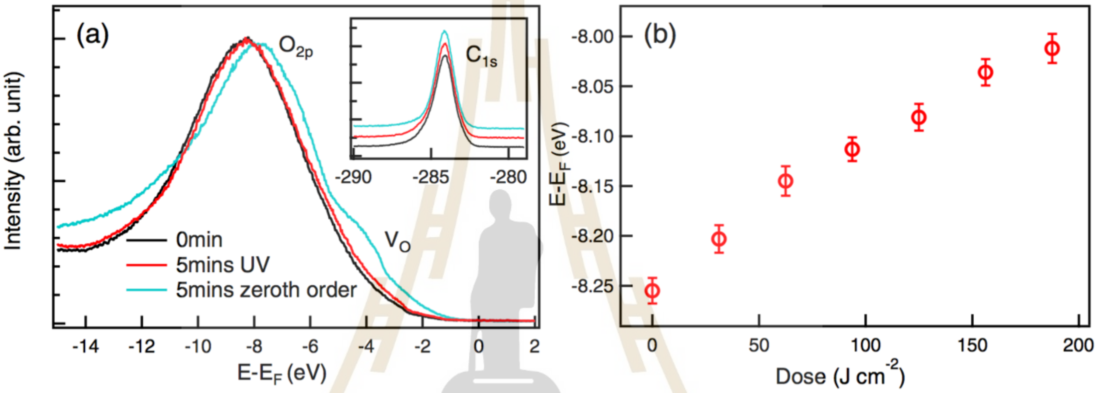

Figure 3.3 (a) Valence band spectra of $Bi_{0.95}La_{0.05}FeO_3$ indicating the shift in binding energy position of O 2p states to lower binding energies at 5mins UV and 5mins zeroth order light irradiation. (b) Summarize the binding energy shift of the O 2p states as a function of light dose (Nathabumroong et al., 2020).

CHAPTER IV

PHOTOEMISSION SPECTROSCOPY

Photoemission spectroscopy (PES) is a powerful tool to directly investigate the electronic structure at the surface of materials which is mostly used to study in the polycrystalline and amorphous-crystalline solid materials. In this chapter, the introduction to photoemission spectroscopy with a general view of photoelectric effect will be reviewed in section 4.1. Next, the simple physical models of photoemission process as called three- and one-step models are presented in section 4.2. Then, the ultraviolet photoemission spectroscopy (UPS) and core-level photoemission spectroscopy will be discussed in sections 4.3, 4.4, and 4.5. The additional related techniques about the potassium evaporation in ultrahigh vacuum and sample preparation are presented in section 4.6.

4.1 Photoelectric effect

Photoemission spectroscopy (PES) is the surface sensitive technique which is used to directly probe the electronic structure at the surface of the materials based on the photoelectric effect. The photoelectric effect was discovered by Hertz in 1887 (Hertz, 1887), and then this effect was explained through the quantum nature of light by Einstein in 1905. By exposing the light with photon energy ($h\nu$) with larger than the work function ($\mathbf{\Phi}$) of material, the electrons are ejected from the surface of the material with the maximum kinetic energy (KE) as called the photoelectron. The KE of photoelectron depends on its binding energy (BE) and Φ. The relationship of these factors can be obtained as the following:

$$\mathrm{BE} = h\nu - \mathrm{KE} - \Phi_A \tag{4.1}$$

where Φ_A is the work function of the analyzer that is larger than the work function of measured sample (Φ). Thus, the Φ_A is usually used as the reference work function relative to the Fermi level (E_F) in the photoemission measurements.

4.2 The photoemission process

In this section, the description of the photoemission process including three-step and one-step models will be described. The photoemission process can be explained as the following: after exposing the light onto the sample surface, photoelectrons are kicked out to the vacuum level as described by the photoelectric effect. Therefore, we can determine the behavior of these photoelectrons by using the equation 4.1.

4.2.1 The three-step model

The three-step model is the most commonly used in the interpretation of the photoemission data. This model is separated into three important steps including the photo-excitation of photoelectron, transport of photoelectron to the surface, and transmission of photoelectron into the vacuum level. The three-step model is displayed in figure 4.1 (left) and is described below.

(I) Photo-excitation of photoelectron

This process explains the situation that an electron at the occupied electronic state (initial state) is excited into the unoccupied state (final state) by the photon and then the electron-hole pair is created inside the crystal.

(II) Transport of photoelectron to the surface

This step can be explained by the terms of inelastic-mean-free-path (IMFP) of photoelectron which is a measurement of how far electrons can travel in the sample surface without inelastic scattering. This term relates with the probability of those photoelectrons to propagate through the surface without losing energy (scattering).

(III) Transmission of photoelectron into the vacuum level

The escape of photoelectron from the sample surface required the photon energy is larger than the energy of work function of the material. This step provides the information of the transmission probability for ejected out of photoelectrons from the surface depending on the excited energy and work function.

4.2.2 The one-step model

The main idea of the one-step model of photoemission process is used to describe the all photoemission process including the photo-excitation, the transport of the photoelectron to the surface, and the escape into the vacuum level as only one step. The one single step can be explained as the following: the excited electron from the initial state is excited go to the damped final state near the surface. This damping final state of electron supports the all photoemission process of photoelectron that travels through the surface of material with a short inelastic mean free path. Unlike the three-step model, the one-step model can cover all of three steps in the three-step model as a single process as shown in figure 4.1 (right).

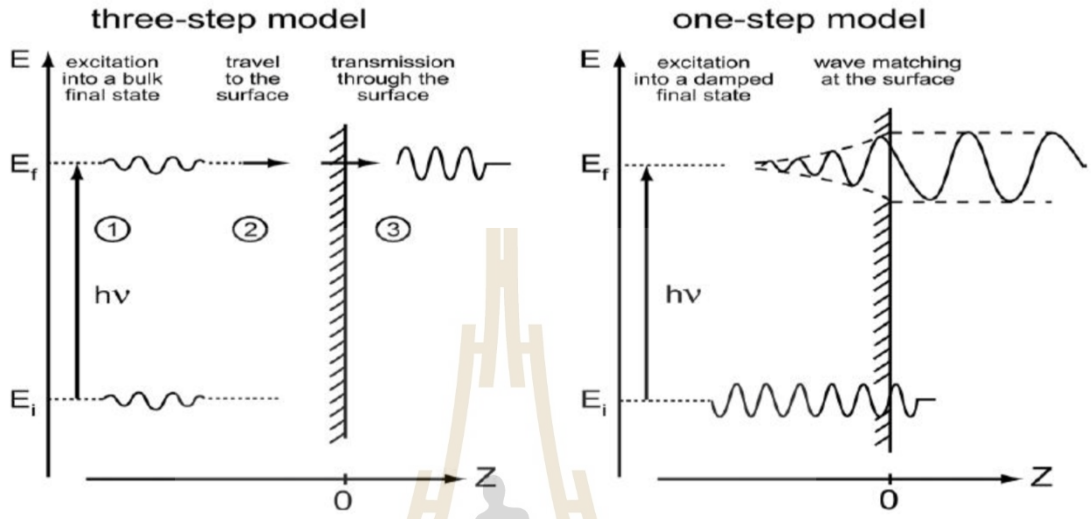
three-step model
E
excitation into a bulk final state
travel to the surface
transmission through the surface
E_f
①
②
③
hν
E_i
Z
0
one-step model
E
excitation into a damped final state
wave matching at the surface
E_f
hν
E_i
Z
0

Figure 4.1 Schematic illustration of the three-step model (left) and one-step model (right) for interpretation the possibility of photoemission process (Hüfner, 1995).

4.3 Ultraviolet photoemission spectroscopy (UPS)

This section is dedicated for a brief introduction to the advantage of UPS. For this, the light source of monochromatic photons and the synchrotron light with ultraviolet irradiation range are applied to eject the electrons from the sample surface to examine the valence levels and outermost electrons of core-levels. Traditionally, the He lamp with $h\nu$ = 21.1 eV is typically used to be the light source for UPS experiment. Nowadays, the synchrotron light source with tunable photon energy has become available to be a modern UPS experiment for investigating the electronic structure of materials. Due to a short length of the inelastic mean free path (IMFP), UPS is the surface sensitive technique (see the information of IMFP in figure 4.2).

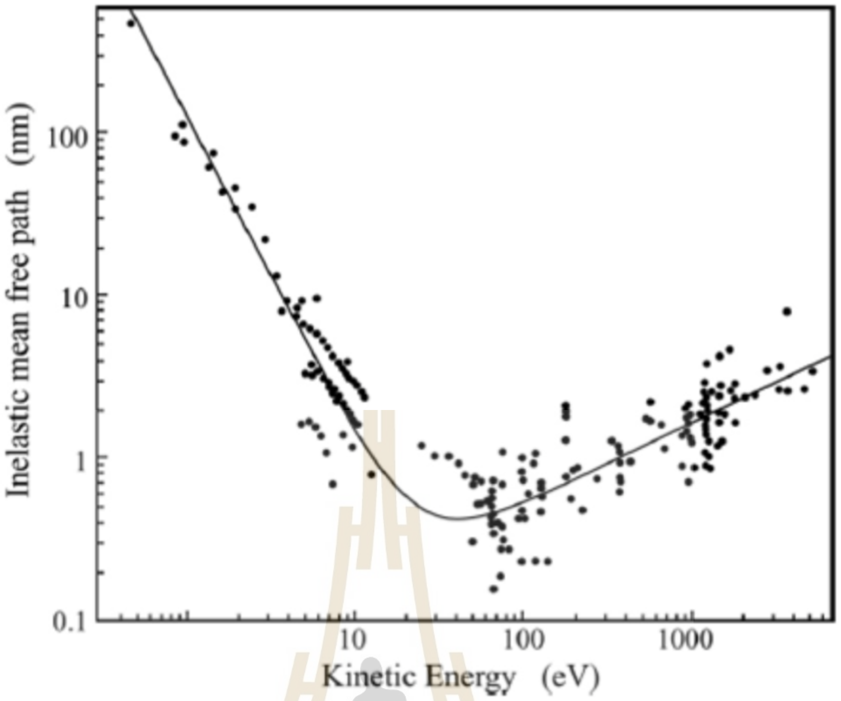

Figure 4.2 The universal curve of inelastic mean free path (IMFP) of electron in solids as a function of kinetic energy. This figure is adapted from the published work of Seah and Dench, 1979 (Seah and Dench, 1979).

4.4 UPS measurements system

The schematic of a typical photoemission experiment and the real apparatus of photoemission end-station of the beamline 4.0.3 (MERLIN) of the Advanced Light Source (ALS), USA, are shown in figures 4.3(a) and 4.3(b), respectively. Synchrotron light source contains a wide spectral range of high intensity and continuous spectrum which commonly used for modern photoemission measurement. In UPS experiment, the synchrotron radiation with energy of UV range is used to be a light source over a broad range of photon energies $h\nu \approx$ 40-100 eV. Nowadays, the beam size can be focused down to about 100 μm, and its direction of incidence angle onto the sample can be precisely controlled.

The synchrotron light is the electromagnetic radiation which is produced by bending magnet holding electrons inside the storage ring. The electrons are generated in the storage ring and are accelerated to be near the speed of light by the linear accelerator. The electrons are circulated around the storage ring by bending magnet which deflected through the magnetic field created by the magnets that give off the electromagnetic radiation, and consequently the beam of synchrotron light is produced. In order to enhance the photon flux of emitted light, many insertion devices such as multipole wigglers or undulators are installed alongside the storage ring which can be seen in the new generation of the synchrotron light source around the world. Note that the main of UPS data in this thesis were carried out at beamline 4.0.3 (MERLIN) of the Advanced Light Source (ALS), USA.

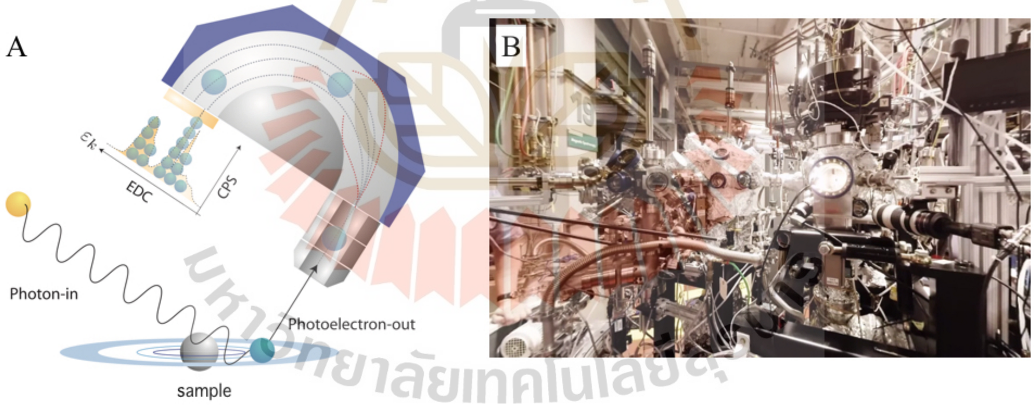

Figure 4.3 (a) Schematic illustration of UPS system, consisting of incident photon light, sample, and electron analyzer. (b) Real equipment of high energy resolution UPS beamline at the Advanced Light Source (ALS), USA.

The electron analyzer is a main equipment for UPS experiment consisting of an electrostatic lens, hemispherical deflector, entrance slit, exit slit, and electron detector. It is used for detecting the number of photoelectrons, which defines the energy of the analyzed photoelectrons. The hemispherical electron analyzer is traditionally used for photoemission measurement in the past. In order to understand the mechanism of electron collection, the traditional hemispherical analyzer is firstly discussed. The photoelectrons excited from the surface of solid sample are detected and retarded by electrostatic lens to the entrance slit. This allows some photoelectrons with right kinetic energies which can be explained by the pass energy equation as the following:

$$E_{pass} = \frac{e\Delta V}{\frac{R_2}{R_1} - \frac{R_1}{R_2}} \tag{4.2}$$

where the ΔV is a potential difference, R_1 and R_2 are radius of two hemispheres. These electrons that satisfy this equation can reach to the exit slit and electron detector. The energy resolution of measured electron can be calculated by

$$\Delta E_\alpha = E_{pass}\left(\frac{d_w}{R_0} + \frac{\alpha^2}{4}\right) \tag{4.3}$$

where d_w is the width of entrance slit, $R_0 = \frac{R_1 + R_2}{2}$, and α is acceptance angle. The photoemission spectrum is recorded as a function of kinetic energy by scanning the electrostatic lens.

In the present, our UPS measurements system use new state-of-the-art of electron analyzer with 2D detector. The energy distribution curves (EDCs) are obtained simultaneously with a wide angular range, which is the advantageous for faster measurement time and acquires better quality of the spectrum. The 2D analyzer comprises of two-micro-channel plates, phosphor plates, and charge coupled device (CCD) camera. The photoelectrons travel through the 2D analyzer are recorded simultaneously as a function of KE and θ. The 2D data contains the set of KE, θ, and photoelectrons intensity. In this thesis, we have utilized this analyzer to measure the UPS spectrum of Ti_3CNT_x and $Ti_3C_2T_x$ MXene samples as typically called angle-integrated photoemission spectrum which allows to use an energy resolution of 50 meV. Note that, the measurement setup is set the reference energy, i.e., the Fermi level of gold sample to be the same with that of spectrometer by doing the electrical contact between the gold sample and spectrometer.

The UPS spectrum contains the information of the distribution of electrons from the valence band and outermost core-level of the materials, that reported the number of photoelectrons as a function of binding energy (BE or E_B) (figure 4.4). The main features of UPS spectrum are associated with BE defining with the separation between the lower binding energy at the E_F as called the valence band, and the higher binding energy called the core-level as shown in figure 4.5. The peaks below the E_F are derived from weakly bound electrons states that formed the valence band. The peaks at higher binding energy represents the core-level, which refer to a characteristic of its binding energy of each element. The core-level peak can be used to identify the elements with respect to the surface chemistry of measured material.

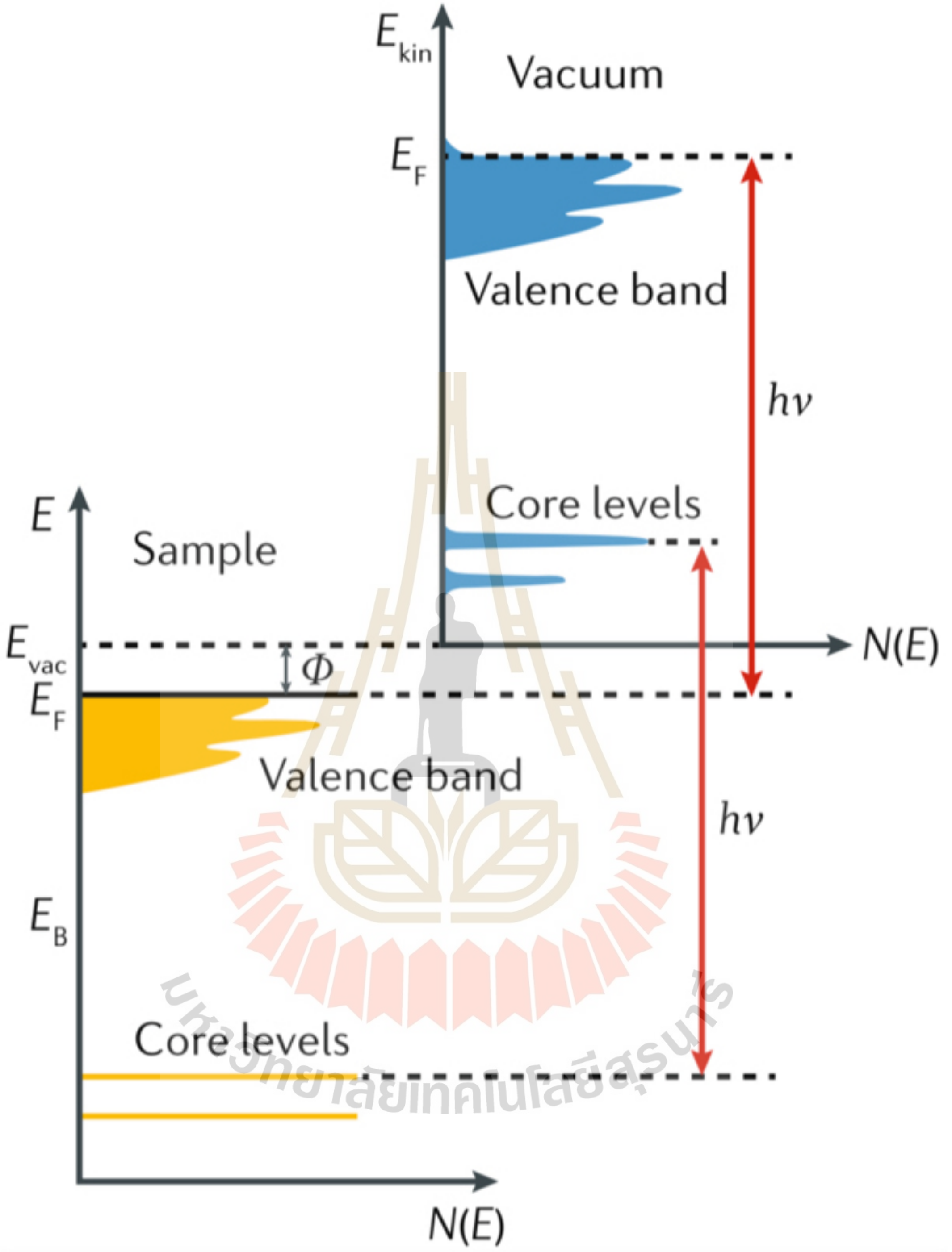
E_{kin}
Vacuum
E_F
Valence band
$h\nu$
Core levels
N(E)
E
Sample
E_{vac}
Φ
E_F
Valence band
$h\nu$
E_B
Core levels
N(E)

Figure 4.4 Relationship between the electronic structure of a solid system (bottom-left) and its photoemission spectrum (top-right). Electrons with binding energy (BE) can be excited to above the vacuum level (E_{vac}) by photons with energy $h\nu$ > BE + $\mathbf{\Phi}$ (Lv et al., 2019).

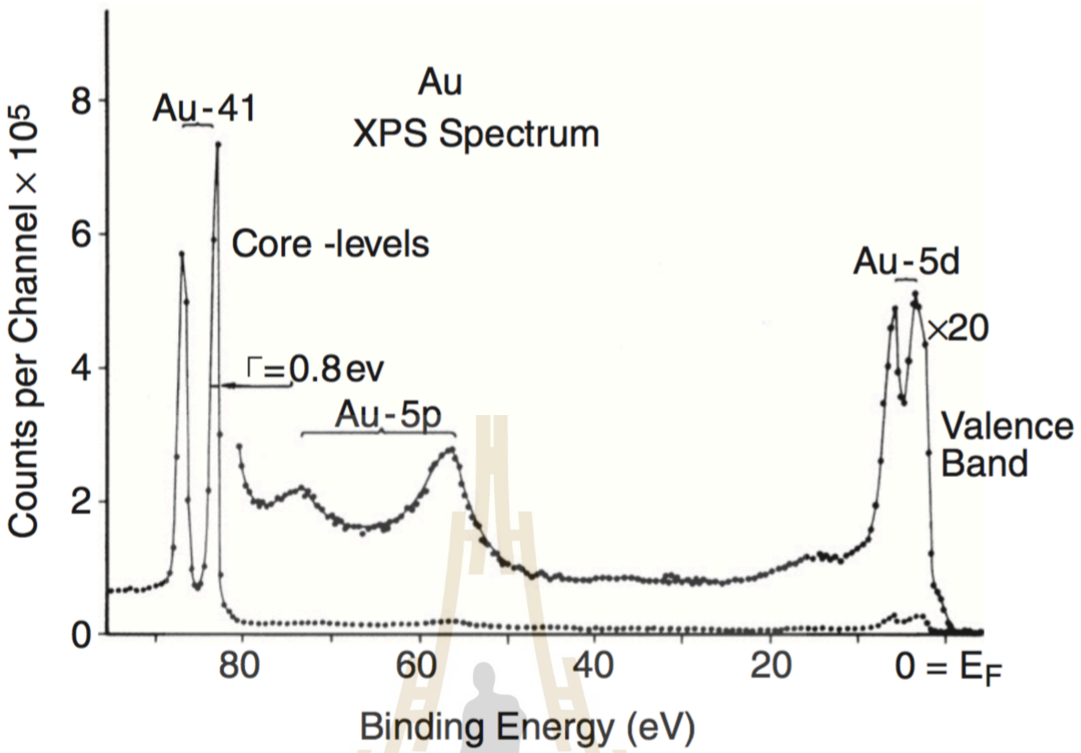

Figure 4.5 UPS spectrum of poly-crystalline Au sample shown as a function of binding energy for 0 (Fermi level, E_F) to 100 eV. The valence band, Au 5d, and Au 5p core-level are observed. This figure is adapted from the published work of Reinert and Hüfner, 2005 (Reinert and Hüfner, 2005).

4.5 Core-level photoemission spectroscopy

Core-level photoemission spectroscopy involves to the study of the deeper electron levels. It is a powerful approach to study the chemical shift, chemical composition, and determine the chemical state of elements on the material surfaces. UPS and soft x-ray photoemission spectroscopy (XPS) are a base technique to investigate the chemical shifts and chemical compositions on the sample surfaces by irradiating UV and soft x-ray light to the surface of sample. The photoelectrons are ejected out from the sample surfaces and will be collected as the photoemission spectrum in a function of kinetic energies. The photoemission spectrum will be some feature of a small shifts in binding energies as called ‘chemical shift’ which determines the information of the chemical state of atoms. Since each element has a characteristic of its binding energies, the peak positions can be used to identify the elements with respect to the surface of measured materials. The concentration of element can be determined by integrating peak intensities under the area of the photoemission peaks as subtracted with the Shirley background, which is used to be a normalization to compare the concentration in each element.

4.6 Related techniques

4.6.1 Potassium evaporation in ultrahigh vacuum

Potassium is the one of chemical element of group IA in the periodic table which is well-known as very reactive element with good electron donor in UPS experiment. In this work, the high purity of potassium source (SAES-dispenser) is set in ultrahigh vacuum chamber to avoid the air contamination. To evaporate the potassium, we clean the potassium source by increasing the current to be around 3-4 A, for a few minutes to repel some contaminations from the source (degassing). Next, the MXene samples are moved to confront with the potassium dispenser. We then apply the potassium evaporation onto the sample surfaces by increasing the current more than 5 A, which is the exact calibration value to heat the potassium dispenser above the boiling point of potassium. After the current is more than the potassium boiling point, the pressure will enhance drastically in this process. This is an evidence confirming that potassium source has already activated inside the chamber and evaporated out of the dispenser to the sample surfaces.

4.6.2 Preparation of Ti_3CNT_x and $Ti_3C_2T_x$ for UPS measurement

Ti_3CNT_x and $Ti_3C_2T_x$ MXene samples (from Prof. Dr. Yury Gogotsi and Dr. Kanit Hantanasirisakul) were produced by selective etching of Al element from their Ti_3AlCN and Ti_3AlC_2 MAX phases powder in a mixture of LiF and HCl solution. The free-standing films of Ti_3CNT_x and $Ti_3C_2T_x$ MXenes with a thickness of 5 μm were produced via vacuum-assisted filtration method. To prepare the Ti_3CNT_x and $Ti_3C_2T_x$ samples for UPS measurement, we mounted the Ti_3CNT_x and $Ti_3C_2T_x$ samples on the copper plates and ground them by using silver epoxy in order to enhance the electrically conductivity and vacuum compatible. Then, the Ti_3CNT_x and $Ti_3C_2T_x$ samples are marked and pinned with ceramic top-post for cleaving the surface in ultrahigh vacuum (UHV). After the Ti_3CNT_x and $Ti_3C_2T_x$ samples are cleaved, the UPS experiments can be performed before and after potassium evaporation.

CHAPTER V

SPECTROSCOPIC SIGNATURE OF NEGATIVE ELECTRONIC COMPRESSIBILITY FROM THE TI CORE-LEVEL OF TITANIUM CARBONITRIDE MXENE

This chapter presents the systematically study on the electronic structure differences between Ti_3CNT_x and $Ti_3C_2T_x$ by UPS experiment and DFT calculations. The contents in this chapter are from my published research article on the observation of the spectroscopic signature of the NEC at the Ti 3p core-level in Ti_3CNT_x MXene (Jindata et al., 2021). In this chapter, I will introduce the new approach to study the electronic structure differences between Ti_3CNT_x and $Ti_3C_2T_x$. The way of how to study this difference will be performed through a combination of UPS measurements during electron doping (*in situ* K deposition) and DFT calculations. The DFT calculations include the Ti 3p core-level and valence band shifts calculation, the DOS calculation, as well as the charge density difference and the Bader charge calculation. This chapter has been divided into two main parts, i.e., UPS experiments and DFT calculations. I made a major contribution in the UPS measurements and data analysis. The Ti_3CNT_x and $Ti_3C_2T_x$ samples were synthesized and characterized by Dr. Kanit Hantanasirisakul. All of the DFT calculations were done by Dr. Ittipon Fongkaew.

5.1 Introduction

MXenes are a very large class of 2D materials with a general formula of $M_{n+1}X_nT_x$, where M is an early transition metal, X represents C and/or N, T_x stands for surface terminations; for example, −O, −OH, −F, and –Cl, and $n = 1-4$ (Naguib et al., 2011; Gogotsi et al., 2019; Anasori et al., 2019). Titanium carbide, $Ti_3C_2T_x$, is the first discovered and the most studied MXene to date. It possesses the layered structure with unique intrinsic properties, such as high electrical conductivity exceeding 10 000 S/cm (Zhang et al., 2017), high negative surface charge in solution (Ying et al., 2015) and a variety of surface terminations (Persson et al., 2018), which renders it promising for a wide variety of applications spanning through energy storage, electronics, optics, electromagnetic interference (EMI) shielding and sensors (Anasori et al., 2017; Khazaei et al., 2013; Hantanasirisakul et al., 2018; Shahzad et al., 2016; Ma et al., 2017). Titanium carbonitride (Ti_3CNT_x) is isostructural with $Ti_3C_2T_x$ with ~50% of the carbon atoms in the X layers substituted by nitrogen atoms. It has been previously thought that nitrogen doping into the X layer will result in higher electrical conductivity, as observed in bulk carbonitrides (Gogotsi et al., 1999). However, the electrical conductivity of Ti_3CNT_x has been reported to be about an order of magnitude lower than that $Ti_3C_2T_x$ (Du et al., 2017; Hantanasirisakul et al., 2019). However, recent experimental studies reveal some exceptional properties of Ti_3CNT_x such as anomalously high EMI shielding effectiveness (Iqbal et al., 2020), superior charge storage capacity (Du et al., 2017; Lu et al., 2020), and very high negative surface charge (Naguib et al., 2015) compared to $Ti_3C_2T_x$. The role of nitrogen atoms in the MXene structure and their effects on electronic and other properties remain to be further understood.

Understanding and controlling MXene electronic structure is important to further tune and improve the material performance. Photoemission spectroscopy (PES) and density functional theory (DFT) calculations are powerful tools for this purpose. A comparison of measured photoemission spectra with calculated density of states (DOS) of materials provides insights into interactions between electrons in the system. Recently, PES has been used to distinguish the difference of the chemical composition and chemical bonding on $Ti_3C_2T_x$ surface (Halim et al., 2016; Schultz et al., 2019; Enyashin et al., 2013).

DFT calculations have revealed drastic difference of the electronic structure between $Ti_3C_2T_x$ and Ti_3CNT_x MXenes, despite their very similar structure (Lu et al., 2020; Enyashin et al., 2013; Sun et al., 2020). For example, Ti_3CNT_x has the hybridization of additional Ti-N bonding that contributes to DOS near the E_F. Moreover, a significant effect of nitrogen bonding in Ti_3CNT_x on the charge storage capability has been predicted by DFT calculations (Zhang et al., 2016). However, the difference between the electronic structures of Ti_3CNT_x and $Ti_3C_2T_x$, which is essential for fundamental understanding of the electronic properties of these MXenes, remain unexplored experimentally.

New approaches, such as surface electron doping achieved by alkali-metal deposition, may help to study and better understand the electronic structure of MXenes. It is a powerful method for studying the electron-electron interactions in various 2D materials, which show the variation of electronic structure as a function of electron density (n) (Chen et al., 2018; Kim et al., 2017; Kang et al., 2017; Eknapakul et al., 2018). In particular, the so called negative electronic compressibility (NEC) has been observed when electrons are doped into 2D materials (Riley et al., 2015). The negative thermodynamic density of states, which is described as a counterintuitive decrease of chemical potential (μ) upon increasing the electron density $(1/n^2)$ $(\partial n/\partial \mu) < 0$ (Eisenstein et al., 1992; Eisenstein et al., 1994), can be experimentally observed by using PES measurements (Riley et al., 2015; He et al., 2015; Wen et al., 2020).

Here, we used a combination of *in situ* ultraviolet photoemission spectroscopy (UPS) measurements during electron doping and DFT calculations to provide further insights into fundamentally different electronic structures of Ti_3CNT_x and $Ti_3C_2T_x$ MXenes. We report on the spectroscopic signature of NEC in Ti_3CNT_x as it shows a chemical potential shift to lower binding energies of the Ti 3p core-level up to ~250 meV upon electron doping, indicating a decrease of the chemical potential with increasing electron density, which is not observed in $Ti_3C_2T_x$. Our DFT calculations demonstrate that the spectroscopic signature of NEC resulted from the hybridization of titanium-nitrogen bonding in Ti_3CNT_x which plays an important role in promoting the Ti 3d available states for receiving more electron above the E_F upon electron doping. These results not only clearly show a significant difference in the electronic structures of Ti_3CNT_x and $Ti_3C_2T_x$, but also provide a new strategy to further study the electronic properties of MXenes.

5.2 Experimental and calculation approaches

The Ti_3CNT_x and $Ti_3C_2T_x$ samples were produced by selective etching of Al element from their Ti_3AlCN and Ti_3AlC_2 MAX phases in a mixture of LiF and HCl solution as described by Hantanasirisakul et al., 2019 and Alhabeb et al., 2017.

The free-standing films of MXenes with a thickness around 5 μm were produced via vacuum-assisted filtration of the delaminated MXene solutions. Their electronic structures were measured by using high-resolution UPS, performed at the MERLIN beamline 4.0.3 of the Advanced Light Source (ALS), U.S.A., using photon energy of 90 eV and a Scienta R4000 hemispherical electron analyzer. The measurements were performed immediately after cleaving the surface in ultrahigh vacuum at a pressure better than 4×10^{-11} Torr, as well as, following the deposition of potassium (K) onto the sample surface from a properly outgassed of alkali metal dispenser (SAES Getters). Density functional theory (DFT) calculations were carried out using the Vienna Ab-Initio Simulation Package (VASP) code. The computational method based on DFT was used in the generalized gradient approximation (GGA). The structural relaxations were performed with the Perdew-Burke-Ernzerhof (PBE) parameterization (Perdew et al., 1996; Perdew et al., 1997) exchange-correlation functional and projector augmented wave (PAW) pseudopotentials (Blöchl et al., 1994), with van der Waals corrections and Tkatchenko-Scheffler method iterative Hirshfeld partitioning (Kerber et al., 2008). A 11 × 11 × 11 and 5 × 5 × 1 Monkhorst-Pack *k*-point grids were used for bulk and for supercell calculations, respectively. The electron wave functions were described using a plane wave basis set with the energy cutoff of 520 eV.

5.3 The experimental results

5.3.1 Characterization of Ti_3CNT_x and $Ti_3C_2T_x$ by XPS

Figure 5.1 shows the quintuple layers of Ti_3CNT_x packed in a hexagonal structure of the three M-layers of titanium atoms interleaved by two X-layers of the nitrogen atoms alternately substituting carbon atoms (Jhon et al., 2017), with optimized lattice constants of $a = 3.01$ Å and $c = 18.70$ Å. The chemical compositions of Ti_3CNT_x and $Ti_3C_2T_x$ samples were characterized by XPS. A survey scan, Ti 2p, C 1s and N 1s core-level spectra of Ti_3CNT_x are shown in figures 5.2(a)-5.2(d), respectively. The survey scan is assigned to the Ti 3p, Cl 2p, C 1s, N 1s, Ti 2p, O 1s, and F 1s core-level. For the Ti 2p core-level, four pairs of doublets correspond to spin-orbit splitting of the Ti $2p_{1/2}$ and Ti $2p_{3/2}$ were fitted and assigned to Ti-C-N (461.18 eV and 454.98 eV), Ti-O (461.27 eV and 455.77 eV), Ti-F (462.74 eV and 457.04 eV), and TiO_2 (464.36 eV and 458.76 eV) bonds, respectively. The C 1s core-level can be deconvoluted into four fitted peaks: $C-Ti-T_x$ (281.88 eV), C−C (284.95 eV), C−O (286.55 eV) and O−C=O (288.83 eV). The chemical bonding of carbon atoms with highly electronegative oxygen atoms affect the chemical shifts of O−C=O peak appeared at the higher binding energy followed by C−O, C−C and $C-Ti-T_x$ peaks, respectively. For the N 1s core-level, three peaks were used to fit the spectrum: $N-Ti-T_x$ (396.67 eV), N−O−Ti (399.34 eV) and $N-TiO_x$ (401.65 eV). Also, the chemical bonding of nitrogen atoms with highly electronegative oxygen atoms affect the chemical shifts of $N-TiO_x$ peak appeared at the higher binding energy followed by N−O−Ti and $N-Ti-T_x$ peaks, respectively.

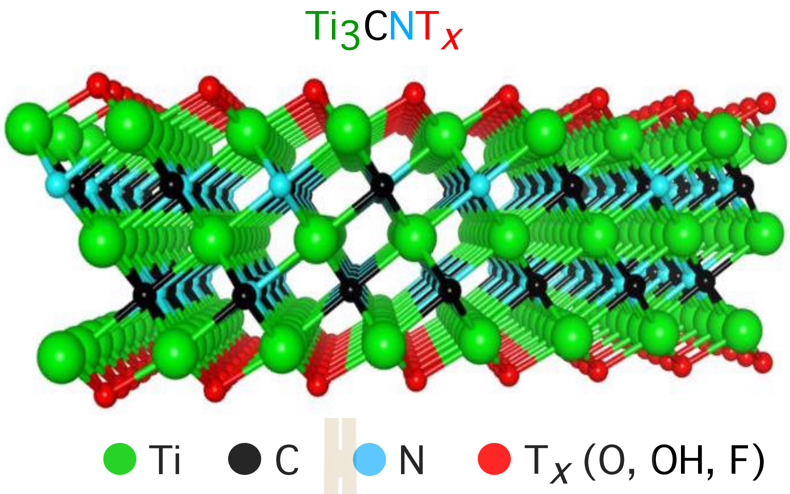

Figure 5.1 Atomic structure of Ti_3CNT_x, composed of stacking three Ti layers interleaved with two alternately mixed C and N layers, as well as terminated by surface terminations (T_x) layers (adapted from (Jindata et al., 2021)).

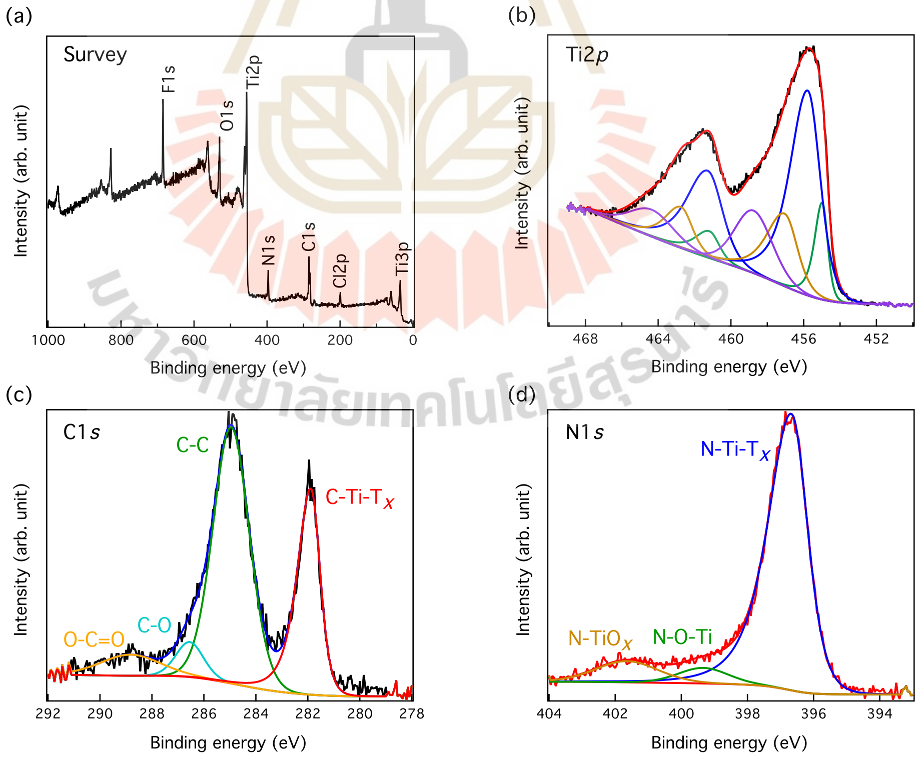

Figure 5.2 X-ray photoelectron spectra of Ti_3CNT_x MXene. (a) Survey scan assigned to the peak Ti 3p, Cl 2p, C 1s, N 1s, Ti 2p, O 1s, and F 1s core- level spectra. (b) The

Ti 2p core-level fitted by the four pairs of doublets correspond to spin-orbit splitting of the Ti $2p_{1/2}$ and Ti $2p_{3/2}$. (c)-(d) The C 1s and N 1s core-level XPS spectra of Ti_3CNT_x, respectively. For the C 1s core-level, the four fitting peaks are assigned to C−Ti−T_x, C−C, C−O and O−C=O bonds and for the N 1s core-level, the three fitting peaks are assigned to N−Ti−T_x, N−O−Ti, and N−TiO_x bonds (adapted from (Jindata et al., 2021)).

Figure 5.3(a) shows the atomic structure of $Ti_3C_2T_x$ sample which the two carbon layers are sandwiched by the three titanium layers with optimized lattice constant a = 3.30 Å and c = 17.75 Å. The sample characterization has been studied by XPS. The survey scan of $Ti_3C_2T_x$ is shown in figure 5.3(b) which is assigned to the Ti 3p, Cl 2p, C 1s, Ti 2p, O 1s, and F 1s core-level. Figure 5.3(c) presents the Ti 2p core-level with the four pairs of doublets correspond to spin-orbit splitting of the Ti $2p_{1/2}$ and Ti $2p_{3/2}$ were fitted and assigned to Ti-C (461.02 eV and 454.82 eV), Ti-O (461.13 eV and 455.63 eV), Ti-F (462.79 eV and 457.09 eV), and TiO_2 (464.17 eV and 458.09 eV) bonds, respectively. For the C 1s core-level, the four fitting peaks are shown in figure 5.3(d) which assigned to C-Ti-T_x (282.05 eV), C-C (284.94 eV), C-O/C-H (285.8 eV), and COOH (287.71 eV), respectively.

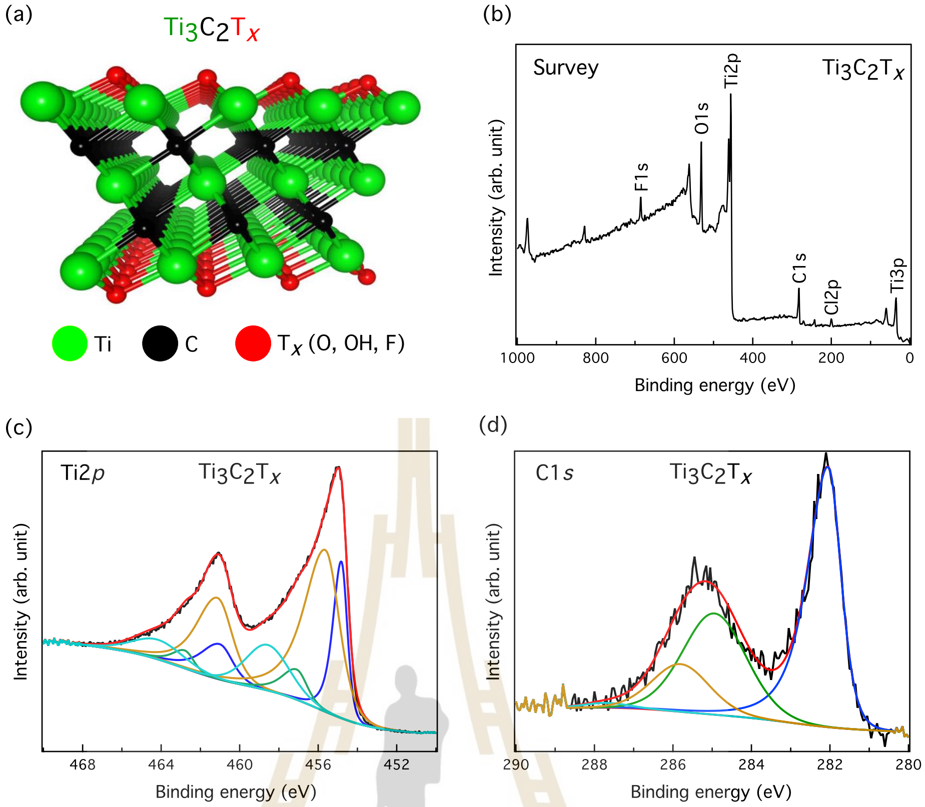

Figure 5.3 (a) Atomic structure, (b) survey scan and high-resolution (c) Ti 2p and (d) C 1s core- level spectra of $Ti_3C_2T_x$. The peaks in the survey scan are assigned to Ti 3p, Cl 2p, C 1s, Ti 2p, O 1s, and F 1s core-level spectra. For the Ti 2p, four pairs doublets correspond to spin-orbit splitting of the Ti $2p_{1/2}$ and Ti $2p_{3/2}$ are fitted (Jindata et al., 2021).

5.3.2 Analysis of the photoemission data

5.3.2.1 Determining the potassium concentrations by Ti 3p and K 3p core-level spectra

All angle-integrated photoemission spectra were measured on freshly-cleaved Ti_3CNT_x and $Ti_3C_2T_x$ surfaces. We used *in situ* potassium (K) deposition for electron doping. K is a well-known electron donor used during PES experiments (Shi et al., 2017). In this study, the electron density was increased by increasing the K deposition times at a constant current $I = 5$ A. Figures 5.4(a) and 5.4(b) show the K 3p core-level spectra as function of deposition time for Ti_3CNT_x and $Ti_3C_2T_x$ samples, respectively. The K concentrations were estimated by comparing the relative core-level peak intensities of the Ti 3p and K 3p using the simulation of electron spectra for surface analysis (SESSA) XPS simulation program (Nemšák et al., 2014; Smekal et al., 2005; Werner et al., 2013). We initially evaluated the relative ratio of Ti to K at each deposition time by integrating peak intensities under the areas of the Ti 3p and K 3p with normalization from the PES cross-section (Nilson et al., 2012). The integrated peak intensities under the areas of the Ti 3p and K 3p core-level spectra were performed based on the quantitative XPS analysis. The peak area (I_i) of the peak i is expressed by the following:

$$I_i = N\sigma_i\lambda_i K \tag{5.1}$$

where, N is the number of atoms per area, σ_i is the photoelectron cross-section, λ_i is the inelastic mean free path of the photoelectron, and K is the all other factors related to the quantitative detection of a signal. Here, we assume that the λ factor is negligible and the K factor is constant during the experiment. In order to show the spectral change by potassium deposition, the change in the integrated intensities under the areas of Ti 3p (green color) and K 3p (blue color) core-level spectra are plotted as a function of deposition time for Ti_3CNT_x (figure 5.5(a) and $Ti_3C_2T_x$ figure 5.5(c)), respectively. It is shown that the Ti 3p is rather not changed with increasing the deposition time, while the K 3p is increased in both MXene samples. Thus, we have evaluated the relative ratio of Ti to K with normalization from the photoelectron cross-section. As a result, the relative ratio is monotonically increased (see figures 5.5(b) and 5.5(d) for Ti_3CNT_x and $Ti_3C_2T_x$, respectively). This leads to the hypothesis that the potassium concentrations are increased on the surface of the two MXene samples. After that, the concentrations of K dopant were estimated by varying the relative intensities of the Ti 3p and K 3p in Ti_3CNO_2 and $Ti_3C_2O_2$ models in the Simulation of Electron Spectra for Surface Analysis (SESSA) XPS simulation program in order to give the best agreement in the relative ratio of Ti to K between simulations and experimental measurements of Ti_3CNT_x and $Ti_3C_2T_x$.

Next, the concentrations of K dopant were estimated by varying the relative intensities of the Ti 3p and K 3p in the SESSA XPS simulation program to give the best agreement in the relative ratio of Ti to K between simulations and experimental measurements of Ti_3CNT_x and $Ti_3C_2T_x$, as summarized in tables 5.1 and 5.2, respectively. This resulted in the K concentrations per MXene formula of 0.10, 0.23, 0.35, 0.51 K atoms in the Ti_3CNT_x unit cell and 0.07, 0.18, 0.29, 0.41 K atoms in the $Ti_3C_2T_x$ unit cell for –2, –5, –10, and –20 min doping times, respectively. In this work, we used this estimated K concentrations to represent the electron density in the system. By assuming that K atoms only donate their 4s electrons to the MXene surface, the doped electron densities of Ti_3CNT_x and $Ti_3C_2T_x$ range from $0.10e$ to $0.51e$ and $0.07e$ to $0.41e$ per unit cell, respectively (see figures. 5.6 and 5.7 for Ti_3CNT_x and $Ti_3C_2T_x$, respectively). Fitting the K 3p spectra with a Gaussian function reveals no potassium metal intercalation, as the peak would appear at a lower binding energy, indicating only the surface adsorption of the potassium atoms on MXene surfaces (Rossnagel et al., 2010). In addition, the absence of spin-orbit splitting feature in K 3p peak was attributed to the fact that the surface coverage of potassium is less than one monolayer (Riffe et al., 1990). The larger chemical shift toward higher binding energies of K 3p core-level of both Ti_3CNT_x (~510 meV) and $Ti_3C_2T_x$ (~240 meV) as shown in figures 5.4(a) and 5.4(b), can be attributed to the formation of potassium oxide on the MXene surface by the chemical bonding between potassium and oxygen surface termination of MXene. Similar shift to a higher binding energy of up to 600 meV of K 3p and K 2p core-level of potassium oxide on aluminum, silicon and copper surfaces have been reported (Braaten et al., 1991; Krix et al., 2013; Waluyo et al., 2019).

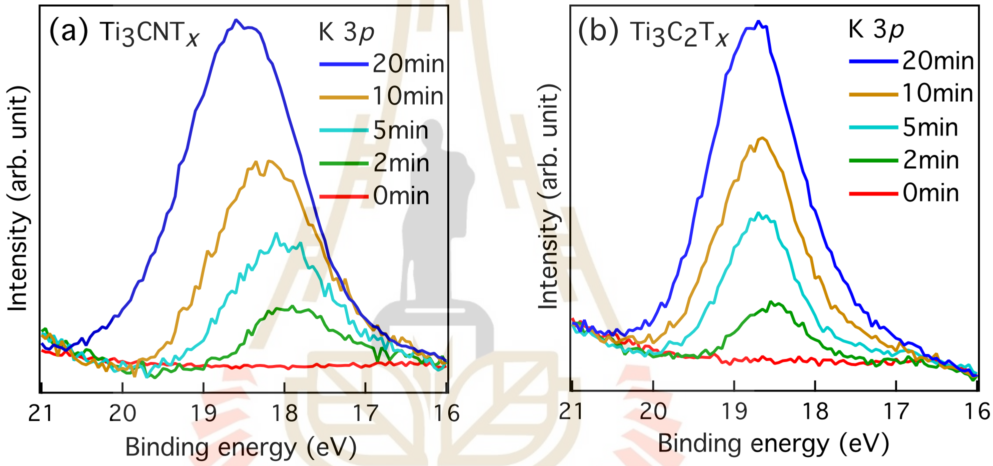

Figure 5.4 K 3p core-level spectra of (a) Ti_3CNT_x and (b) $Ti_3C_2T_x$ samples, shown in a function of potassium deposition time (adapted from (Jindata et al., 2021)).

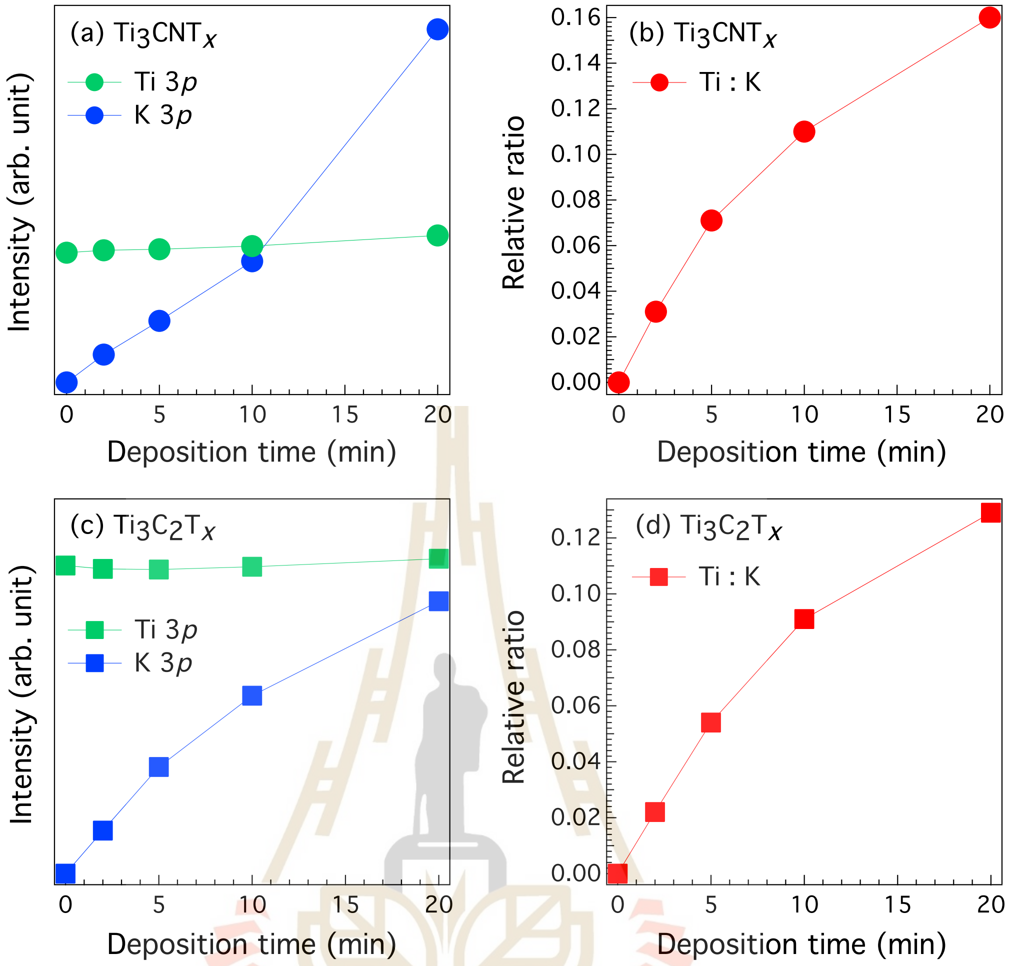

Figure 5.5 (a), (c) The integrated intensities under the areas of Ti 3p (green color) and K 3p (blue color) core-level spectra for Ti_3CNT_x and $Ti_3C_2T_x$ respectively. (b), (d) Corresponding the relative ratio of Ti to K (red color) as a function of potassium deposition time of the Ti_3CNT_x and $Ti_3C_2T_x$, respectively (Jindata et al., 2021).

Table 5.1 Results of the K concentrations for *in situ* K deposition on Ti_3CNT_x surface (adapted from (Jindata et al., 2021)).

Experimental measurement of Ti_3CNT_x	Ti : K (experiment Ti_3CNT_x)	The estimated K concentrations in Ti_3CNO_2 model	I_{Ti3p} (simulation Ti_3CNO_2)	I_{K3p} (simulation Ti_3CNO_2)	Ti : K (simulation Ti_3CNO_2)
2min doping	0.031	$K_{0.10}Ti_3CNO_2$	1.41×10^{-4}	4.41×10^{-6}	0.031
5min doping	0.071	$K_{0.23}Ti_3CNO_2$	1.37×10^{-4}	9.83×10^{-6}	0.071
10min doping	0.110	$K_{0.35}Ti_3CNO_2$	1.32×10^{-4}	1.45×10^{-5}	0.110
20min doping	0.160	$K_{0.51}Ti_3CNO_2$	1.27×10^{-4}	2.03×10^{-5}	0.160

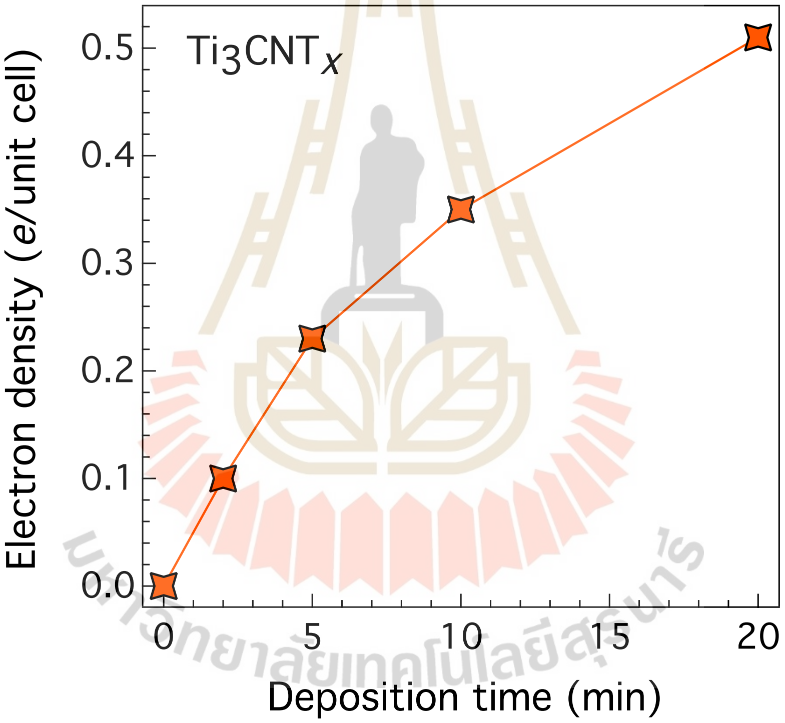

Figure 5.6 The estimated electron density of Ti_3CNT_x sample (Jindata et al., 2021).

Table 5.2 Results of the K concentrations for *in situ* K deposition on $Ti_3C_2T_x$ surface (adapted from (Jindata et al., 2021)).

Experimental measurement of $Ti_3C_2T_x$	Ti : K (experiment $Ti_3C_2T_x$)	The estimated K concentrations in $Ti_3C_2O_2$ model	I_{Ti3p} (simulation $Ti_3C_2O_2$)	I_{K3p} (simulation $Ti_3C_2O_2$)	Ti : K (simulation $Ti_3C_2O_2$)
2min doping	0.022	$K_{0.07}Ti_3C_2O_2$	1.41×10^{-4}	3.09×10^{-6}	0.022
5min doping	0.054	$K_{0.18}Ti_3C_2O_2$	1.37×10^{-4}	7.75×10^{-6}	0.054
10min doping	0.091	$K_{0.29}Ti_3C_2O_2$	1.34×10^{-4}	1.22×10^{-5}	0.091
20min doping	0.129	$K_{0.41}Ti_3C_2O_2$	1.29×10^{-4}	1.67×10^{-5}	0.129

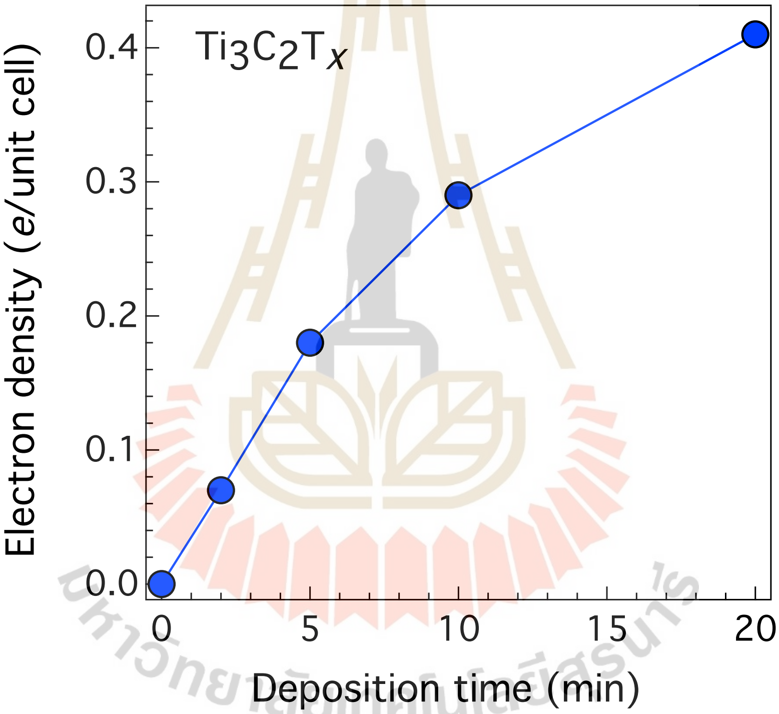

Figure 5.7 The estimated electron density of $Ti_3C_2T_x$ sample (Jindata et al., 2021).

5.3.2.2 The extraction of the Ti 3p core-level and valence band shifts upon potassium doping

In this work, the evolutions of the chemical potential shift of Ti 3p core-level and valence band of Ti_3CNT_x and $Ti_3C_2T_x$ upon potassium deposition were measured by ultraviolet photoemission spectroscopy (UPS). To determine the Ti 3p and valence band peak positions, UPS spectra were subtracted by the Shirley background to exclude extrinsic effects (Shirley, 1972; Norgren et al., 1994; Grosvenor et al., 2004). After that, the analyzed spectra were fitted by using the Gaussian equation and the peak positions could be obtained. The fitting equation is expressed by the following:

$$f(x) = A_0 \exp\left[-(\tfrac{x-x_0}{w})^2\right] + SB \tag{5.2}$$

where, A_0 is amplitude, x_0 is peak position, w is full width at half maximum (FWHM), and SB is the Shirley background. The example of UPS fitting for Ti_3CNT_x and $Ti_3C_2T_x$ are shown in figures 5.8 and 5.9 where blue, orange, and green curves are the measured UPS spectra, Gaussian fitted curve, and the Shirley background, respectively.

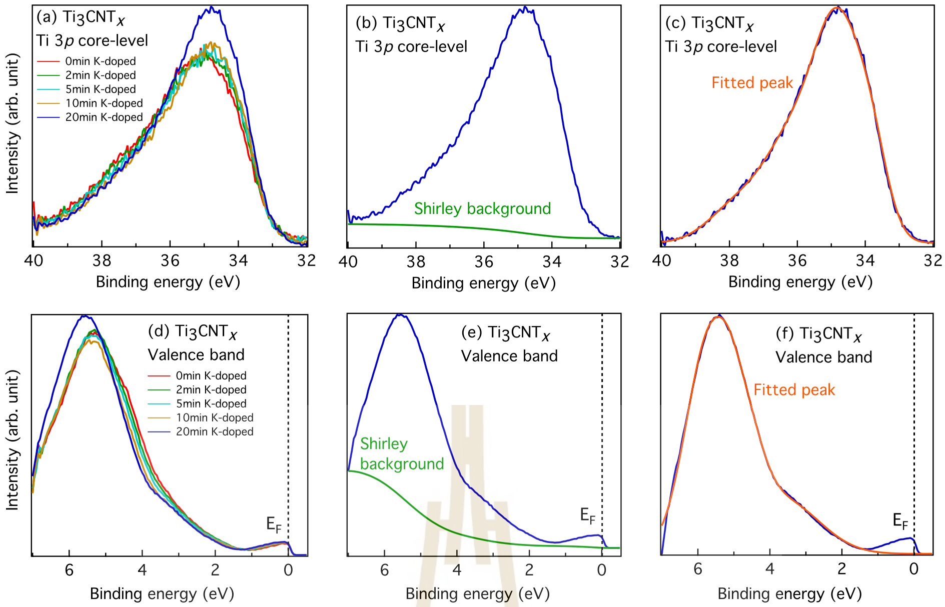

Figure 5.8 (a), (d) UPS spectra of the Ti 3p core-level and valence band of the Ti_3CNT_x as a function of potassium deposition time. (b), (c) and (e), (f) The example of Gaussian fitting at Ti 3p core-level and valence band states, respectively (Jindata et al., 2021).

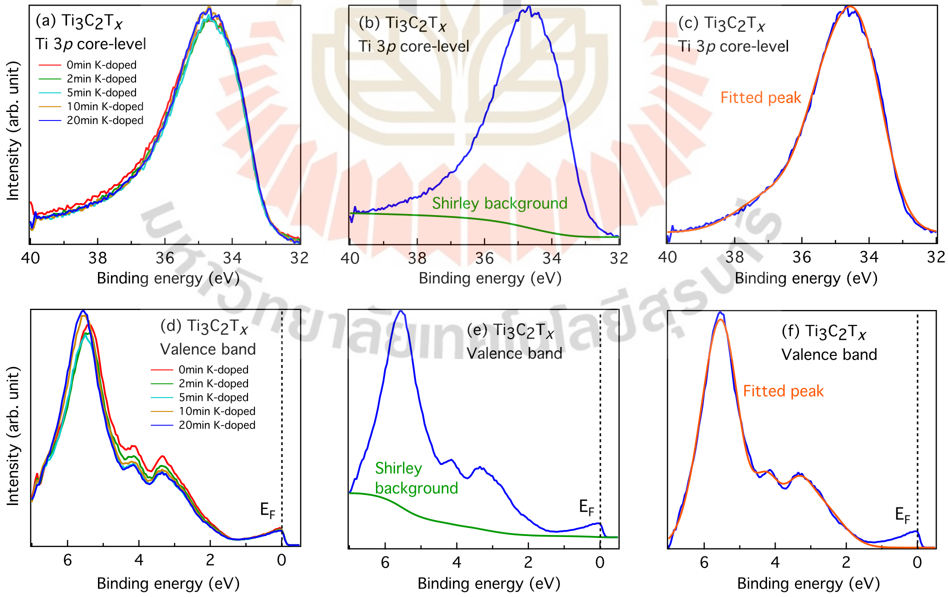

Figure 5.9 (a), (d) UPS spectra of the Ti 3p core-level and valence band of the $Ti_3C_2T_x$ as a function of potassium deposition time. (b), (c) and (e), (f) The example of Gaussian fitting at Ti 3p core-level and valence band states, respectively (Jindata et al., 2021).

5.3.3 Results of the chemical potential shifts of potassium doped Ti_3CNT_x and $Ti_3C_2T_x$ by UPS measurement

The change of chemical potential ($\Delta\mu$) as a function of doping can be deduced from the binding energy shift with reference to electronic states located below the E_F; for example, the valence band (VB) (Shen et al., 2004) and the core-level (Yagi et al., 2006; Fujimori et al., 1998; Fujimori et al., 2002; Maiti et al., 2009). As shown in figures 5.10(a) and 5.11(a), a wide binding energy range from 0 to 42 eV used in our experiments covers the E_F, VB, O 2p, K 3p and Ti 3p core-levels, allowing simultaneous detection of the change of the VB and the MXenes' titanium electronic structure as well as the K dopant. The Ti 3p core-level spectra of pristine (undoped) samples were immediately measured after cleaving the surface and we observed that the Ti 3p of Ti_3CNT_x appears at ~0.5 eV higher binding energy than $Ti_3C_2T_x$, resulting from an effect of the titanium bonding with a highly electronegative (EN) nitrogen atom. In addition, as expected for metallic Ti-based MXenes, a spectral weight at the E_F can be observed for both Ti_3CNT_x and $Ti_3C_2T_x$, which is mainly contributed from the Ti 3d states (Enyashin et al., 2013). Since the Ti 3p core-level and VB were measured relative to the E_F, we can extract the evolution of the chemical potential shift of both samples as normalized by setting their E_F at 0 eV. The spectral intensity of both Ti 3p core-level and VB are relatively unchanged during the experiment, however, these spectra were stacked in order to follow the chemical potential shift in a function of electron density (figures 5.10(b-c) and 5.11(b-c)). Unlike $Ti_3C_2T_x$, Ti_3CNT_x shows a distinctly opposite sign in binding energy shift between the Ti 3p core-level and VB upon electron doping (figures 5.10(b) and 5.10(c)). The VB shows the shift to higher binding energies of ~160 meV corresponding to an increase of μ, which is consistent with the results of electrons transfer from potassium to the MXene (figure 5.10(c)). Strikingly, we find an anomalous shift of the Ti 3p core-level to lower binding energies of up to ~250 meV upon increasing the electron density (figure 5.10(b)). This anomalous shift to a lower binding energy indicates a decrease of μ with increasing the electron densities, a signature of the NEC effect.

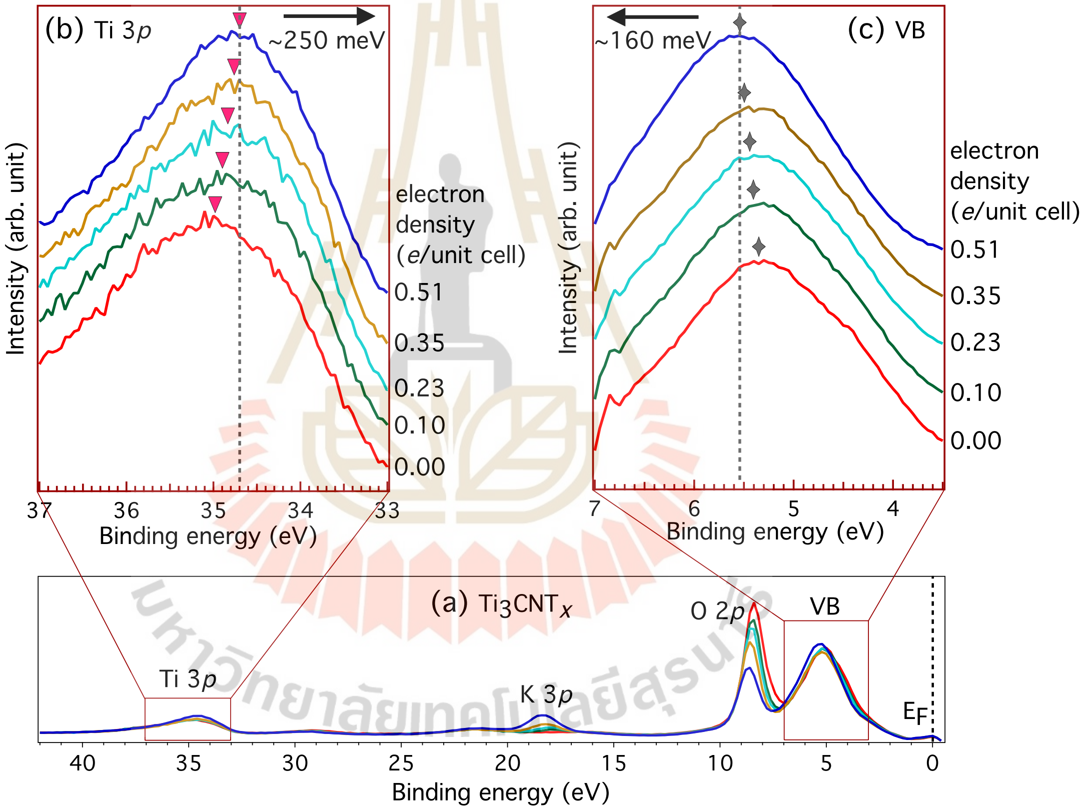

Figure 5.10 (a) Angle-integrated photoemission spectra and evolution of the chemical potential shift ($\Delta\mu$) of (b) Ti 3p core-level and (c) VB, shown in a function of electron density for Ti_3CNT_x (Jindata et al., 2021).

By contrast, this feature is not observed in $Ti_3C_2T_x$, where a shift to higher binding energies of up to ~100 meV was observed for both Ti 3p core-level and

VB upon increasing the electron densities (figures 5.11(b) and 5.11(c)). A decrease in spectral intensity of oxygen surface termination (O 2p) as compared with the Ti 3p for both Ti_3CNT_x and $Ti_3C_2T_x$ samples may be attributed to O-depletion caused by K evaporation during the experiments. However, this O-depletion was not observed in the UPS data of the *in situ* K deposition on Ti_3CNT_x surface recorded at the BL 3.2Ua of the Synchrotron Light Research Institute (SLRI) for reproducibility test, which might be due to a few oxygen contaminations inside the beamline with a pressure of 1.5×10^{-9} Torr. The chemical potential shift of both Ti 3p core-level and VB were reproducibly observed in Ti_3CNT_x and $Ti_3C_2T_x$ samples, shown in figures 5.12 and 5.13, respectively.

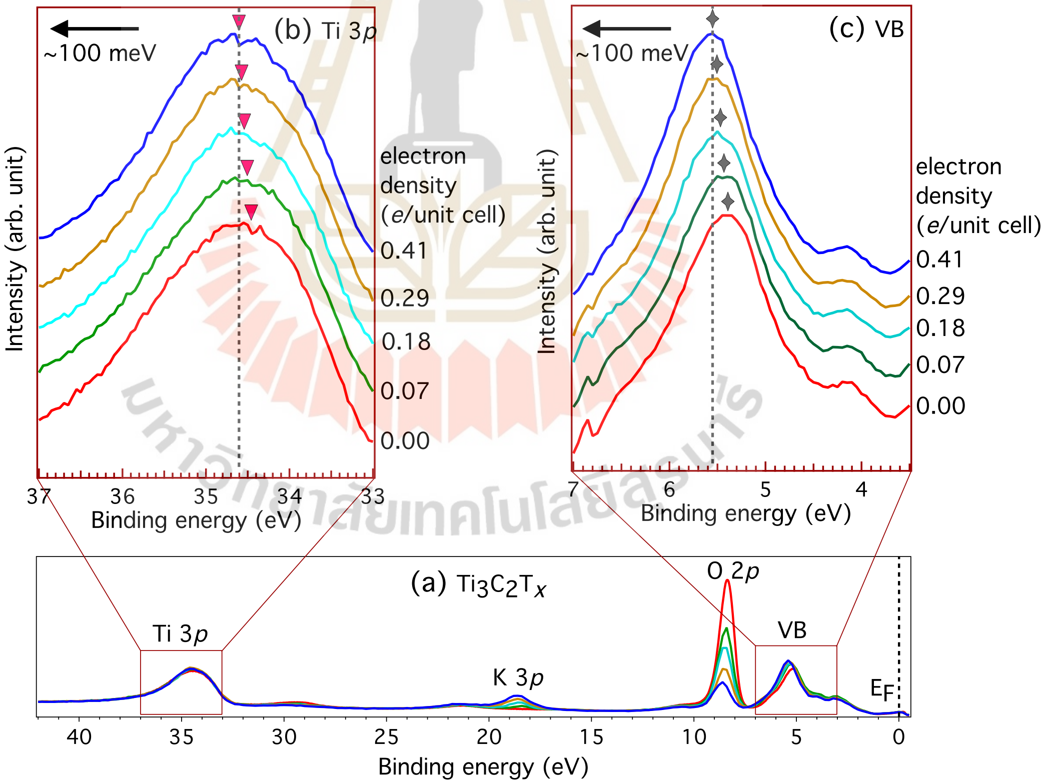

Figure 5.11 (a) Angle-integrated photoemission spectra and evolution of the chemical potential shift ($\Delta\mu$) of (b) Ti 3p core-level and (c) VB, shown in a function of electron density for $Ti_3C_2T_x$ (Jindata et al., 2021).

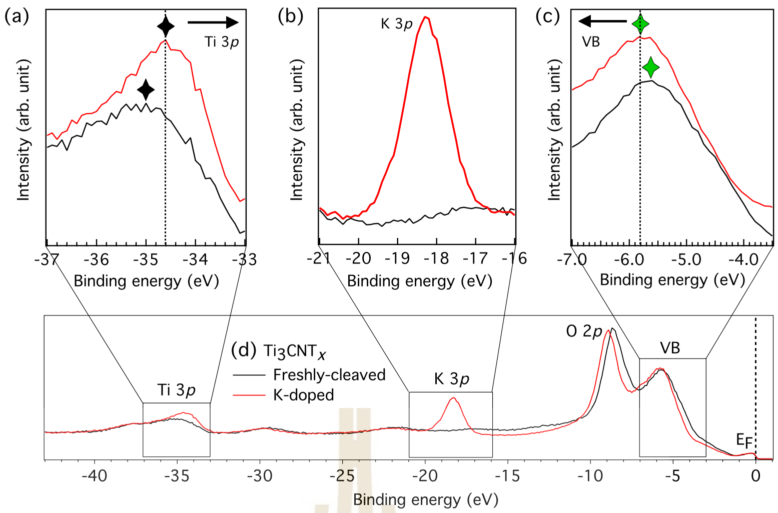

Figure 5.12 Reproducibility of the UPS data of the *in situ* K deposition on Ti_3CNT_x surface measured at the BL 3.2Ua of SLRI in Thailand. Black and green diamond symbols indicate spectral peaks of (a) Ti 3p core-level and (c) VB, respectively (Jindata et al., 2021).

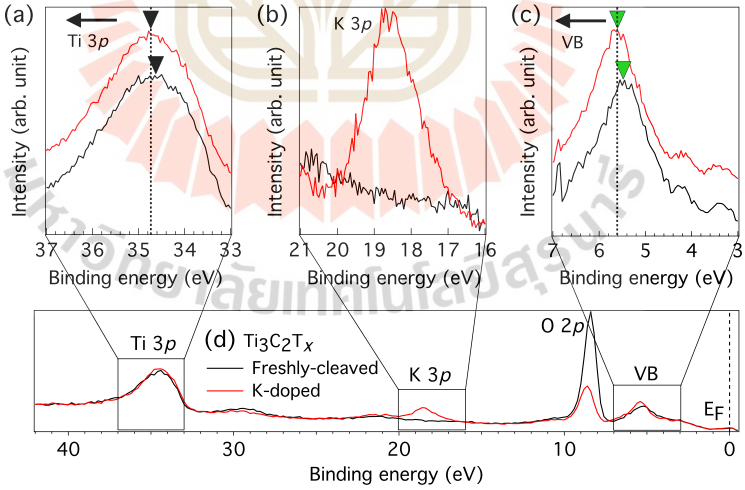

Figure 5.13 Reproducibility of the UPS data of the *in situ* K deposition on $Ti_3C_2T_x$ surface measured at MERLIN BL 4.0.3 of ALS in USA. Black and green triangle symbols indicate spectral peaks of (a) Ti 3p core-level and (c) VB, respectively (Jindata et al., 2021).

Our *in situ* UPS results provide a direct experimental evidence of a significant difference of the electronic structures between Ti_3CNT_x and $Ti_3C_2T_x$, in spite their seemingly similar crystal structures. Importantly, this is the first report on the spectroscopic signature of NEC for a MXene, whereas NEC has been experimentally observed in other 2D materials such as WSe_2 by *in situ* angle-resolved photoemission (ARPES) measurements (Riley et al., 2015). The negative shift to a lower binding energy of Ti 3p core-level of about 250 meV at 0.51*e* per unit cell observed in Ti_3CNT_x is larger to that observed for the Sr 3d and Ir 4f core-level in $Sr_3Ir_2O_7$ as it shows the negative shift to a lower binding energy of around 100 meV upon electron doping (He et al., 2015).

5.4 Density functional theory (DFT) calculations

5.4.1 Ti 3p core-level and valence band shifts calculation

To shed some light on our experimental findings, we calculate the chemical potential shifts for Ti 3p core-level and VB of Ti_3CNO_2 and $Ti_3C_2O_2$ structures under different electron doping from 0 to 0.5*e* per unit cell, as shown in figures 5.14 and 5.16, respectively. The calculated absolute binding energies of Ti 3p core-level are obtained by using the initial state (Z+1) approximation (Fongkaew et al., 2017). Our calculation shows that the absolute binding energies of Ti 3p core-level of the pristine (undoped) Ti_3CNO_2 and $Ti_3C_2O_2$ structures are located at 33.61 eV and 33.04 eV, respectively, while the Ti 3p core-level of Ti_3CNO_2 shows 0.57 eV higher binding energy than that of $Ti_3C_2O_2$, in agreement with the experimental data shown in figures 5.10(b) and 5.11(b). The chemical potential shift ($\Delta\mu$) values of Ti 3p core-level of Ti_3CNO_2 and $Ti_3C_2O_2$ as a function of electron density presented in figures. 5.14 and

5.16, are obtained by determining their calculated absolute binding energies relative to the change of the E_F upon electron doping. The energy band theory of metals defines the VB level as the highest occupied state of electrons, allowing us to use the change of the E_F during electron doping as a reference for the chemical potential shifts of VB. The MXene structures with the O terminations located on top of Ti middle layers (FCC sites) were used in our calculations, due to their structural stability, and they are expected to be a majority of the surface terminations of MXenes synthesized by this method (Schultz et al., 2019).

Figure 5.14 shows the consistency of general trends in the chemical potential shift for titanium carbonitride between experimental measurement on Ti_3CNT_x (T_x is a mixture of −O, −F, and –Cl terminations) and calculation using Ti_3CNO_2 with alternately mixed C/N structure. Both, the experiment data and calculations, show the opposite direction of the shifts of Ti 3p core-level to lower binding energies while VB shifts to higher binding energies upon electron doping. However, the calculated Ti 3p core-level and VB shifts (green and yellow solid lines in figure 5.14) are lower than the experimental values measured by UPS, which might stem from the nonstoichiometric nitrogen contents in the as-synthesized titanium carbonitride (Hantanasirisakul et al., 2019). Also, the difference in the degree of the chemical potential shift can be due to the mixed surface termination present in the as-synthesized MXene compared to the O-termination structures used in calculations. The effects of surface terminations on NEC behavior warrant further investigations. Lastly, the inconsistency could be caused by the calculation of absolute core-level binding energies using the initial state approximation, which neglects core-hole interactions.

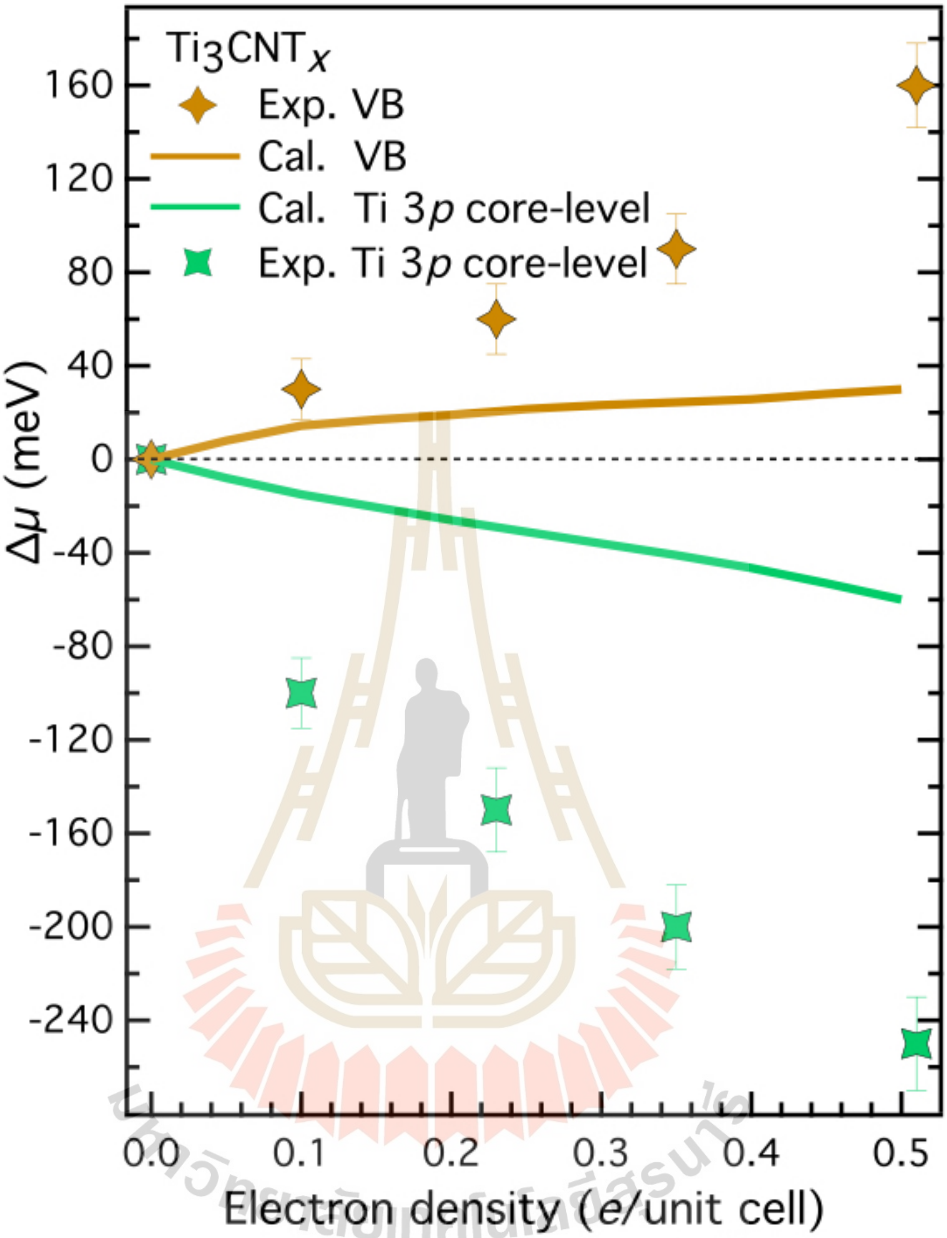

Figure 5.14 Summary of the chemical potential shift ($\Delta\mu$) of Ti 3*p* core-level and VB for UPS measurement of Ti_3CNT_x versus DFT calculation of Ti_3CNO_2. Green and yellow markers represent the $\Delta\mu$ of experimental data for Ti 3p core-level and VB, respectively. Error bars of the experimental data reflect the uncertainty in determining the peak energy position. Green and yellow solid lines represent the $\Delta\mu$ of calculation data for Ti 3p core-level and VB, respectively (Jindata et al., 2021).

Moreover, we calculated the Ti 3p core-level and VB shift titanium carbonitride structure with the various the nitrogen content. We observed that the signature of NEC can be observed in titanium carbonitride with different ratios of C/N (Ti_3CNO_2 and $Ti_3C_{0.5}N_{1.5}O_2$) as shown in figure 5.15.

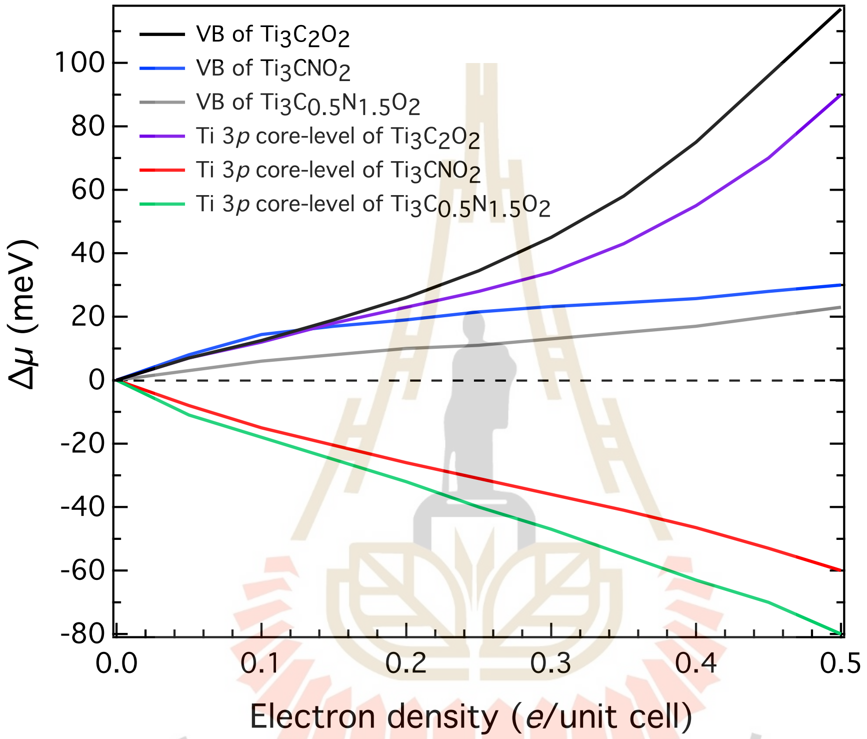

Figure 5.15 DFT calculations of the Ti 3p core-level and VB shifts considering the effect of the nitrogen content in the Ti_3CNO_2 structure (Jindata et al., 2021).

Figure 5.16 shows the same direction of the chemical potential shift for the titanium carbide for experimental measurement of $Ti_3C_2T_x$ and calculations of $Ti_3C_2O_2$ as it shows both, the Ti 3p core-level and VB, shift to higher binding energies upon electron doping. The closer values between experimental and calculation observed in the carbide may be ascribed to less structural variation between the as-synthesized MXene used in the experiment and $Ti_3C_2O_2$ structure used in the DFT calculations.

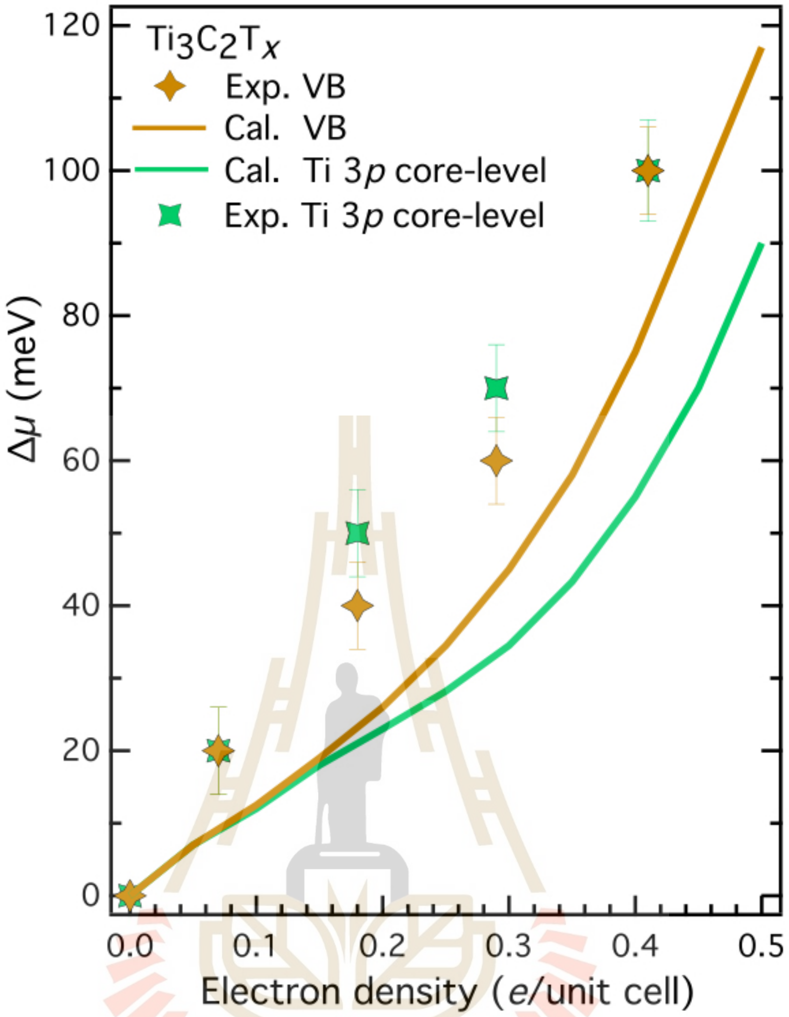

Figure 5.16 Summary of the chemical potential shift (Δμ) of Ti 3p core-level and VB for UPS measurement of $Ti_3C_2T_x$ versus DFT calculation of $Ti_3C_2O_2$. Green and yellow markers represent the Δμ of experimental data for Ti 3p core-level and VB, respectively. Error bars of the experimental data reflect the uncertainty in determining the peak energy position. Green and yellow solid lines represent the Δμ of calculation data for Ti 3p core-level and VB, respectively (Jindata et al., 2021).

Intriguingly, as shown in figure 5.17, our calculations show the shift of the E_F of Ti_3CNO_2 (red line) to a higher energy level at a much slower rate than the E_F of $Ti_3C_2O_2$ (blue line) of around four times after doping of 0.5*e* per unit cell, indicating that Ti_3CNO_2 has more available states to receive the extra electrons above the E_F than $Ti_3C_2O_2$.

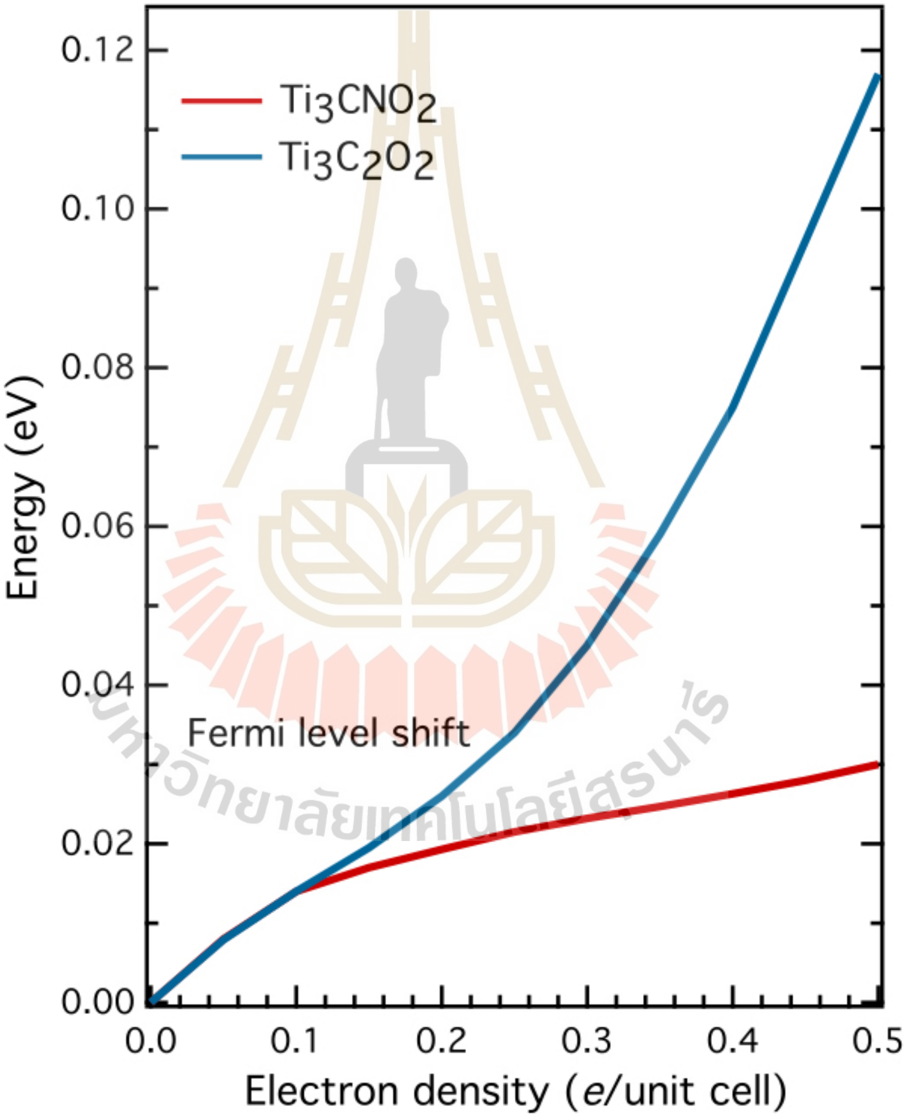

Figure 5.17 Comparison of the calculated change of the E_F upon increasing the electron density between Ti_3CNO_2 (red line) and $Ti_3C_2O_2$ (blue line) (Jindata et al., 2021).

5.4.2 Density of states (DOS) calculation

To confirm the difference of the electronic structure between the two MXenes, we compare the density of states (DOS) calculations near the E_F of Ti_3CNO_2 and $Ti_3C_2O_2$ (figure 5.18). To allow a direct comparison, the DOS of two MXenes are aligned with the same range of energy (see figure 5.19 for the full DOS in the VB region). As shown in figure 5.18, the partial density of states (PDOS) of Ti 3d orbital (green color) mainly dominates followed by a few PDOS of N 2p (blue color), C 2p (black color) and O 2p (red color) orbitals, indicating that Ti 3d orbitals play the most important role in receiving electron doping in both Mxenes. More importantly, we find that the Ti_3CNO_2 has the additional PDOS of N p orbital (blue color) near the E_F. Therefore, it would be expected that the difference of the X elements between Ti_3CNT_x and $Ti_3C_2T_x$ can lead to the difference in electronic structure of the two Mxenes. The calculations show that Ti_3CNO_2 has the higher total DOS below the E_F than $Ti_3C_2O_2$, in agreement with the experimental data shown in figures 5.10(a) and 5.11(a). Interestingly, the Ti_3CNO_2 shows PDOS of Ti d orbital distinctively higher than that of $Ti_3C_2O_2$.

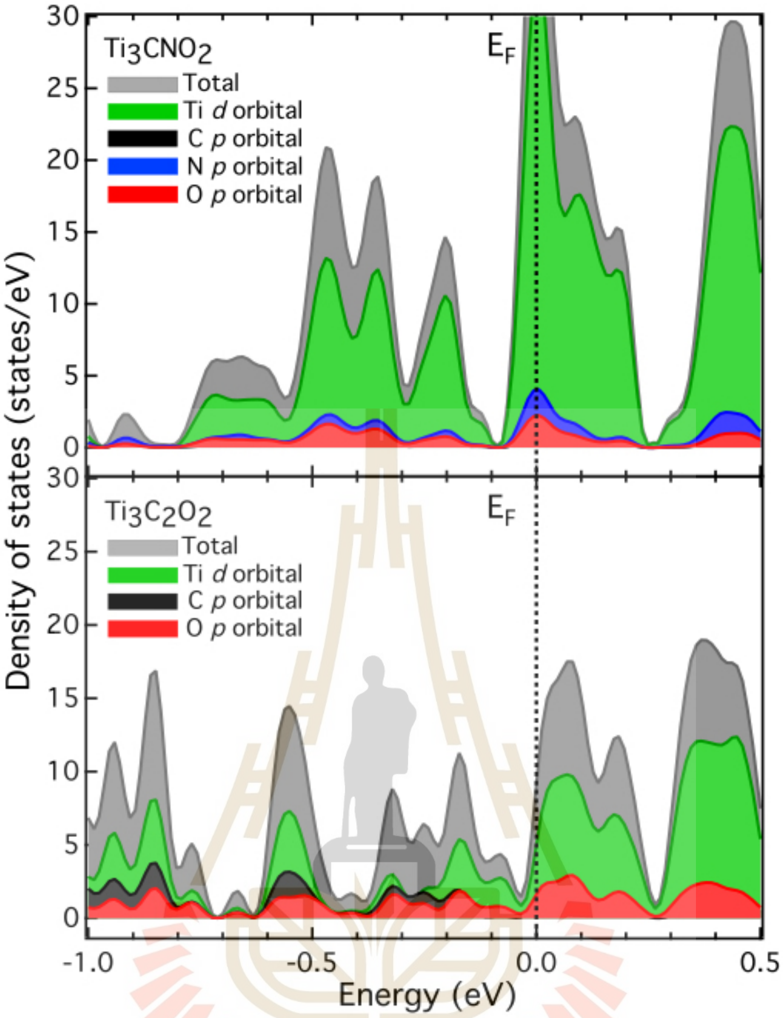

Figure 5.18 Comparison of the calculated density of states (DOS) near the E_F between Ti_3CNO_2 and $Ti_3C_2O_2$. The total DOS and that of Ti, C, N and O are presented by grey, green, black, blue, and red colors, respectively. The E_F is set to 0 eV (Jindata et al., 2021).

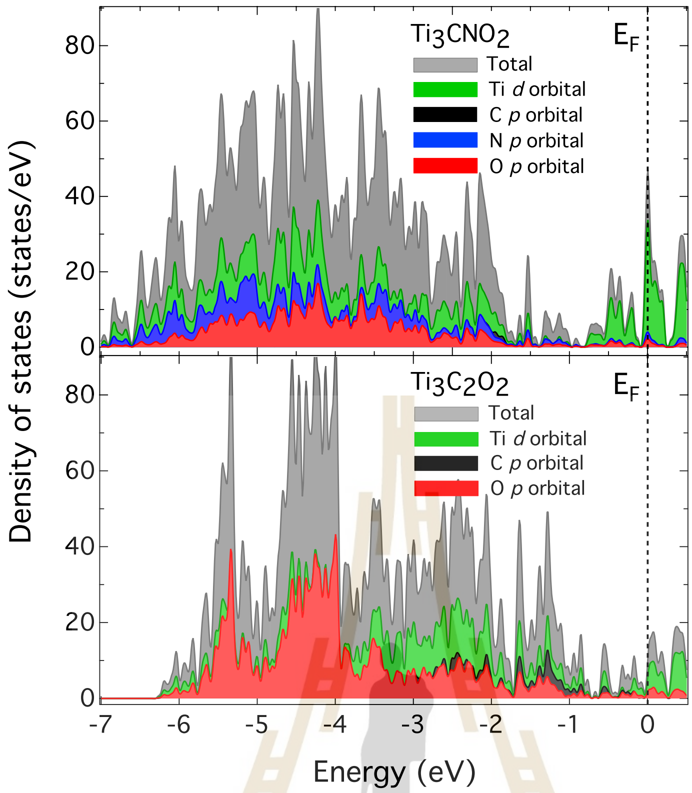

Figure 5.19 The full DOS covering the near E_F and valence band states of energy -7 to 0.5 eV of Ti_3CNO_2 and $Ti_3C_2O_2$ (adapted from (Jindata et al., 2021)).

The difference in the DOS between two MXenes is fully supported by our DOS extraction at the E_F ($N(E_F)$) and above the E_F (available states) from 0 to 0.5 eV of Ti, C, N and O elements, as summarized in table 5.3. The results confirm that Ti_3CNO_2 has a much larger $N(E_F)$ and Ti available states than $Ti_3C_2O_2$, in good agreement with the data reported in other works (Lu et al., 2020; Sun et al., 2020). Importantly, the N available states appear only in the Ti_3CNO_2. A few of the C available states is rather small and similar in both Mxenes. In addition, the O available states in $Ti_3C_2O_2$ is higher than Ti_3CNO_2. Thus, our calculation suggests that the increase of the Ti available states in Ti_3CNO_2 can be attributed from the titanium-nitrogen bonding in Ti_3CNO_2, which helps promoting the Ti 3d available states of Ti atoms above the E_F, and consequently enhancing the potentiality of Ti_3CNO_2 for receiving more electron than $Ti_3C_2O_2$.

Table 5.3 The calculated DOS at the E_F ($N(E_F)$) and above the E_F from 0 to 0.5 eV (available states) of Ti, C, N and O atoms in states/eV. The DOS of Ti, C, N and O available states are given as normalized by the total number of each atoms in unit cell (adapted from (Jindata et al., 2021)).

MXene	$N(E_F)$	Ti available states	C available states	N available states	O available states
Ti_3CNO_2	5.67	3.36	0.09	0.28	0.14
$Ti_3C_2O_2$	1.30	1.92	0.11	-	0.39

5.4.3 Charge density difference and Bader charge calculation

To obtain insights into the role of nitrogen on charge storage mechanism underlying the observed spectroscopic signature of NEC, we perform the charge density difference calculations, which is reported on a charge accumulation (yellow color) and charge loss (light blue color) upon electron doping of 0.5*e* per supercell in Ti_3CNO_2 and $Ti_3C_2O_2$ (figures 5.20(a) and 5.20(b)). This allows a direct comparison with the DOS near E_F of both Mxenes in figure 5.18. These calculations were subtracted by the existing charge density from the pristine (undoped) structure, allowing us to observe the local charge accumulation after the doping. As shown in figures 5.20(a) and 5.20(b), the electron accumulation is localized at the bonding of Ti d – X p orbitals and Ti d – O p orbitals for both Mxenes. Since the X layers in Ti_3CNO_2 are composed of C and N atoms, while that of $Ti_3C_2O_2$ has only C, it is clear that X layers play a significant role in causing the different mechanisms of charge storage between the two MXenes.

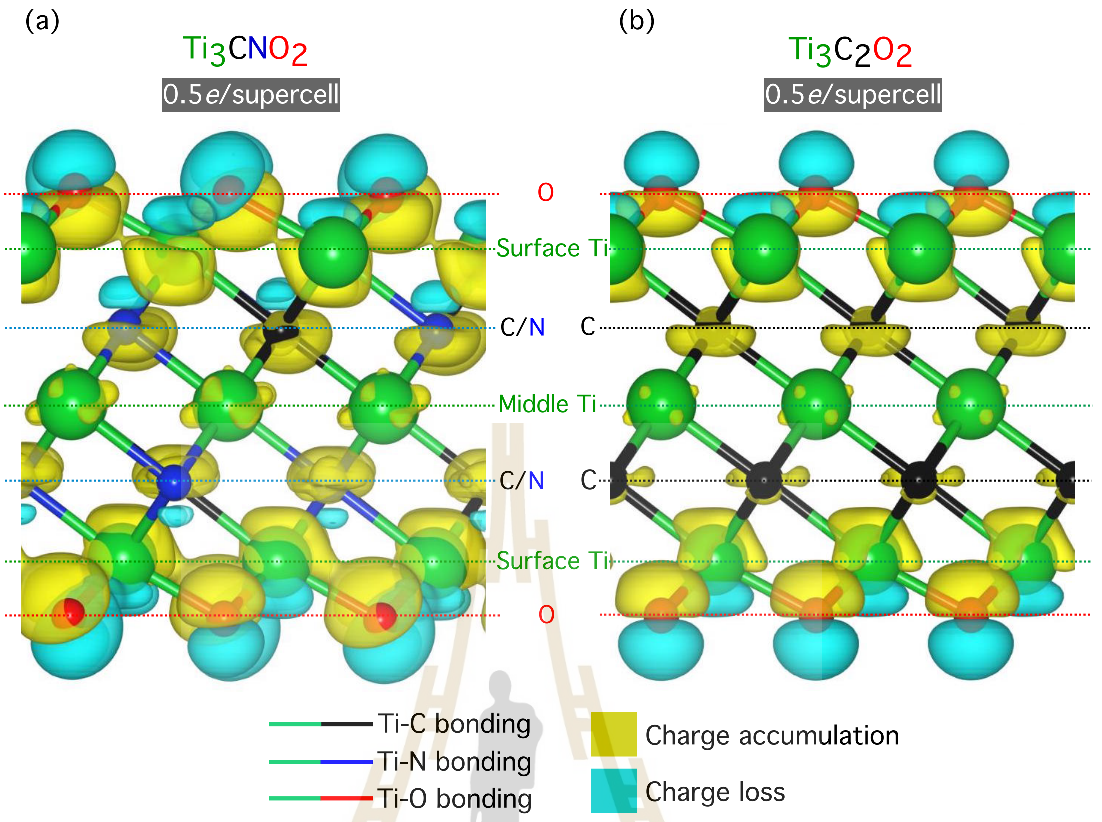
(a)
Ti_3CNO_2
0.5e/supercell
(b)
$Ti_3C_2O_2$
0.5e/supercell
O
Surface Ti
C/N
C
Middle Ti
C/N
C
Surface Ti
O
Ti-C bonding
Ti-N bonding
Ti-O bonding
Charge accumulation
Charge loss

Figure 5.20 The calculated charge density difference of (a) Ti_3CNO_2 and (b) $Ti_3C_2O_2$ upon electron doping of 0.5*e* per supercell. Both (a) and (b) are shown with the same isosurface level of 0.0005. The charge accumulation region is displayed in yellow color while the charge loss region is in light blue color (adapted from (Jindata et al., 2021)).

To uncover this difference, we calculate the Bader charge and compared the percentage of charge density distribution as a function of electron doping for both Mxenes, as shown in table 5.4. Starting from the Bader charge of Ti atoms in the pristine structure, which consist of the surface Ti and middle Ti atoms, we find that the surface Ti atoms have a lower Bader charge than the middle Ti atoms for both Mxenes resulting from the chemical bonding with oxygen surface termination, in good agreement with other published report (Sun et al., 2020). Moreover, the Bader charge of both surface

Ti and middle Ti in Ti_3CNO_2 is lower than $Ti_3C_2O_2$ due to higher electronegativity of N as discussed earlier. However, the Bader charges of C and O atoms are rather similar for both Mxenes. To track the charge localization on each atom after electron doping, we extracted the percentage of charge density distribution as a function of electron doping normalized by their Bader charge in the pristine structure. By comparing the doping at 0.3*e* per supercell of the two MXenes, the M layers including surface Ti and middle Ti; the X layers; and O layers contribute electron accumulations of ~31%, ~35.5%, ~24.5% and ~9%, respectively, verifying that the majority electrons are accumulated at the Ti d orbitals. We observe that the M layers in both Mxenes have similar behavior for receiving electrons, whereas the X layers are different. The N atoms can help accepting extra electrons together with C atoms in Ti_3CNO_2 for ~9.15% and ~16.23% respectively, while $Ti_3C_2O_2$ has only C atoms to accept the extra electrons. Surprisingly, after increasing the doping to 0.5*e* per supercell, the Ti_3CNO_2 has only a slight increase in electrons at surface Ti atoms (31.71%), whereas $Ti_3C_2O_2$ has a much larger charge accumulation at surface Ti atoms (38.30%), indicating that the N atoms in Ti_3CNO_2 help assisting the Ti atoms in receiving the electrons from the doping. We show the important role of N atoms in Ti_3CNO_2 that help promoting the Ti atoms to have more available states for receiving more electron doping above the E_F compared to $Ti_3C_2O_2$.

Table 5.4 The Bader charge and summary of the percentage of charge density distribution on surface Ti, middle Ti, C, N and O atoms in Ti_3CNO_2 (and $Ti_3C_2O_2$) supercell for 16 (16) atoms, 8 (8) atoms, 8 (16) atoms, 8 (-) atoms and 16 (16) atoms of surface Ti, middle Ti, C, N, and O, respectively (adapted from (Jindata et al., 2021)).

	Bader charge (pristine structure)		Charge density distribution (%)			
	Ti_3CNO_2	$Ti_3C_2O_2$	0.3*e* doping		0.5*e* doping	
			Ti_3CNO_2	$Ti_3C_2O_2$	Ti_3CNO_2	$Ti_3C_2O_2$
Surface Ti	2.247	2.274	30.15	31.38	31.71	38.30
Middle Ti	2.471	2.488	35.60	35.72	34.28	35.27
C	5.574	5.499	16.23	23.74	16.83	20.16
N	6.487	-	9.15	-	8.62	-
O	6.987	6.983	8.87	9.16	8.56	6.27

5.4.4 The effect of carbon and nitrogen distribution on the structural and electronic structure of titanium carbonitride

Furthermore, we investigate the effects of the C/N atomic distribution on the structural stability and electronic structure of the titanium carbonitrides. For this, we constructed Ti_3CNO_2 structures with C/N atoms in the X layers with 3 different atomic distributions: i) separately, where C and N atoms are in separate X layers, ii) alternately, where C and N atoms alternate mixed in both of the X layers, and iii) randomly, where C and N atoms random mixed in both of the X layers, as shown in figures 5.21(a) - 5.21(c), respectively. The total ground state energy of these structures is computed, as shown in table 5.5. By comparing the calculated total ground state energy, we find that the structure of randomly mixed C/N atoms has a lowest energy

(-527.921 eV) followed by the alternately mixed C/N atoms (-527.918 eV) and the separately C/N atoms (-527.494 eV), respectively, as summarized in table 5.5.

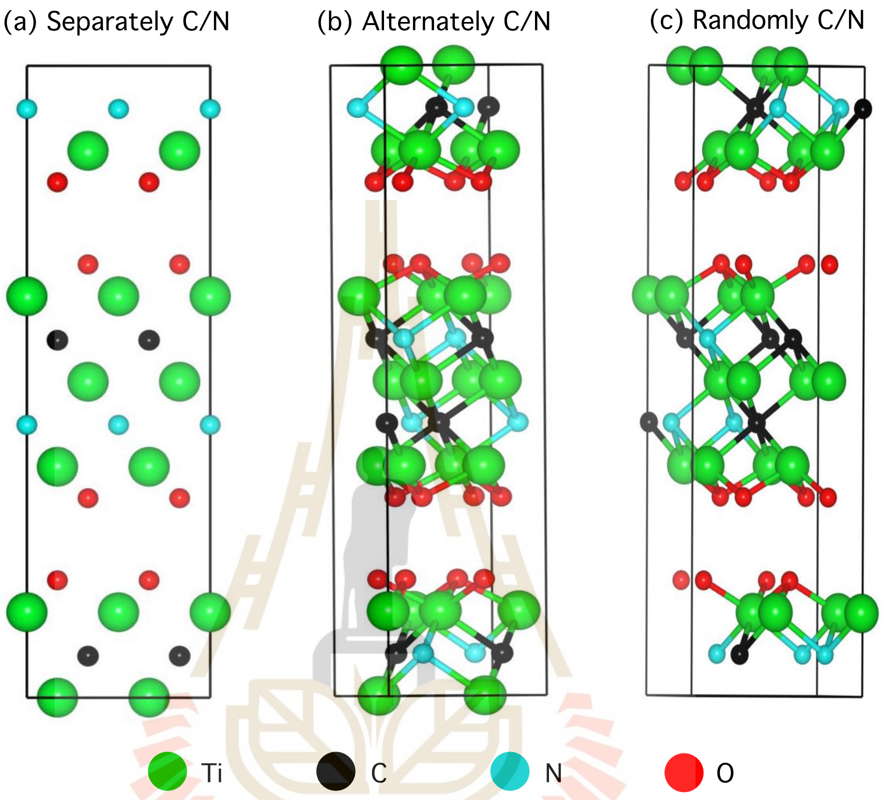
(a) Separately C/N (b) Alternately C/N (c) Randomly C/N

Figure 5.21 The relaxed structure of Ti_3CNO_2 shown in (a) separately C/N, (b) alternately mixed C/N, and (c) randomly mixed C/N, respectively (Jindata et al., 2021).

Table 5.5 The calculated total ground state energy for the different types of C/N atoms in the X layers of Ti_3CNO_2 structures (Jindata et al., 2021).

Structure	Total ground state energy (eV)
Separately C/N	-527.494
Alternately mixed C/N	-527.918
Randomly mixed C/N	-527.921

However, only structures (i) having separate C/N layers and structure and (ii) with alternate mixed C/N atoms in both X layers result in the signature of NEC, whereas structure (iii) having randomly mixed C/N atoms shows typical positive electronic compressibility (PEC) at low electron doping and NEC at higher electron doping (figures 5.14 and 5.22). Because it is less likely, entropically, for the C and N to separate in different X layers, the spectroscopic signature of NEC observed in this work could be used to imply that the titanium carbonitride prefers to have alternating C and N atoms with symmetrical arrangement of C and N atoms in the X layers than the randomly mixed structure. However, the exact arrangement of C and N atoms in titanium carbonitride MXene needs further exploration, which is beyond the scope of this work.

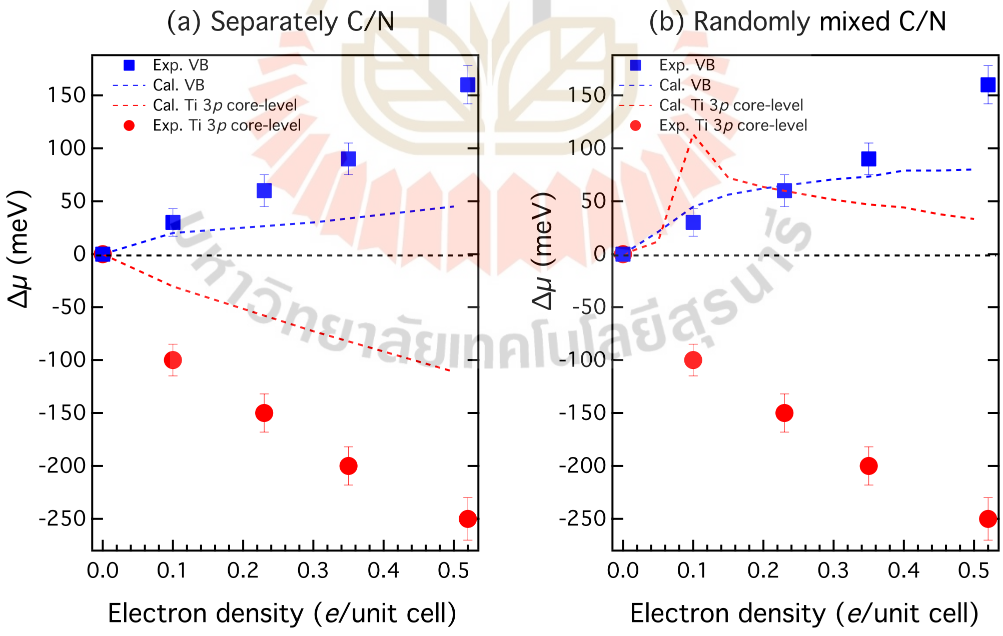

Figure 5.22 DFT calculations of the Ti 3p core-level and valence band shifts of (a) separately C/N atoms and (b) randomly mixed C/N atoms for Ti_3CNO_2 structures (Jindata et al., 2021).

CHAPTER VI

CONCLUSION

In this thesis, we systematically study the difference of the electronic structures between Ti_3CNT_x and $Ti_3C_2T_x$ MXenes as a function of electron density using a combination of UPS measurements and DFT calculations. We find that, in contrast to $Ti_3C_2T_x$, the Ti_3CNT_x exhibits the spectroscopic signature of negative electronic compressibility (NEC) as it shows the anomalous feature as the counterintuitive chemical potential shift of the Ti 3p core-level to a lower binding energies of up to 250 meV upon increasing the electron density. We interpret this counterintuitive chemical potential shift to lower binding energy observed in Ti_3CNT_x to the signature of the NEC effect which is defined as the chemical potential counterintuitively become lower upon increasing the electron density. To explain the experimental result, we perform the DFT calculations for the chemical potential shifts of Ti 3p core-level and VB upon electron doping in Ti_3CNO_2 and $Ti_3C_2O_2$ models in order to compare with the experimental data. As a result, the calculated chemical potential shifts agree well in general trend with the experimental UPS data. Moreover, our DFT calculations also show that the Ti_3CNT_x has more available states (unoccupied states) above the E_F to accepting more electron from doping than $Ti_3C_2T_x$. We confirm this calculation result by comparing the density of state (DOS) near the E_F between Ti_3CNO_2 and $Ti_3C_2O_2$. The DOS calculation demonstrates that the presence of nitrogen atoms in titanium carbonitride structure cause an increase in $N(E_F)$ and Ti 3d available states of Ti atoms above the E_F as compared to titanium carbide. More importantly, the calculated charge density difference and Bader charge analysis also further suggest that the signature of NEC in Ti_3CNT_x is resulted from the hybridization of titanium-nitrogen bonding in Ti_3CNT_x which plays an important role in promoting the Ti 3d available states of Ti atoms for receiving more electron above the E_F upon electron doping, driving the observed spectroscopic signature of NEC in Ti_3CNT_x. In addition, we discuss the chemical potential shift to higher binding energy upon electron doping for both Ti 3p core-level and VB of $Ti_3C_2T_x$ by the results of the positive electronic compressibility (PEC) effect which is described as the chemical potential shift should have the same shift to higher binding energy upon electron doping.

The NEC leads to the negative quantum capacitance which added to a set of conventional geometric capacitance, allowing more charge to be stored in the material. Our findings suggest that NEC is the explanation of how the capacitance of Ti_3CNT_x can be higher than that of $Ti_3C_2T_x$. Moreover, this study might assist with the fundamental understanding of the anomalously high absorption of electromagnetic waves of Ti_3CNT_x, which can be attributed to a peculiar characteristic of its electronic structure.

REFERENCES

REFERENCES

Anasori, B., and Gogotsi, Y. (2019). 2D Metal Carbides and Nitrides (MXenes): Structure, properties and Applications (Springer).

Alhabeb, M., Maleski, K., Anasori, B., Lelyukh, P., Clark, L., Sin, S., and Gogotsi, Y. (2017). Guidelines for synthesis and processing of two-dimensional titanium carbide ($Ti_3C_2T_x$ MXene). **Chemistry of Materials**. 29: 7633-7644.

Anasori, B., Lukatskaya, M. R., and Gogotsi, Y. (2017). 2D metal carbides and nitrides (MXenes) for energy storage. **Nature Reviews Materials**. 2: 16098.

Braaten, N. A., Grepstad, J. K., and Raaen, S. (1991). K promoted oxidation of Al and Ta. **Surface Science**. 250: 51-58.

Blöchl, P. E. (1994). Projector augmented-wave method. **Physical Review B**. 50(24): 17953-17979.

Chen, P., Pai, W. W., Chan, Y.-H., Sun, W.-L., Xu, C.-Z., Lin, D.-S., Chou, M. Y., Fedorov, A. V., and Chiang, T.-C. (2018). Large quantum-spin-Hall gap in single-layer 1T’ WSe_2. **Nature Communication**. 9: 2003.

Du, F., Tang, H., Pan, L., Zhang, T., Lu, H., Xiong, J., Yang, J., and Zhang, C. (2017). Environmental friendly scalable production of colloidal 2D titanium carbonitride MXene with minimized nanosheets restacking for excellent cycle life lithium-ion batteries. **Electrochimica Acta**. 235: 690-699.

Enyashin, A. N., and Ivanovskii, A. L. (2013). Two-dimensional titanium carbonitrides and their hydroxylated derivatives: Structural, electronic properties and stability of MXenes $Ti_3C_{2-x}N_x(OH)_2$ from DFTB calculations. **Journal of Solid State Chemistry**. 207: 42-48.

Eisenstein, J. P., Pfeiffer, L. N., and West, K. W. (1992). Negative compressibility of interacting two-dimensional electron and quasiparticle gases. **Physical Review Letter**. 68(5): 674-677.

Eisenstein, J. P., Pfeiffer, L. N., and West, K. W. (1994). Compressibility of the two-dimensional electron gas: Measurements of the zero-field exchange energy and fractional quantum Hall gap. **Physical review B**. 50(3): 1760-1778. Eknapakul, T., Fongkaew, I., Siriroj, S., Jindata, W., Chaiyachad, S., Mo, S.-K., Thakur, S., Petaccia, L., Takaki, H., Limpijumnong, S., and Meevasana, W. (2018). Direct observation of strain-induced orbital valence band splitting in $HfSe_2$ by sodium intercalation. **Physical review B**. 97: 201104(R).

Fongkaew, I., Akrobetu, R., Sehirlioglu, A., Voevodin, A., Limpijumnong, S., and Lambrecht, W. R. L. (2017). Core-level binding energy shifts as a tool to study surface processes on $LaAlO_3/SiTiO_3$. **Journal of Electron Spectroscopy and Related Phenomena**. 218: 21-29.

Fujimori, A., Ino, A., Mizokawa, T., Tsujioka, T., Yoshida, T., Satake, M., Okazaki, K., Eisaki, H., Uchida, S., Kishio, K., Taguchi, Y., Katsufuji, T., Tokura, Y., Yasui, Y., Nishikawa, T., and Sato, M. (1998). Chemical potential shifts in correlated electron systems studied by photoemission spectroscopy. **Journal of Electron Spectroscopy and Related Phenomena**. 92: 59-63.

Fujimori, A., Ino, A., Matsuno, J., Yoshida, T., Tanaka, K., and Mizokawa, T. (2002). Core-level photoemission measurements of the chemical potential shift as a probe of correlated electron systems. **Journal of Electron Spectroscopy and Related Phenomena**. 124: 127-138.

Gogotsi, Y., and Anasori, B. (2019). The rise of MXenes. **ACS Nano**. 13: 8491-8494.

Ghidiu, M., Lukatskaya, M. R., Zhao, M.-Q., Gogotsi, Y., and Barsoum M. W. (2014). Conductive two-dimesional titanium carbide 'clay' with high volumetric capacitance. **Nature**. 516: 78-81.

He, J., Hogan, T., Mion, T. R., Hafiz, H., He, Y., Denlinger, J. D., Mo, S.-K., Dhital, C., Chen, X., Lin, Q., Zhang, Y., Hashimoto, M., Pan, H., Lu, D. H., Arita, M., Shimada, K., Markiewicz, R. S., Wang, Z., Kempa, K., Naughton, M. J., Bansil, A., Wilson, S. D., and He, R.-H. (2015). Spectroscopic evidence for negative electronic compressibility in a quasi-three-dimensional spin-orbit correlated metal. **Nature Materials**. 14: 577-582.

Halim, J., Cook, K. M., Naguib, M., Eklund, P., Gogotsi, Y., Rosen, J., and Barsoum, M. W. (2016). X-ray photoemission spectroscopy of select multi-layered transition metal carbides (MXenes). **Applied Surface Science**. 362: 406-417.

Hantanasirisakul, K., and Gogotsi, Y. (2018). Electronic and optical properties of 2D transition metal carbides and nitrides (MXenes). **Advanced Materials**. 30: 1804479.

Hantanasirisakul, K., Alhabeb, M., Lipatov, A., Maleski, K., Anasori, B., Salles, P., Ieosakulrat, C., Pakawatpanurut, P., Sinitskii, A., May, S. J., and Gogotsi, Y. (2019). Effects of synthesis and processing on optoelectronic properties of titaniumcarbonitride MXene. **Chemistry of Materials**. 31: 2941-2951.

Hüfner, S. (1995). **Photoemission spectroscopy**. Berlin: Springer–Verlag.

Iqbal, A., Shahzad, F., Hantanasirisakul, K., Kim, M.-K., Kwon, J., Hong, J., Kim, H., Kim, D., Gogotsi, Y., and Koo, C. M. (2020). Anomalous absorption of electromagnetic waves by 2D transition metal carbonitride Ti_3CNT_x (MXene). **Science**. 369: 446-450.

Jhon, Y. I., Koo, J., Anasori, B., Seo, M., Lee, J. H., Gogotsi, Y., and Jhon, Y. M. (2017). Metallic MXene saturable absorber for femtosecond mode-locked lasers. **Advanced Materials**. 29: 1702496.

Jindata, W., Hantanasirisakul, K., Eknapakul, T., Denlinger, J. D., Sangphet, S., Chaiyachad, S., Jaisuk, C., Rasritat, A., Sawasdee, T., Nakajima, H., Rattanachata, A., Fongkaew, I., Limpijumnong, S., Gogotsi, Y., and Meevasana, W. (2021). Spectroscopic signature of negative electronic compressibility from the Ti core-level of titanium carbinitride MXene. **Applied Physics Reviews**. 8: 021401.

Kang, M., Kim, B., Ryu, S. H., Jung, S. W., Kim, J., Moreschini, L., Jozwiak, C., Rotenberg, E., Bostwick, A., and Kim, K. S. (2017). Universal Mechanism of band-gap engineering in transition-metal dichalcogenides. **Nano Letters**. 17: 1610-1615.

Khazaei, M., Arai, M., Sasaki, T., Chung, C.-Y., Venkataramanan, N. S., Estili, M., Sakka, Y., and Kawazoe, Y. (2013). Novel electronic and magnetic properties of two-dimensional transition metal carbides and nitrides. **Advanced Functional Materials**. 23: 2185-2192.

Krix, D., and Nienhaus, H. (2013). Low-temperature oxidation of alkali overlayers: Ionic species and reaction kinetics. **Applied Surface Science**. 270: 231-237.

Kerber, T., Sierka, M., and Sauer, J. (2008). Application of semiempirical long-range dispersion corrections periodic systems in density functional theory. **Journal of Computational Chemistry**. 29: 2088-2097.

Kim, B. S., Kyung, W. S., Seo, J. J., Kwon, J. Y., Denlinger, J. D., Kim, C., and Park, S. R. (2017). Possible electric field induced indirect to direct band gap transition in $MoSe_2$. **Scientific Reports**. 7: 5206.

Li, L., Richter, C., Peatel, S., Kopp, T., Mannhart, J., and Ashoori, R. C. (2011). Very large capacitance enhancement in a two-dimensional electron system. **Science**. 332: 825-828.

Lu, C., Yang, L., Yan, B., Sun, L., Zhang, P., Zhang, W., and Sun, Z. (2020). Nitrogen-doped Ti_3C_2 MXene: Mechanism investigation and electrochemical analysis. **Advanced Functional Materials**. 30: 2000852.

Lukatakaya, M. R., Bak, S.-M., Yu, X., Yang, X.-Q., Barsoum, M. W., and Gogotsi, Y. (2015). Probing the mechanism of high capacitance in 2D titanium carbide using in situ x-ray absorption spectroscopy. **Advanced Energy Materials**. 5: 1500589.

Lukatakaya, M. R., Kota, S., Lin, Z., Zhao, M.-Q., Shpigel, N., Levi, M. D., Halim, J., Taberna, P.-L., Barsoum, M. W., Simon, P., and Gogotsi, Y. (2017). Ultra-high-rate pseudocapacitive energy storage in two-dimensional transition metal carbides. **Nature energy**. 2: 17105.

Lv, B., Qian, T., and Ding H. (2019). Angle-resolved photoemission spectroscopy and its application to topological materials. **Nature Reviews Physics**. 1:609-626.

Maiti, K., Fink, J., Jong, S. J., Gorgoi, M., Lin, C., Raichle, M., Hinkov, V., Lambacher, M., Erb, A., and Golden, M. S. (2009). Doping dependence of the chemical potential and surface electronic structure in $YBa_2Cu_3O_{6+x}$ and $La_{2-x}Sr_xCuO_4$ using hard x-ray photoemission spectroscopy. **Physical Review B**. 80: 165132.

Magnusorn, M., Halim J., and Näslund, L.-Å. (2018). Chemical bonding in carbide MXene nanosheets. **Journal of Electron Spectroscopy and Related Phenomena**. 224: 27-32.

Ma, Y., Liu, N., Li, L., Hu, X., Zou, Z., Wang, J., Luo, S., and Gao, Y. (2017). A highly flexible and sensitive piezoresistive sensor based on MXene with greatly changed interlayer distances. **Nature Communications**. 8: 1207.

Nilson, K., Åhlund, J., Shariati, M.-N., Schiessling, J., Palmgren, P., Brena, B., Göthelid, E., Hennies, F., Huismans, Y., Evangelista, F., Rudolf, P., Göthelid, M., Mårtensson, N., and Puglia, C. (2012). Potassium-intercalated H_2Pc films: Alkali-induced electronic and geometrical modifications. **The Journal of Chemical Physics**. 137: 044708.

Naguib, M., Kurtoglu, M., Presser, V., Lu, J., Niu, J., Heon, M., Hultman, L., Gogotsi, Y., and Barsoum, M. W. (2011). Two-dimensional nanocrystal produced by exfoliation of Ti_3AlC_2. **Advanced Materials**. 23: 4248-4253.

Naguib, M., Unocic, R. R., Armstrong, B. L., and Nanda, J. (2015). Large-scale delamination of multi-layers transition metal carbides and carbonitrides "MXenes". **Dalton Transactions**. 44: 9353-9358.

Nathabumroong, S., Eknapakul T., Jaiban, P., Yotburat, B., Siriroj, S., Saisopa, T., Mo, S.-K., Supruangnet, R., Nakajima, H., Yimnirun, R., Maensiri, S., and Meevasana, M., (2020). Interplay of negative electronic compressibility and capacitance enhancement in lightly-doped metal oxide $Bi_{0.95}La_{0.05}FeO_3$ by quantum capacitance model. **Scientific Reports**. 10: 5153.

Nemšák, S., Shavorskiy, A., Karslioglu, O., Zegkionglou, I., Rattanachata, A., Conlon, C. S., Keqi, A., Greene, P. K., Burks, E. C., Salmassi, F., Gullikson, E. M., Yang, S.-H., Liu, K., Bluhm, H., and Fadley, C. S. (2014). Concentration and chemical-state profiles at heterogeneous interfaces with sub-nm accuracy from standing-wave ambient-pressure photoemission. **Nature Communications**. 5: 5441.

Persson, I., Näslund, L.-A., Halim J., Barsoum, M. W., Darakchieva, V., Palisaitis, J., Rosen, J., and Persson, P. O. Å. (2017). On the organization and thermal behavior of functional groups on Ti_3C_2 MXene surfaces in vacuum. **2D Materials**. 5: 015002.

Perdew, J. P., Burke, K., and Ernzerhof, M. (1996). Generalization gradient approximation made simple. **Physical Review Letters**. 77(18): 3865-3868.

Perdew, J. P., Burke, K., and Ernzerhof, M. (1997). Generalization gradient approximation made simple. **Physical Review Letters**. 78(7): 1396.

Riley, J. M., Meevasana, W., Bawden, L., Asakawa, M., Takayama, T., Eknapakul, T., Kim, T. K., Hoesch, M., Mo, S. K., Takagi, H. and Sasagawa, T. (2015). Negative electronic compressibility and tunable spin splitting in WSe_2. **Nature nanotechnology**. 10(12): 1043.

Riffe, D. M., Wertheim, G. K., and Citrin, P. H. (1990). Alkali-metal adsorbates on W(110): Ionic, covalent or metallic?. **Physical Review Letters**. 64(5) 571-574.

Rossnagel, K. (2010). Suppression and emergence of charge-density waves at the surfaces of layered $1T$-$TiSe_2$ and $1T$-TaS_2 by *in situ* Rb deposition. **New Journal of Physics**. 12: 125108.

Reinert, F. and Hüfner, S. (2005). Photoemission spectroscopy – from early days to recent applications. **New Journal of Physics**. 7: 97.

Shahzad, F., Alhabeb, M., Hatter, C. B., Anasori, B., Hong, S. M., Koo, C. M., and Gogotsi, Y. (2016). Electromagnetic interference shielding with 2D transition metal carbide (MXenes). **Science**. 353(6043): 1137-1140.

Schultz, T., Frey, N. C., Hantanasirisakul, K., Park, S., May, S. J., Shenoy, V. B., Gogotsi, Y., and Koch, N. (2019). Surface termination dependent work function and electronic properties of $Ti_3C_2T_x$ MXene. **Chemistry of Materials**. 31: 6590-6597.

Shi, X., Han, Z.-Q., Peng, X.-L., Richard, P. Qian, T., Wu, X.-X., Qiu, M.-W., Wang, S. C., Hu, J. P., Sun, Y.-J., and Ding, H. (2016). Enhanced superconductivity accompanying a Lifshitz transition in electron-doped FeSe monolayer. **Nature Communications**. 8: 14988.

Seah, M. P. and Dench, W. A. (1979). Quantitative electron spectroscopy of surface: A standard database for electron inelastic mean free paths in solds. **Surface and Interface Analysis**. 1: 2.

Shen. K. M., Ronning F., Lu, D. H., Lee, W. S., Ingle N. J. C., Meevasana, W., Baumberger, F., Damascelli, A., Armitage, N. P., Miller, L. L., Kohsaka, Y., Azuma, M., Takano, M., Takagi, H., and Shen, Z.-X. (2004). Missing Quasiparticles and the chemical potential puzzle in the doping ebolution of the cuprate superconductors. **Physical Review Letters**. 93: 267002.

Smekal, W., Werner, W. S. M., and Powell, C. J. (2005). Simulation of electron spectra for surface analysis (SESSA): a novel software tool for quantitative Auger-electron spectroscopy and X-ray photoelectron spectroscopy. **Surface and Interface Analysis**. 37: 1059-1067.

Sun, W., Wang, H.-W., Vlcek, L., Peng, J., Brady, A. B., Osti, N. C., Mamontov E., Tyagi, M., Nanda, J., Greenbaum, S. G., Kent, P. R. C., and Naguib, M. (2020). Multiscale and multimodal characterization of 2D titanium carbonitride MXene. **Advanced Materials Interface**. 7: 1902207.

VahidMohammadi, A., Rosen, J., and Gogotsi, Y. (2021). The world of two-dimensional carbides and nitrides (MXenes). **Science**. 372: 6547, eabf1581.

Wen, W., Zhao, G., Hong, C., Song, Z., and He, R.-H. (2020). 3D negative electronic compressibility as a new emergent phenomenon. **Journal of Superconductivity and Novel Magnetism**. 33: 229-239.

Waluyo, I., Mudiyanselage, K., Xu, F., An, W., Liu, P., Boscoboinik, J. A., Rodriguez, J. A., and Stacchiola, D. J. (2019). Potassium-promoted reduction of $Cu_2O/Cu(111)$ by CO. **The Journal of Physical Chemistry C**. 123: 8057-8066.

Werner, W. S. M., Smekal, W., Hisch, T., Himmelsbach, J., and Powell, C. J. (2013). Simulation of electron spectra for surface analysis (SESSA) for quantitative interpretation of (hard) X-ray photoelectron spectra (HAXPES). **Journal of Electron Spectroscopy and Related Phenomena**. 190: 137-143.

Ying, Y., Liu, Y., Wang, X., Mao, Y., Cao, W., Hu, P., and Peng, X. (2015). Two-dimensional titanium carbide for efficiently reductive removal of highly toxic chromium (VI) from Water. **ACS Applied Materials and Interfaces**. 7: 1795-1803.

Yagi, H., Yoshida, T., Fujimori, A., Kohsaka, Y., Misawa, M., Sasagawa, T., Takagi, H., Azuma, M., and Takano, M. (2006). Chemical potential shift in lightly doped to optimally doped $Ca_{2-x}Na_xCuO_2Cl_2$. **Physical Review B**. 73: 172503.

Zhang, C. J., Anasori, B., Seral-Ascaso, A., Park, S.-H., McEvoy, N., Shmeliov, A., Duesberg, G. S., Coleman, J. N., Gogotsi, Y., and Nicolosi, V. (2017). Transparent, flexible, and conductive 2D titanium carbide (MXene) films with high volumetric capacitance. **Advanced Materials**. 29: 1702678.

Zhang, W., Cheng, C., Fang, P., Tang, B., Zhang, J., Huang, G., Cong, X., Zhang, Ji, X., and Miao L. (2016). The role of terminations and coordination atoms in the pseudocapacitance of titanium carbonitride monolayers. **Physical Chemistry Chemical Physics**. 18: 4376-4384.

CURRICULUM VITAE

NAME	Mr. Warakorn Jindata
DATE OF BIRTH	December 1, 1990
PLACE OF BIRTH	Nan, Thailand
PERSONAL ADDRESS	19/6 Worawichai Road, Muang, Nan 55000, Thailand
E-MAIL	warakornjindata@gmail.com

EDUCATIONS

2009-2013	B.Sc. (Physics), Kasetsart University
2013-2016	M.Sc. (Physics), Kasetsart University
2016-2021	Ph.D. candidate (Physics), Suranaree University of Technology

PUBLICATION:

Jindata, W., et al. (2021). Spectroscopic signature of negative electronic compressibility from the Ti core-level of titanium carbonitride MXene. **Applied Physics Reviews** 8: 021401. (Impact factor (2021) = 19.162)